HYBRID QUANTUM SYSTEMS WITH SOLID STATE SPINS IN DIAMOND

by

IGNAS LEKAVICIUS

A DISSERTATION

Presented to the Physics Department
and the Graduate School of the University of Oregon
in partial fulfillment of the requirements
for the degree of
Doctor of Philosophy

September 2020

DISSERTATION APPROVAL PAGE

Student: Ignas Lekavicius

Title: Hybrid Quantum Systems with Solid State Spins in Diamond

This dissertation has been accepted and approved in partial fulfillment of the requirements for the Doctor of Doctor of Philosophy degree in the Department of Physics by:

Benjamin Aleman	Chairperson
Hailin Wang	Advisor
Steven van Enk	Core Member
Cathy Wong	Institutional Representative

and

Kate Mondloch   Interim Vice Provost and Dean of the Graduate School

Original approval signatures are on file with the University of Oregon Graduate School.

Degree awarded September 2020

DISSERTATION ABSTRACT

Ignas Lekavicius

Doctor of Philosophy

Department of Physics

September 2020

Title: Hybrid Quantum Systems with Solid State Spins in Diamond

As work progresses towards a useful quantum computer using various physical implementations, it seems likely that no single physical system can fully realize all necessary requirements for a large scale, interfaced, stable quantum computer. Instead, it seems various systems are more predisposed for use as computational qubits while others to acting as "flying" qubits. The nitrogen vacancy center in diamond is a physical system of numerous applications, of which significant interest has been towards the NV's role in quantum computation. The center's impressive spin coherence as well as its coupling to magnetic fields, strain fields and nuclear spins suggests the role of the NV in hybrid quantum systems will be critical. In this dissertation, I will report on progress made towards the use of the NV in various hybrid quantum systems, including the coupling of the NV between optical, microwave and strain fields.

CURRICULUM VITAE

NAME OF AUTHOR: Ignas Lekavicius

GRADUATE AND UNDERGRADUATE SCHOOLS ATTENDED:

University of Oregon, Eugene
University of Nevada, Reno

DEGREES AWARDED:

Bachelor of Science in Physics and Mathematics, 2013, UNR

AREAS OF SPECIAL INTEREST:

Optics, Solid State Defects, Quantum Optics

PROFESSIONAL EXPERIENCE:

Research Assistant, Hailin Wang, Department of Physics, University of Oregon,
    2014-present.

Undergraduate Researcher, Andrew Geraci, University of Nevada, Reno, 2012

PUBLICATIONS:

[1]   I. Lekavicius, D. A. Golter, T. Oo, and H. Wang, "Transfer of Phase Information between Microwave and Optical Fields via an Electron Spin," *Phys. Rev. Lett.*, vol. 119, no. 6, p. 063601, Aug. 2017, doi: 10.1103/PhysRevLett.119.063601.

[2]   D. A. Golter, T. Oo, M. Amezcua, I. Lekavicius, K. A. Stewart, and H. Wang, "Coupling a Surface Acoustic Wave to an Electron Spin in Diamond via a Dark State," *Phys. Rev. X*, vol. 6, no. 4, p. 041060, Dec. 2016, doi: 10.1103/PhysRevX.6.041060.

[3]   I. Lekavicius, T. Oo, and H. Wang, "Diamond Lamb wave spin-mechanical resonators with optically coherent nitrogen vacancy centers," *Journal of Applied Physics*, vol. 126, no. 21, p. 214301, Dec. 2019, doi: 10.1063/1.5124307.

[4]   I. Lekavicius and H. Wang, "Optical coherence of implanted silicon vacancy centers in thin diamond membranes," *Opt. Express, OE*, vol. 27, no. 22, pp. 31299–31306, Oct. 2019, doi: 10.1364/OE.27.031299

ACKNOWLEDGMENTS

TABLE OF CONTENTS

LIST OF FIGURES

CHAPTER I

INTRODUCTION

With the emergence of quantum information science as a field of leading importance in contemporary physics, the search for the necessary components of a useful quantum computer has led to the investigation of numerous physical systems. One such system has been color centers in diamond which are optically active defects in a wide bandgap crystal. The most well known of these defects is the nitrogen vacancy center in diamond, which is formed of a substitutional nitrogen atom adjacent to a vacancy in the carbon lattice. The electronic and spin properties of these defects, along with their coupling to their environment allows for a wide array of applications ranging from magnetic field sensing, entangled photon generation and quantum spin memory. In this dissertation, I will discuss the importance of solid state spins in quantum computation, in particular their role in hybrid quantum systems which can couple quantum systems of disparate energies and control mechanisms.

1.1 Quantum Computation

A tremendous amount of attention and experimental effort has been drawn towards using the coherent quantum properties of physical systems towards improving computation schemes. Classical computers use physical switches to store and perform computations using binary information. These switches are themselves electronic circuits whose state is determined by the presence or lack of a voltage/current flow. Technological advancements since the 1970's have reduced the size and operating power of these chips of transistors, leading to modern transistor densities in excess of 10^7 transistors/mm^2. However, modern

computation may be saturating and reaching a limit for transistor density, breaking down Moore's Law[1]. Though the computational power achieved with these systems is massive there are certain classes of problems, of both practical and academic interest, which a classical computer cannot solve efficiently [2].

In contrast to a classical bit which can be in two given states (0 or 1, low or high, etc.), a quantum bit ("qubit") can be in a superposition of either state. As such, gate operations on qubits perform the operation on each element of the superposition state. Generally, the exact state of the quantum system is not something which can be fully measured in a single measurement operation. Instead, a projective measurement is made onto one of the basis states, with a probability given by the absolute value squared of the probability amplitude of the component of the superposition. Through the use of quantum algorithms, many of which involve interference measurements to extract additional information from the superpositions states, certain problems have been shown to have exponential decreases in the computation time needed to solve the problem as compared to their classical operation, one of the most well known of which being Shor's algorithm [3]. Though it is still an open question whether there are problems that can only be solved efficiently (i.e. in polynomial time) with quantum algorithms, it is a likely enough scenario that it has motivated huge effort towards the physical realization of a quantum computer.

The current physical systems leading in the number of qubits are linear trapped ion chains and superconducting qubits. Trapped ion chains have atomic transitions controlled by optical fields, which can then couple multiple ions in the chain together with a collective mechanical mode which excites multiple ions[4]. This excitation of the linear "string mode

coupling two ionic qubits can act as a two qubit gate. Trapped ion chains as high as 11 qubits have been realized [5] and have the advantage of being almost perfect qubits (Fig. 1a), basically immune to fabrication imperfection which plague systems larger than a few atoms. Two qubit gate operations on two separate ions in the chain usually involves optically exciting a common mechanical mode coupling the two ions, allowing for complete interconnectivity even between non-adjacent ions in the chain.

Superconducting circuit (SC) qubits are microwave frequency circuits which can use the state of various currents or charges to represent logical states. The presence of a Josephson junction introduces a nonlinearity into the otherwise evenly spaced energy levels of the SC qubit, allowing for the resonant control of two states. To reduce the loss effects of electrical resistance these systems generally operate at very cold temperatures to enable superconductivity of the material in the circuit (Fig. 1b). Due to the size and complexity of these systems, fabrication imperfections are a major issue in SC qubits. However, in contrast to linear trapped ion chains, SC qubits have a more obvious path forwards towards higher qubit devices. Superconducting circuits with up to 50 qubits have been realized [6]. Though there are a number of interesting applications of low qubit count quantum computers[7], the advertised supremacy of quantum computation over classical computers in certain problems will need many more logical qubits than is currently achieved by any system.

It is clear that systems so vastly different as trapped ions and SC qubits will have advantages and disadvantages compared with each other. For instance, trapped ions offer high coherence times ranging from milliseconds to seconds, as compared with SC qubits

which have coherence times on the order of 10-100μs[8]. This is due to trapped ion systems being naturally isolated from their environment, as the only sources of noise near them are adjacent ions and the currents in the fabricated chip underneath them. SC qubits on the other hand are strongly coupled to electric and magnetic noise due to the nature of their qubit states. Conversely, due to this strong coupling SC qubit gate operations are much quicker than trapped ion gate operations (~ns for SC vs. μs for trapped ions). Because of this, it has been suggested that future implementations of quantum computers will likely divide computational and storage operations into separate physical systems the same way that classical computers have.
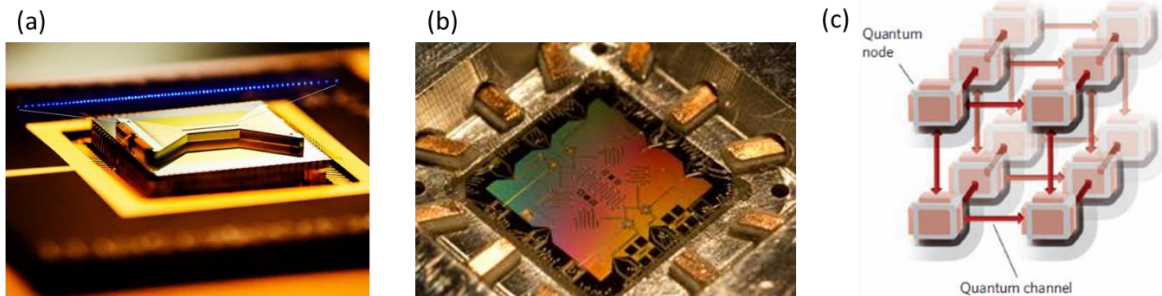
Figure 1: Implementations of multiple qubit quantum computer. (a) Image of a trapped ion chain over a fabricated magnetic trap. The individual ions are fluorescing and are thus visible to the naked eye. (b) Image for the chip and wiring of a superconducting circuit. (c) Schematic of quantum node/quantum channel implementation for resolving the scaling issue of numerous quantum computation schemes. (Images from[9], [10], [11] respectively)

1.2 Hybrid Quantum Systems

1.2.1 Introduction

A hybrid quantum system is a system combining disparate quantum systems such that the full system can utilize the advantages of each individual component. These systems

4

have been investigated with the motivation of improving the overall operations of a quantum computer and towards solving the scalability issues present in certain systems. Though tremendous progress has been made, it is possible that certain physical systems are already reaching the limit in the number of controllable qubits. For example, in the case of the linear trapped ion chain, adding more ions increases the density of the mechanical mode structure. At some point the mode structure will become so dense that it will become impossible to choose a single mode which couples two individual ions together and serves as the two qubit gate.

Though the problem of scalability for quantum computers might be solved purely with increasingly sophisticated engineering of current systems, there is an alternative. It has been suggested that building an array of small quantum "nodes" with a relatively small amount of qubits and then interfacing them coherently can alleviate this problem of scalability (Fig. 1c). In the case of trapped ions for example, a node might have 100 ions in a linear chain with a mechanical mode structure just barely resolved enough to allow for gate operations between every pair of qubits. This node would then be coupled to a number of different 100 ion nodes such that whatever quantum information needing to be preserved for parallel computation would be coherently exchanged between the nodes. In principle, the coherent channel or "bus" could be anything from optical photons, microwave photons or even phonons. A restriction on the quantum channel is that it must be able to carry "quantum information" (i.e. supports a superposition), though this is complicated by the fact that the fields used for the control of the qubits and operation of the gates may not be optimal for operation as "flying qubits" in the bus. Flying qubits would ideally be either optical or telecommunications wavelength photons propagating in optical fibers. As such

the qubit systems that do not operate with these fields may need a coherent conversion/transduction between computational qubits and flying qubits for the quantum node/channel system to operate.

Due to the wide range of fields that operate on qubits, a physical system which can interact with various fields is optimal for design as a quantum transducer. For this role, solid state defect spins, the nitrogen vacancy (NV) center in diamond in particular, are ideal. The NV center is a defect center in diamond with a long lived and coherent spin triplet ground state even at room temperature. Due to the long coherence time of the spin, the NV center has been a popular candidate for use as a storage qubit [12], [13]. The nuclear spin of the nitrogen in the NV center is additionally long lived and has drawn attention as a means for exceptionally long storage applications[14], [15]. In addition, the NV center has both orbital and spin transitions affected by optical fields, MW fields, magnetic fields and strain fields. This has led it to be used in numerous sensing applications ranging from magnetic fields sensing[16], [17], bolometry[18] and strain sensing[19]. Due to its remarkable coherence properties and coupling to a vast array of fields, the NV center in diamond is a promising physical system for the realization of a quantum transducer.

1.2.2 Coupling SC to Spins

A large amount of work has been done towards coupling SC qubits and superconducting resonators to various systems in the field of "hybrid quantum circuits." In particular, solid state spins systems such as the NV center in diamond have been used due to their long spin coherence times. An experiment by Zhu *et al.*[20] has coupled an ensemble of NV spins in diamond sample on top of a magnetic flux qubit SC sample (Fig.

2a). The energy of the flux qubit can be tuned into resonance to the ground state NV spin transitions, at which point vacuum Rabi oscillations of the flux qubit state can be observed (Fig 2b). Here, the flux qubit acts as a cavity coupling to the two level system of the NV ensemble analogous to an atom inside a resonant optical cavity. This experiment opens the possibility of storing information in a long lived spin system after whatever necessary gate operations have been performed on the computational qubit system. These types of couplings are not relegated to magnetic flux qubits either, as Kubo *et al.*[21] coupled an NV center ensemble in a diamond with a transmon qubit (Fig. 2c). The transmon qubit was interfaced with a superconducting circuit resonator which could be tuned to resonantly interact with the spin ensemble.
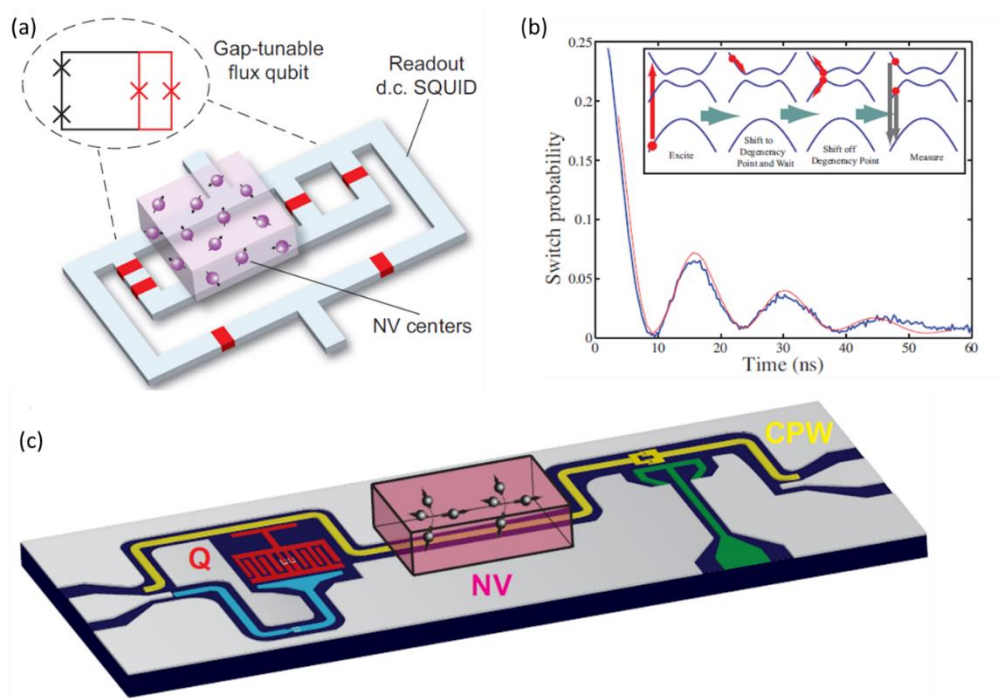
Figure 2: Two separate implementations of a hybrid SC system. (a) Schematic of diamond with NV ensemble placed at the point of highest magnetic fields of a flux qubit. (b) Vacuum rabi oscillations measuring the state population of the flux qubit. (c) Schematic of Transmon qubit coupled to a NV spin ensemble via a SC resonator. (Images a,b from [20], c from [21])

1.2.3 MW to Optical Transduction

A separate concern for the scalability of SC qubit systems is that the fields controlling the qubits (MW frequency photons) are not suitable for long range communications. Indeed, the most suitable long-ranged flying qubit candidates are optical or telecommunications frequency photons. This limitation of MW photons not only affects the implementation of a node based SC qubit quantum computer (Fig. 1c) but also the usefulness of SC qubit systems in the case of long range communications which transmit quantum information. It is because of this that coherent MW to optical state transfer/transduction is a topic of huge current interest. Numerous systems to accomplish this have been proposed ranging from mechanical resonators[22], collective spin ensembles of cold atoms [23] and electro-optic modulators [24]. Because of their similarity to spin carrying trapped atoms, NV centers offer a comparable way of performing the experiments suggested in [23] while using a physical system of significantly lower experimental complexity.

1.2.4 Mechanical Transduction

Though optical and telecommunications photons are the clear favorites for long range communications, there may be superior alternatives in the case of shorter scale interfaces. Mechanical modes/phonons are one such alternative which has a number of advantages over photonic modes. The speed of sound in most materials is nearly 5 orders of magnitude smaller than the speed of light, making on-chip timing requirements much less stringent. In addition, phonon modes cannot couple to vacuum, meaning that it is generally easier to create low loss mechanical systems as opposed to optical systems.

8

Various physical systems can either naturally couple to phonon modes, such as solid state defects in a crystal lattice [25], or can be designed to couple to mechanical oscillations, such as SC qubits[8]. In particular, flux qubits can easily be coupled to phonon modes if the displacement of the mechanical oscillator changes the flux area of the qubit[8]. The variety of quantum systems that can couple to phonon modes suggests that phonons are a promising and flexible platform for coherently interfacing systems of disparate energy or different physical control mechanisms.

1.3 Dissertation Overview

In this dissertation, I will report on the progress towards using solid state spins in diamond (i.e. the NV center and silicon vacancy center) to realize a quantum transducer for use in hybrid quantum systems. Chapter II gives a theoretical overview of the NV center including the ground state and excited state properties. In addition, it is discussed how the NV center ground state spin can be optically initialized and read out at room temperature. Chapter III gives an overview of the experimental techniques used towards imaging, initializing and controlling the NV center. Room temperature and cryogenic temperature quantum control experiments of the NV center are presented as preparation for Chapter IV.

Chapter IV reports on work done with a single NV center at cryogenic temperatures to coherently couple optical and microwave fields. The NV center is used as an intermediary to transfer the phase information stored in two MW fields which interact with the NV, after which two optical phase with some phase difference between them read out the state of the NV spin in such a way as to be dependent on the phase of the MW preparation fields. The reverse process is also accomplished, with optical preparation and

MW readout. This chapter gives a first step towards using the NV center to coherently convert electromagnetic fields of disparate energy levels.

Chapter V then changes the focus from electromagnetic fields to strain fields as a resource for achieving transduction. The coupling of the NV defect to single frequency phonons is discussed and the previous work in this field, which has focused on observing the effects due to strongly driven strain fields, is given a brief review. It will be shown that for useful transduction, the chosen two level system of the NV center must strongly interact at the level of single phonons and that high quality factor mechanical resonators are necessary to achieve this goal. At this point, a measurement scheme for detecting the interaction of the NV with phonons in a high quality factor resonator is discussed and simulated. Two varying types of "two level" systems in the NV are discussed, which impart differing requirements to the mechanical resonators to be used.

Chapter VI gives mechanical mode calculations for the chosen high frequency and high quality factor mode. Finite element analysis using COMSOL is used to give an estimate for the quality factors of the Lamb wave modes. Chapter VII describes the fabrication of mechanical resonators imbedded in phononic crystal shields, which should greatly reduce mechanical dissipation and lead to a high quality factor mechanical mode. In addition to the design and fabrication of the resonator, detail is given on how to maintain reasonable optical coherence properties of the NV center excited state in sub-micron thick diamond membranes, which up to this point has presented a major obstacle. The Appendix gives work done in parallel with silicon vacancy centers in diamond. Thin diamond

membranes with implanted silicon vacancy centers are shown to maintain their optical coherence even in <100nm thick diamond.

The contents of Chapter IV includes materials from [26] which were coauthored by Hailin Wang, Thein Oo and Andrew Golter. Content from Chapter VII comes from [27] which was coauthored by Hailin Wang. Content in the Appendix comes from [28] which was also coauthored by Hailin Wang.

CHAPTER II

THE NITROGEN VACANCY CENTER IN DIAMOND

2.1 Overview

Diamond is a material with remarkable chemically inertness, a high Debye temperature (2250K) and the highest known speed of sound (12,000 m/s) of any material. In addition, it has a very large band gap of 5.5 eV. Because of this, defect centers with optical transitions in the visible regime can be optically addressed in the otherwise transparent material. One such defect center is the negatively charged nitrogen vacancy (NV) center. The NV center is formed with a vacancy in the carbon lattice adjacent to a substitutional nitrogen atom (Fig. 3a). The unpaired electrons from the adjacent carbon atoms and nitrogen form the energy levels of the NV center, which is often called "nature's trapped atom." The states of the NV center can be represented in the basis of the hybridized sp^3 orbitals (Fig. 3b) [29]. There are two known charge states of the NV center, the neutrally charged NV^0 [30] and the negatively charged NV^-, of which only the NV^- has a spin carrying ground state. As such, for the remainder of this dissertation, the NV^- will be referred to as simply the NV.

The NV center can be optically addressed since the energy of its excited state transitions is less than the electronic bandgap of the diamond lattice. Off-resonant excitation of a single NV center with a 532nm laser excites the electron population, whose emission spectrum is shown in Figure 3c. There is a primary zero-phonon line (ZPL) occurring at 637nm with a large phonon-sideband (PSB) extending out to 800nm. The Debye-Waller factor of the NV center is relatively low (~.03), resulting in only 3% of the

fluorescence emitting at the ZPL. This factor complicates NV related quantum entanglement experiments, where indistinguishable photons are necessary, though the emission into the ZPL can be enhanced via optical cavities resonant at the NV ZPL[31]. Though the large PSB of the NV is a detriment in entanglement experiments, it is a useful property when performing resonant optical excitations which require the filtering out of an excitation laser on resonance to the NV center transitions (i.e. laser at the ZPL frequency). A feature of note in the spectrum of the NV center is the ZPL of the neutral NV^0 center at 568nm. The charge stability of the NV$^-$ center is a function of the electronic environment surrounding it and is of critical importance, as NV$^-$ charging to NV^0 is an important loss mechanism to be aware of while performing quantum control experiments on the NV.
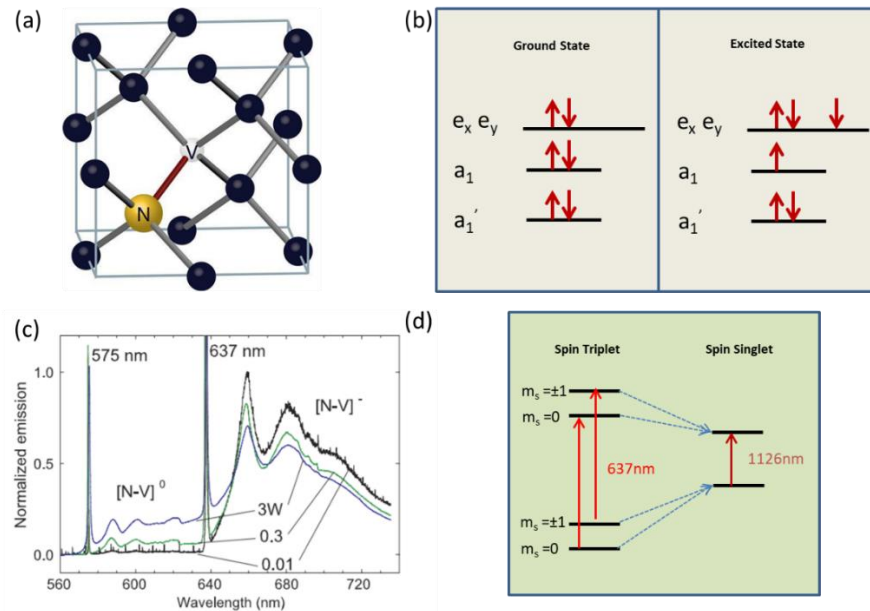
Figure 3:Overview of the NV center in diamond. (a) Diagram of the NV in a diamond lattice (Picture from https://www.chemistryworld.com/news/putting-a-new-spin-on-things/3007939.article). (b) Energy level scheme of the NV center in the basis of sp^3 hybridized orbitals. (c) Photoluminescence spectrum of the NV$^-$ and NV^0 center[32]. (d) Excited state structure of the NV center with the spin triplet and spin singlet configurations. The intersystem crossing transitions are represented by the dashed arrows while the dipole allowed transitions are represented by solid arrows.

13

2.2 The NV Ground State

With the states of the 5 electrons from the lattice and 1 additional electron each approximated in the sp^3 hybridized basis, the state of the NV center can then be treated as the state of two sp^3 electron holes, as 8 electrons would lead to a completely filled orbital (Fig. 3b). It is then clear that a two-hole system possesses a spin S=1 ground state. The $m_s=\pm1$ states in the ground state are split from the $m_s=0$ state by due to spin-spin interactions by ~2.87GHz at room temperature. These spin states can then be further split and isolated by an external magnetic field applied on the axis of the vacancy defect. In addition to any external magnetic fields, the electron spins also interact with the nuclear spin of the adjacent nitrogen atom. Depending on the isotope of the nitrogen, each of the $m_s=\pm1$ are split into triplets detuned by 2.2MHz for ^{14}N or a doublet detuned by 3MHz for ^{15}N. The full ground state Hamiltonian with the nuclear spin interactions is given as:

$$H_{gs} = D_{gs}\left[S_z^2 - \frac{S(S+1)}{3}\right] + A_{gs}^{\perp}S_zI_z + A_{gs}^{||}\left[S_xI_x + S_yI_y\right]$$
$$+ P_{gs}[I_z^2 - \frac{I(I+1)}{3}]$$

(1)

Here, $S_{x/y/z}$ are the respective Pauli matrices in three dimensions, D_{gs} is the ground state spin-spin splitting roughly equal to 2.87GHz, $A_{gs}^{\perp/||}$ are the non-axial/axial nuclear magnetic hyperfine parameters (dependent on the nitrogen isotope) and P_{gs} is the nuclear electric quadropole parameter [12]. The effects of magnetic, electric and strain fields on the NV can be described by the addition of the following interaction Hamiltonian:

14

$$V_{gs} = \mu_B g_{gs}^{||} S_z B_z + \mu_B g_{gs}^{\perp}(S_x B_x + S_Y B_y) + \mu_N g_N \vec{I} \cdot \vec{B}$$

$$+ d_{gs}^{||}(E_z + \delta_z)\left[S_z^2 - \frac{S(S+1)}{3}\right] \tag{2}$$

$$+ d_{gs}^{||}(E_x + \delta_x)(S_y^2 - S_x^2) + d_{gs}^{\perp}(E_y + \delta_y)(S_x S_y$$

$$+ S_y S_x)$$

Here μ_B is the Bohr magneton, μ_N is the nuclear magneton, g_{gs}^{α} are the relevant components of the electron g-factor, g_N is the nitrogen nuclear g-factor and d_{gs}^{α} are the components of the ground state electronic dipole moment. From this interaction Hamiltonian, we can see that the static magnetic fields aligned off axis to the NV mix the spin character of the ground state. In addition, static strain and electric fields have the equivalent effects to each other on the energy level structure.

The NV center is optically addressable with off resonant laser light. Though off-resonant, this excitation is still somewhat spin dependent, meaning that the populations in the three different initial states end up in different excited state. While in the excited state, the population can decay back radiatively to the triplet ground state or non-radiatively into the spin singlet state (Fig. 3d). The transition from the triplet to singlet spin configuration is called the intersystem crossing (ISC) and is highly spin selective. Because of this, population in the $m_s=\pm1$ excited states preferentially transitions to the singlet configurations after a few optical cycles, while population in the $m_s=0$ ground and excited states is allowed to complete many more optical cycles in the triplet configuration. In

addition, the decay out of the singlet into the ground state triplet can populate any of the spin ground states. This leads to two critical properties of the NV center which allow for room temperature quantum control experiments. Firstly, off-resonantly pumping the NV will eventually lead to a high fidelity initialization [12] into the m_s=0 state. Secondly, the spin selectivity of the ISC leads to high fluorescence intensity if the NV begins in the m_s=0 state and relatively low intensity for the m_s=±1 states. These two features allow for off resonant, room temperature spin initialization and state readout of the NV center.

2.3 The NV Excited State

The excited state structure is an orbital doublet and spin triplet, leading to 6 total excited states. These states are labelled by their group theoretic symmetries; $E_{1/2}$, $E_{x/y}$ and $A_{1/2}$ (Fig. 4a). At room temperature phonon interactions broaden all 6 transitions into a single ZPL located at 637nm in the spectrum. When cooled to below 10K, the phonon interactions are frozen out and the linewidths of all excited state transitions become resolvable[33]. Dipole allowed optical transitions must conserve orbital angular momentum and can be determined by group theory[34]. Transitions to $|E_{x,y}\rangle$ from $|m_s=0\rangle$ take place with linearly polarized light and transitions from $|m_s=\pm1\rangle$ to $|A_{1,2}\rangle$ and $|E_{1,2}\rangle$ occur with circularly polarized light. The highly polarized emission into these states has been used as a source for entangled photons in loophole free Bell inequality violations[35]. The zero field effective Hamiltonian for the excited state is given by the following:

16

$$H_{es} = D_{es}^\perp \left(S_z^2 - \frac{S(S+1)}{3} \right) - \lambda_{es}^\parallel \sigma_y \otimes S_z$$

$$+ D_{es}^\perp \left[\sigma_z \otimes (S_y^2 - S_x^2) - \sigma_x \otimes (S_y S_x + S_x S_y) \right]$$

$$+ \lambda_{es} \left[\sigma_z \otimes (S_x S_z + S_z S_x) - \sigma_x \otimes (S_y S_z + S_z S_y) \right]$$

$$(3)$$

As before, S_α's are the S=1 spin operators while the σ's are the two dimensional Pauli matrices in the basis of the two orbital configurations $\{E_x, E_y\}$. The field interaction Hamiltonian of the excited state with static magnetic, electric and strain fields is given as:

$$V_{es} = \mu_B (l_{es}^\parallel \sigma_y + g_{es}^\parallel S_z) B_z + \mu_B g_{es}^\perp (S_x B_x + S_Y B_y) + d_{gs}^\parallel (E_z + \delta_z)$$

$$+ d_{es}^\perp (E_x + \delta_x) \sigma_z - d_{es}^\perp (E_y + \delta_y) \sigma_x \qquad (4)$$

Here, $l_{es}^\parallel$ is the magnetic moment of the orbital excited state and $d_{es}^\parallel$ and $d_{es}^\perp$ are the components of the orbital dipole moment. Like the ground state Hamiltonian, both strain and electric fields affect the energy structure equivalently, splitting and mixing the orbital configurations depending on if the strain/electric field is on-axis to the NV or off-axis. The splitting component will be especially crucial in the coming work, since a time varying strain field will modulate the energy levels and create sidebands detuned by the frequency of the strain modulation.
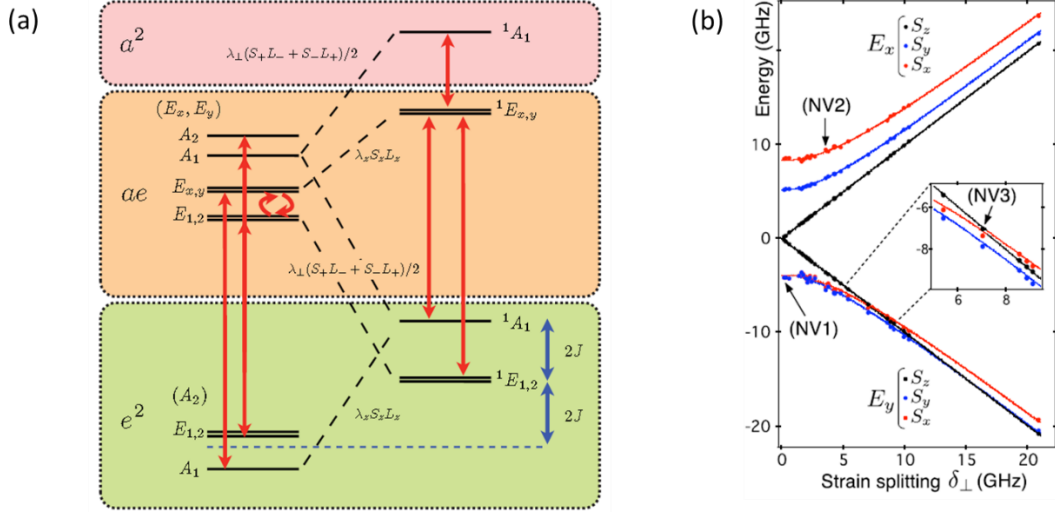
Figure 4: Excited state of the NV. (a) Full energy level diagram of the NV center [34]. (b) Energy splitting of the excited state as a function of off-axis static strain [33].

For completeness, the effects of lateral (i.e. off-axis) strain are shown in Fig. 4b. As no real sample is truly strain free, the actual energy spectrum of an NV is typically in the 1-5GHz strain region for most bulk diamond samples. Diamond sample with especially high amounts of fabrication performed on them (such as those with solid immersion lenses[36]) can have higher strains in the 10s of GHz. This can be a detriment if you need high polarization fidelity (such as in entangled state preparation) or strong selection rules. However, this induced mixing may also be a resource when an optical lambda system is required without the use of microwaves to induce transitions in the ground state due to the existence of anticrossing sites that mix the spin character of two excited states[37].

In summation, the NV center is a defect center with useful properties at both room temperature and cryogenic temperatures. It is a center whose energy levels and eigenstates are affected by external magnetic, electric and strain fields. This has led it to be explored

as a useful quantum sensor at room temperature for magnetic and strain fields as well as

temperature fluctuations.

CHAPTER III

CHARACTERIZATION AND CONTROL OF NV CENTERS

3.1 Confocal Microscopy

The workhorse of NV experiments is the confocal microscope. Though the control mechanisms applied to the defect center differ, nearly all signals detected are optical intensity measurements made from the fluorescent light of the NV center(s). In general, a confocal microscope consists of an excitation optical path which reflects off a beamsplitter and is focused onto the sample through an objective lens. The sample then emits light omni-directionally and the objective lens collects the light in a cone with a solid angle determined by its numerical aperture (NA). The fluorescent light follows the reversed path and splits at the beamsplitter into the collection path, which usually consists of another objective lens focusing the beam onto a pinhole. The pinhole acts as a spatial filter, removing noise from the collection path and filtering out everything except that which was initially in focus at the sample objective.

The confocal setup used for the experiments in this chapter is shown in Figure 5. Off resonant excitation at 532nm is provided via a diode laser (LaserGlow LRS-0532). The laser is passed through a band pass filter centered at 540nm to remove excess power away from the central frequency and then through an acousto-optic modulator (AOM) (Gooch & Housego R23080). An AOM is a crystal attached to a piezoelectric that will cause it to vibrate at some external RF frequency. The Brillouin scattering caused by the vibration will cause the laser light passing through it to scatter into separate sidebands, where the laser frequency is then detuned by some multiple of the piezo driving frequency. The

primary use of the AOMs will be to shutter the lasers with a fast, programmable signal pulse, as all but one of the spatial laser sidebands is blocked out. The main computer control of the pulse sequences is done through a SpinCore Pulseblaster. This outputs up to 8 TTL pulses controlled by the computer with a frequency of 400MHz (corresponding to a time resolution of 2.5ns). The TTL pulse from the SpinCore and an RF generator combine in a frequency mixer (Minicircuits ZAD-1+) which is used as a switch to modulate the signal going to the AOM. The green laser path goes to a 602nm longpass (LP) dichroic beamsplitter upon which it reflects from another 650nm LP dichroic and into the galvomirror assembly and the objective lens (Nikon L Plan 100X/0.85NA). The purpose of the galvomirrors is to steer the excitation beam across the aperture of the objective lens which in turn results in a spatial rastering of the focused beam across the sample. The emitted fluorescence at the sample then follows the reverse optical path up to the 650nm LP dichroic, upon which light above 650nm (i.e. the phonon sideband) transmits through towards additional green and red filters and then to an objective lens focused into a multimode fiber with a core diameter of 30μm terminating at the avalanche photodiode (APD). The red laser paths follow similar paths of being focused into AOMs which gates them. They are then coupled into a polarization preserving single mode fiber to clean up the spatial mode and then emitted to free space. A half-wave (λ/2) plate is used to control the linear polarization of the red lasers, after which they are combined with the green path on the 602nm LP beamsplitter. An example photoluminescence fluorescence (PL) scan performed on a diamond sample with a SIL fabricated on it is shown in Figure 6.
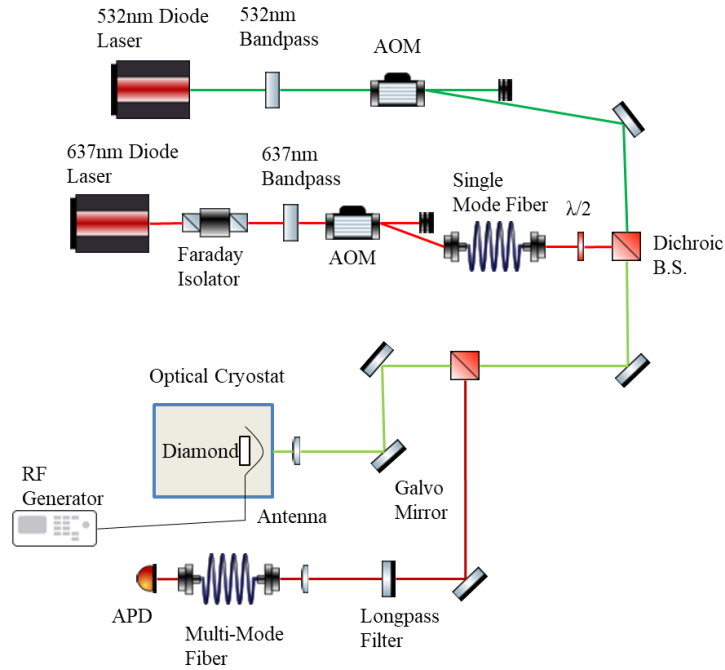
Figure 5: Confocal setup for imaging diamond samples in an optical cryostat (ComponentLibrary by Alexander Franzen is licensed under a Creative Commons Attribution-NonCommercial 3.0 Unported License) .
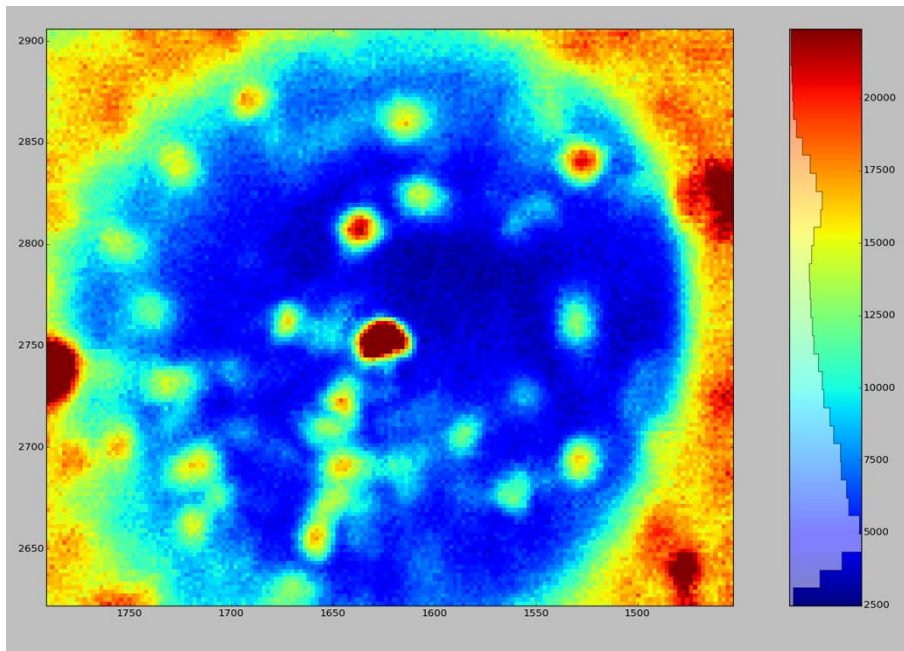
Figure 6: Example PL scan of diamond sample with fabricated SIL structure. Areas with high fluorescence counts suggest the presence of a single NV center, whose dimensions on the scan are determined by the spot size of the laser focus (after the 100X objective) which in this case is ~1μm.

3.2 Ground State Quantum Control

Microwave (MW) frequency fields of frequency~2.8GHz can be used to induce spin transitions within the triplet ground state. A continuously exciting MW field, scanned in frequency while a focused 532nm laser excites and collects fluorescence from a single NV shows the zero field splitting of the triplet ground state at 2.8GHz (Fig. 7a). As mentioned before, the majority of state population of the NV center after a few milliseconds of green excitation is in the m_s=0 spin state. The spin dependence of the ISC results in the m_s=0 state fluorescing more strongly than the m_s=±1 states which cycle out and non-radiatively decay through the spin-singlet branch of transitions. Therefore higher m_s=±1 population results in a decrease in counts, meaning a resonant MW field results in a fluorescence dip. A magnetic field, aligned on the NV symmetry axis, results in a Zeeman splitting of 2×2.8MHz/Gauss between the m_s=-1 and m_s=+1 transitions. This is referred to as optically detected magnetic resonance (ODMR). Upon spectrally isolating the individual transitions, coherent, quantum control of each may be performed using the MW fields. Rabi oscillations are shown in Figure 7b, where the MW pulse time is varied. The oscillations shown correspond to a cycling of state population between the m_s=0 and m_s=-1 spin ground states, while the decay of the oscillation contrast is caused by dephasing of the spin state superposition. The period of the Rabi oscillation informs what the actual magnetic field strength is projected onto the NV dipole transition and allows us to perform a π-pulse to completely invert the state of the NV from m_s=0 to either m_s=±1 state. As such, we can obtain maximum signal for the ODMR dip at various MW power levels (Fig. 7c). Reducing the MW Rabi frequency below the NV hyperfine splitting of 2.2MHz (in the case

of ^{14}N) is necessary to narrow the transitions and resolve the three hyperfine ODMR dips resulting from the nuclear spin coupling of the NV center (Fig. 7d).

To characterize the spin coherence time of the NV environment, a Ramsey pulse sequence can be used. The state of the NV is put into an equal superposition of the two states using a $\pi/2$ pulse and allowed to evolve for a variable time t before a second $\pi/2$ pulse projects the state for a spin measurement. A representative Ramsey pulse graph is shown in Figure 8a, where the 2.2 MHz signal is due to only one of the three hyperfine transitions being on resonance with the MW field while the other two are 2.2 MHz detuned. This fact can be confirmed by detuning the MW field from the central peak onto one of the side hyperfine dips, resulting in a fluorescence signal with two frequency components. Figure 8b shows such a case, where the MW frequency is detuned 2.2MHz away from the central dip and a sum of two frequency signals is fit onto the data. The decay of the Ramsey oscillation is caused by the decoherence mechanisms present within the system, which is primarily due to ^{13}C nuclear spins present near the NV site which. While precessing, the ^{13}C spins induce a time varying magnetic field that alters the energy difference between the $m_s=0$ state and $m_s=\pm1$ states. A decay time of ~3µs is shown in the Ramsey fringe figure, which is representative of most NVs found in this diamond sample. It should be noted that spin coherence as high as 1.3ms have been observed in diamond isotopically purified of ^{13}C[38].
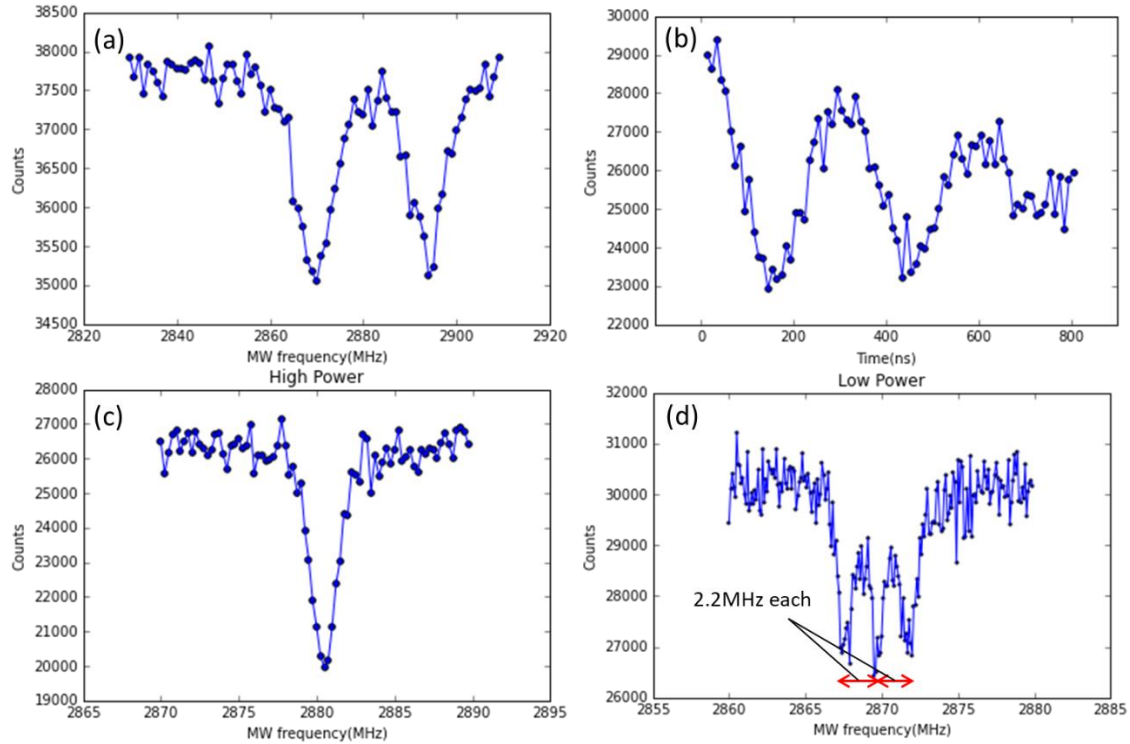
Figure 7: Control of the NV ground state. (a) CW ODMR with an external magnetic field. (b) MW Rabi oscillations between the $m_s=0$ and $m_s=-1$ states. (c) Deeper ODMR dip due to the use of a π-pulse. (d) Low MW power ODMR. The MW Rabi frequency is low enough to resolve the three nuclear hyperfine transitions.
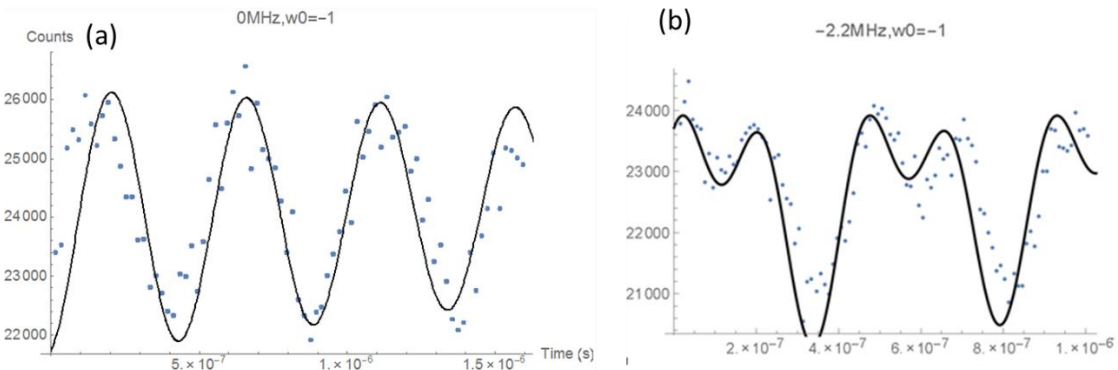
Figure 8: Ramsey fringes with various detunings. (a) MW driven Ramsey fringes. The MW is resonant to the central hyperfine transitions, resulting in a beating frequency of 2.2MHz due the two other off-resonant transitions. (b) Case of the MW field resonant to one of the side hyperfine transitions shown in Figure 7d. The fitting function is the sum of two sine waves of each with the frequency of the MW detuning from the non resonant transitions (i.e. 2.2MHz and 4.4MHz)

25

3.3 Excited State Quantum Control

With quantum control established over the ground state at room temperature, our attention turns to optical control of the excited state. Resonant optical transitions necessitate the cooling of the diamond lattice to below 20 Kelvin to freeze out phonon induced broadening of the excited state transitions[39]. The NV excited state is an orbital doublet spin triplet, resulting in six total states. The presence of thermal phonons at room temperature broadens and mixes these transitions such that they appear as a single, broad ZPL in the spectrum. Though this adds experimental overhead, control of the excited state at cryogenic temperatures allows for high fidelity (>95%) state preparation, entangled photon generation[35] and all optical control of the spin states[40].

A representative photoluminescent excitation (PLE) pulse sequence in shown in Figure 9a. The green laser pulse is still required to initialize the charge state of the NV center into NV$^-$ and to prepare the state in m_s=0. A resonant laser pulse at 637nm is then scanned in frequency while the photon counts at the APD are detected. This method necessitates the use of a LP filter at 650nm to filter out the laser light and, by extension, the ZPL of the NV center. The NV's low Debye-Waller factor leads to a relatively low amount of the NV fluorescence appearing in the ZPL and, as such, the reduction in counts due to the use of a LP filter to filter out the resonant laser light is minimal. Laser frequencies which are resonant to one of transitions result in an increase in counts (Fig. 9b). The emission lifetime of the NV excited state is ~13ns, leading to a 17MHz lifetime limited full width at half max (FWHM). However, due to power broadening and spectral diffusion in the sample, the measured linewidth is usually larger than that. Due to the fact that the pulse

sequence for the linewidth measurement is repeated many times for a given point in the frequency scan, the electronic environment around the NV center is slightly different each time due to the high amount of green power used to initialize the center. This change in the electronic environment shifts the energy levels of the orbital transition slightly, due to the permanent dipole moment present in the NV center. This will become a major issue that will need to be addressed in Chapter VII.
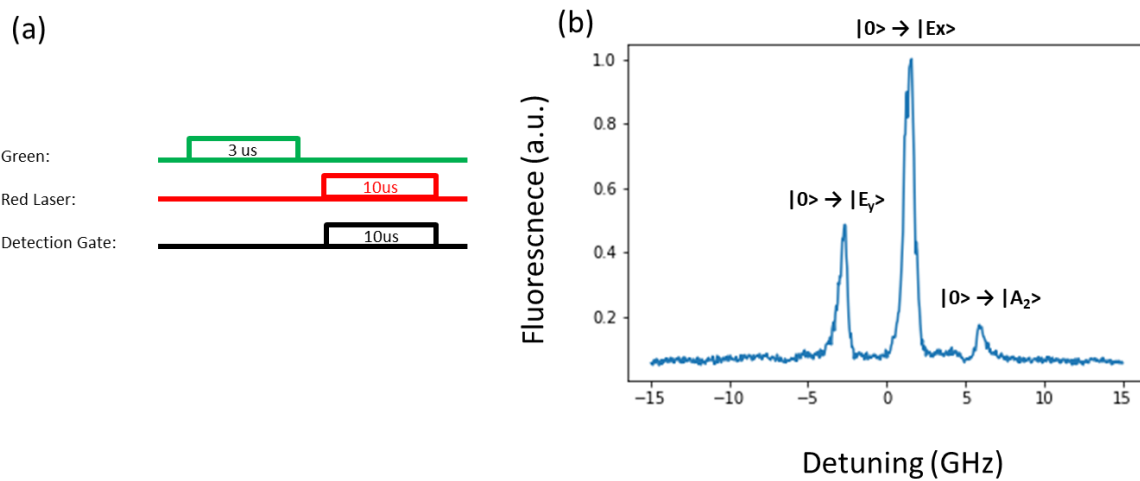
Figure 9: Excited state control of the NV. (a) Pulse sequence for PLE. (b) Typical PLE scan of single NV at 10K. The inherent strain in the diamond lattice both splits the energy levels of the two $m_s=0$ excited states and mixes the selection rules of the other transitions, allowing for the excited state A_2 to be seen.

As shown in the interaction Hamiltonian of the NV excited state, strain can affect the spin selection rules of the NV transitions. The states E_x and E_y have spin component $m_s=0$ and are thus visible in Figure 9b since the state of the NV is initialized into $m_s=0$. However, the state A_2 has spin components $m_s=\pm1$ and should not be visible with this initialized population. The cause of this is that since every real diamond lattice has some amount of inherent strain, the spin selection rules of state A_2 mix with one of the $m_s=0$

excited states and allow for its excitation from the $m_s=0$ ground state. In addition, the inherent strain also splits the energies of E_x and E_y. This is an important feature to note since this causes transitions which could normally cycle for a long time to optically pump into a different spin ground state than their initial one. This is the reasoning for the 10μs collection time in the pulse sequence shown in Figure 9a, even though the other limiting factor for how long the transition can cycle, the NV charge state lifetime is normally much longer than that.

CHAPTER IV

TRANSFER OF PHASE INFORMATION BETWEEN DISPARATE FIELDS

This chapter contains material co-authored with Andrew Golter, Thein Oo and Hailin Wang[26]. The experiment described here was performed by the author.

4.1 Introduction

As shown in Chapter III, the energy level structure of the NV center allows the coupling of both microwave and optical fields, though experimental studies have thus far focused on either coherent microwave or optical interactions. Previous sections have discussed the manipulation of the ground state with MW fields or single transition driving of an excited state, while other work has performed optically driven Raman transitions between the spin states [41], [42]. The robust spin coherence of the NV ground state enables dark-state based optical processes such as coherent population trapping (CPT) [43] and stimulated Raman adiabatic passage[40]. Electron spin ensembles in diamond as well as rare-earth-ion doped crystals have been coupled to a superconducting resonator or qubit via microwave transitions[44], [45]. This unique combination of optical and microwave properties suggests that electron spin coherence in diamond can provide an excellent experimental platform to mediate coherent coupling and to develop an interface between optical and microwave fields.

In this chapter, we demonstrate that a single NV center in diamond can enable the coherent coupling and transfer of phase information between microwave and optical fields.

We map the relative phase of two microwave fields to a superposition spin state in a NV center and then read out the phase with two optical fields. A closely-related process is used for the transfer of phase information from optical to microwave fields. We show that a special superposition spin state, the so-called dark-state, which is decoupled from either optical or microwave fields, plays a central role in the coherent microwave-optical coupling. Theoretically, similar coherent coupling in a NV ensemble can enable the full quantum-state transfer between microwave and optical fields. In addition, our studies also reveal the important effect of optical pumping on the preparation and readout of superposition spin states. The optical pumping hinders optical readout of the superposition states but facilitates optical preparation of the dark state as well as the mapping of optical phase information to the dark state.

4.2 Theory

The scheme for coherent coupling between optical and microwave fields is based on a coherent superposition of the $m_s = \pm 1$ ground spin states in a NV center. As illustrated in Fig. 10, this superposition can couple to a pair of microwave fields via the transitions to the $m_s = 0$ ground spin state and to a pair of optical fields via the electric dipole transitions to an excited state, such as the A_2 state. To demonstrate that this energy level structure can enable the interfacing between optical and microwave fields, we first map or encode the relative phase of the two microwave fields into the relative phase, θ, of a superposition spin state,

$$|\psi> = e^{i\theta}|C_+||+1> +|C_-||-1>$$ (5)

where $C_{\pm}$ are the complex probability amplitudes for states $|\pm1>$ (see Fig. 10a). This relative phase is then read out by the two optical fields (see Fig. 10b). Similarly, encoding the relative optical phase into the superposition spin state and then retrieving the phase information with a pair of microwave fields can transfer phase information from optical to microwave fields.

4.2.1 Ground State Spin Preparation

The mapping of the phase of microwave fields to an electron spin takes place via the V-type three-level system which couples to two resonant microwave fields shown in Fig. 10. The interaction Hamiltonian in the rotating frame is given by:

$$H_{\text{int}} = \frac{\hbar}{2} \begin{pmatrix} 0 & |\Omega_1|e^{i\omega_1 t - i\phi_1} & |\Omega_2|e^{i\omega_2 t - i\phi_2} \\ |\Omega_1|e^{-i\omega_1 t + i\phi_1} & 2v_+ & 0 \\ |\Omega_2|e^{-i\omega_2 t + i\phi_2} & 0 & 2v_- \end{pmatrix}$$

$$,\qquad (6)$$

where $\omega_{1,2}$, $\varphi_{1,2}$ and $\Omega_{1,2}$ are the frequency, phase, and Rabi frequency for the respective microwave fields and $v_{+,-}$ are the transition frequency for the respective microwave transitions. The wave function of the V-system is written in the form,

$$|\psi(t)\rangle = C_0|0\rangle + C_+ e^{-iv_+ t}|+1\rangle + C_- e^{-iv_- t}|-1\rangle. \qquad (7)$$

For the microwave state preparation, two resonant microwave fields create a coherent superposition of states $|+1>$ and $|-1>$ by first exciting half the population from $|0>$ to $|+1>$ using a $\pi/2$ pulse and then exciting the rest from $|0>$ to $|-1>$ using a π pulse. For the first

excitation, $\Omega_2=0$. Therefore, only the evolution of the probability amplitudes C_0 and C_+ is relevant. The corresponding equation of motion assuming $\omega_1 = v_+$ is given by,

$$\begin{pmatrix} \dot{C}_0 \\ \dot{C}_+ \end{pmatrix} = \frac{1}{2} \begin{pmatrix} 0 & -i|\Omega_1|e^{-i\phi_1} \\ -i|\Omega_1|e^{i\phi_1} & 0 \end{pmatrix} \begin{pmatrix} C_0 \\ C_+ \end{pmatrix} \tag{8}$$

Solving Eq. 8 with the initial conditions $C_0(t=0)=1$ and $C_+(t=0)=0$, the state after the $\pi/2$ pulse is given as,

$$C_0 = \frac{1}{\sqrt{2}} \ and \ C_+ = -ie^{-i\phi_1}/\sqrt{2} \tag{9}$$

For the second excitation, the corresponding equation of motion is given by:

$$\begin{pmatrix} \dot{C}_0 \\ \dot{C}_- \end{pmatrix} = \frac{1}{2} \begin{pmatrix} 0 & -i|\Omega_2|e^{-i\phi_2} \\ -i|\Omega_2|e^{i\phi_2} & 0 \end{pmatrix} \begin{pmatrix} C_0 \\ C_- \end{pmatrix} \tag{10}$$

Solving equation 10, the state after the π pulse,

$$|\psi\rangle = \frac{-ie^{i\phi_1-i\omega_a T}}{\sqrt{2}} \left(|+1\rangle + e^{i(\phi_2-\phi_1)+i(\omega_a-\omega_b)T} |-1\rangle \right) \tag{11}$$

where T is the duration of the $\pi/2$ pulse and $\omega_{a,b}$ are the respective detunings of the MW transitions. Note that no decay processes are included in the above calculations. As shown in Eq. 11, the coherent interactions between the microwave fields and the V-system effectively map the relative phase of the microwave fields to the coherent superposition of the electron spin states.

32

4.2.2 Optical Bright and Dark States

In a three level lambda system coupled to two resonant fields, the Hamiltonian after taking the rotating wave approximation in the field interaction representation is given as:

$$\hbar \begin{pmatrix} 0 & \Omega_a/2 & \Omega_b/2 \\ \Omega_a/2 & 0 & 0 \\ \Omega_b/2 & 0 & 0 \end{pmatrix} \tag{12}$$

Note that the Rabi frequencies are complex. The eigenstates of this Hamiltonian are:

$$|d\rangle = \frac{1}{\sqrt{\Omega_a{}^2 + \Omega_b{}^2}} \left(\Omega_b |a\rangle - \Omega_a |b\rangle \right)$$

$$|l\rangle = \frac{1}{\sqrt{\Omega_a{}^2 + \Omega_b{}^2}} \left(\Omega_a |a\rangle + \Omega_b |b\rangle - \sqrt{(\Omega_a{}^2 + \Omega_b{}^2)} |c\rangle \right)$$

$$|u\rangle = \frac{1}{\sqrt{\Omega_a{}^2 + \Omega_b{}^2}} \left(\Omega_a |a\rangle + \Omega_b |b\rangle + \sqrt{(\Omega_a{}^2 + \Omega_b{}^2)} |c\rangle \right) \tag{13}$$

The state |d>, which is called the dark state, has an eigenvalue of zero and is decoupled from the excited state |c>. The states |u> and |l> have populations in |c> which in the case of our experiments will be the state A_2. The initial state before the microwave fields are turned on can be expressed as some superposition of the three states |d>, |l> and |u>. The amplitudes of the |l> and |u> components will quickly decay due to spontaneous emission from A_2, which has a lifetime ~12 ns, while |d> is decoupled from excitations to |A2>. Once steady state is reached, all population in the system will be trapped in |d>. The phase dependence of the superposition |d> becomes clear if we express it as:

$$|d\rangle = \frac{1}{\sqrt{\Omega_a^2 + \Omega_b^2}} e^{i\phi_b} \left(|\Omega_b\||a\rangle - e^{i(\phi_a - \phi_b)} |\Omega_a\||b\rangle \right)$$

(14)

The overall phase factor does not matter in our experiments and the phase difference between the two optical fields determines the phase of the superposition of the two lower states.
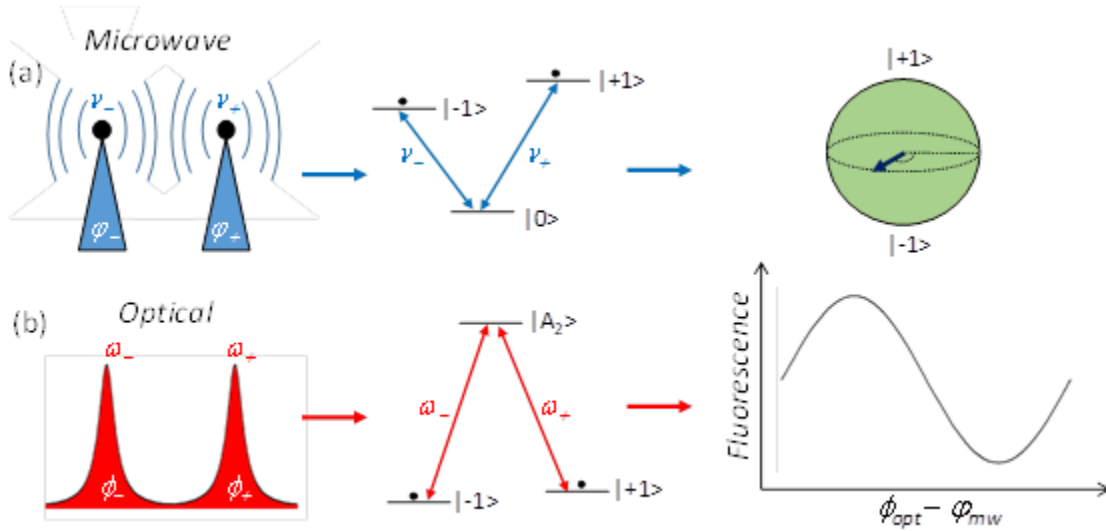
Figure 10: Scheme for phase transfer with a NV. (a) Two microwave fields, with relative phase φ_{MW}, couple resonantly to the $m_s = \pm 1$ transitions and generate a coherent superposition of those states, effectively mapping MW phase to the spin superposition. (b) Two optical fields, with relative phase φ_{OPT} couple resonantly to the A_2 transition. The fluorescence from the A_2 state features sinusoidal oscillations as a function of $\varphi_{OPT} - \varphi_{MW}$, effectively reading out the relative microwave phase and transferring the phase information from the microwave to the optical fields.

4.3 Experimental Methods

An electronic grade single-crystal diamond is used in our experiment. The sample is cooled to 10 K in a closed-cycle optical cryostat. Fluorescence from a native NV center about 5 µm below the surface is collected with a confocal microscopy setup (Fig. 11).

34

Time-resolved fluorescence is performed with an avalanche photodiode hooked up to a field programmable gate array (FPGA) with a time resolution of 2.8 ns. Unless otherwise specified, the Rabi frequency of the microwave fields used is 0.91 MHz, which is small compared with the NV hyperfine splitting (2.2 MHz) such that a microwave field can couple resonantly to only one set of hyperfine states. The corresponding durations for $\pi/2$ and π pulse are 225 ns and 550 ns, respectively. The optical Rabi frequency used is 27 MHz, determined from power broadening of the dipole optical transition. A small wire over the diamond sample is connected to two phase-locked signal generators which create the microwave fields necessary for transitions in the ground state of the NV center. The RF signal generators maintain a fixed phase relationship with the double-pass AOM which generates the two optical fields that drive the transitions between the ground state and excited state A_2. The phase of the double-pass AOM driver determines the phase difference between the 0th and 1st order beams, and the driving frequency determines the frequency splitting. To be on Raman resonance with the A_2 transitions, the optical fields need to be detuned by the Zeeman splitting of the $m_s=+1$ and $m_s=-1$ ground states. The splitting between the ground states is generated by a permanent magnet placed outside the cryostat and is roughly 212MHz. There is a $\lambda/4$ plate placed on the optical path of the 0th order beam that effectively shifts its polarization by 90°. A second $\lambda/4$ plate placed before the objective shift the polarizations of the two frequency components to left and right circularly polarized. The rise time of the gating AOM for the dye laser was measured to be less than 16ns. A green diode laser at 532nm is used for non-resonant initialization into the state $m_s=0$ and to reverse possible ionization of the negatively charged NV into the neutral state NV^0.
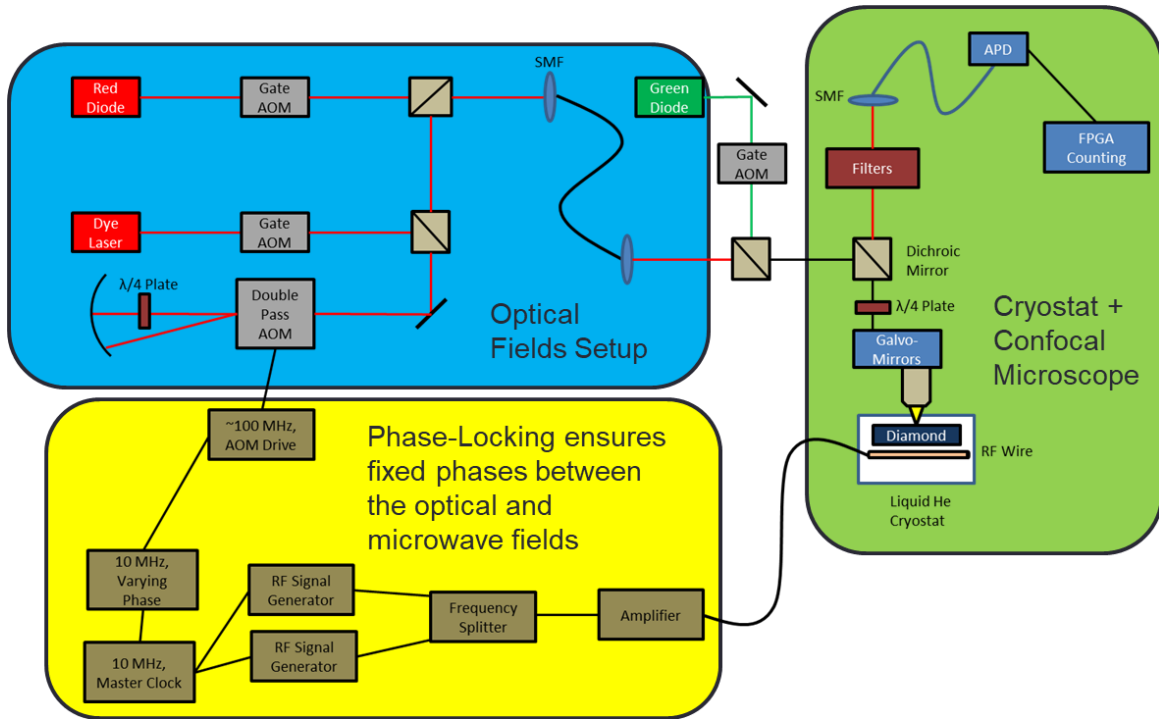
Figure 11: Schematic of experimental setup used for phase transfer experiment.

The confocal microscope has filters which ensure that the majority of collected light is from the PSB to reduce noise from the on-resonant laser fields. An APD is used to collect fluoresce and its signal is sent to a FPGA board that bins the photon counts with a time resolution of 2.8ns (external clock frequency of 300MHz).

In order ensure that the phase of all the fields is constant and well controlled, a phase-locking electronic setup is used. Only the phase relation of the two microwave signals generators and the double-pass AOM are important, all other AOMs are used for gating the various optical fields. For the case of the microwave state preparation followed by optical (time-resolved) readout, the two RF signal generators, at 2.770 GHz and 2.982 GHz, have their external references connected to the same 10MHz clock ("master"). A second 10MHz generator connects to the master and then sends a reference signal to the

~100MHz single generator driving the double-pass AOM. The second 10MHz generator then scans over a phase which maps onto a phase difference between the 1st and 0th order beams passing through the AOM. The overall phase of the dye laser does not affect the generated optical dark state. The range the 10MHz signal needs to be scanned depends on the frequency ratio of the 10MHz signal to the driving signal:

$$\Delta\phi_{Optical} = 2 \cdot \Delta\phi_{AOM} = 2 \cdot \frac{100MHz}{10MHz} \Delta\phi_{10MHz}$$

(15)

For example, to scan a range of 2π for the optical phase, the 10MHz reference signal is scanned a $\pi/10$ range. The factor of 2 is due to the optical field being double passed, as both its frequency and phase are modified by the AOM twice.

For the case of the optical preparation with microwave readout, an altered configuration is used. The 10 MHz master is connected to one RF signal generator and the double pass AOM driver. The second 10 MHz signal is sent to the remaining RF signal generator, which then has its relative phase to the other RF signal scanned. A similar equation gives the microwave phase difference as a function of the 10 MHz reference phase:

$$\Delta\phi_{MW} = \frac{2770MHz}{10MHz} \Delta\phi_{10MHz}$$

(16)

4.4 Phase Readout

To retrieve the phase information, we apply two optical fields, which have opposite circular polarization and equal Rabi frequency and are resonant with the respective circularly-polarized optical transitions. The two optical fields are Raman resonant with the $m_s=\pm1$ states unless otherwise specified and feature a well-defined relative phase, $\phi_{opt} = \phi_+ - \phi_-$, where $\phi_\pm$ are the initial phases of the optical fields coupling to the $m_s=\pm1$ states. Under these conditions, a superposition spin state given by

$$|D> = (e^{i\theta}|+1> -|-1>)/\sqrt{2} \qquad (17)$$

is effectively decoupled from the optical fields. This state is the optical dark state. Optical excitations to $|A_2>$ take place via the bright state,

$$|B> = (e^{i\theta}|+1> +|-1>)/\sqrt{2} \qquad (18)$$

which is orthogonal to $|D>$.

The superposition spin state created by the microwave fields can be expressed in the basis of the optical dark and bright states,

$$|\psi> = \frac{1}{2}[(e^{i(\theta-\varphi_{opt})} + 1)|B> +(e^{i(\theta-\varphi_{opt})} - 1)|D>] \qquad (19)$$

38

The optical excitation (i.e. population in |A₂>) should scale linearly with the population in |B>, which depends on the relationship between θ and ϕ_{opt}, as shown in Eq. 19. The optical readout process, however, can also drive the superposition state into the optical dark state through optical pumping, erasing the phase information encoded by the microwave fields. It is thus essential that the optical readout be performed in a timescale short compared with or at least comparable to the optical pumping time to the dark state (which is around 30 ns, as will be discussed later).

Figure 12b shows the fluorescence from |A₂>, collected during the first 28 ns, as a function of φ_{opt}. The sinusoidal oscillation of the fluorescence in Fig. 12b demonstrates the effective readout of the relative phase of the superposition spin state by the optical fields. Specifically, the maximum in the oscillation occurs when φ_{opt} and θ are in phase. The minimum occurs when φ_{opt} and θ are π out of phase, for which the electron is initially trapped in the optical dark state. Figure 12c also shows examples of time-resolved fluorescence obtained near a maximum and a minimum of the oscillation. Note that the relative optical (or microwave) phases plotted in Fig. 12 can differ respectively from φ_{opt} (or φ_{mw}) by a constant.

The visibility of the sinusoidal oscillations provides important information on the dynamics underlying the phase transfer process. Figure 12d plots the visibility, defined as $(I_{max} - I_{min})/(I_{max} + I_{min})$, as a function of the fluorescence detection time, for which $t=0$ corresponds to the leading edge of the optical pulse. The data points in Fig. 12d are derived from the fit sinusoidal oscillations of the fluorescence as a function of φ_{opt} with the fluorescence collected during a fixed time span of 28 ns. For the numerical fit in Fig. 12d,

we used the decay times derived from the corresponding time-resolved fluorescence experiments. The only fitting parameter is the visibility at t=0.
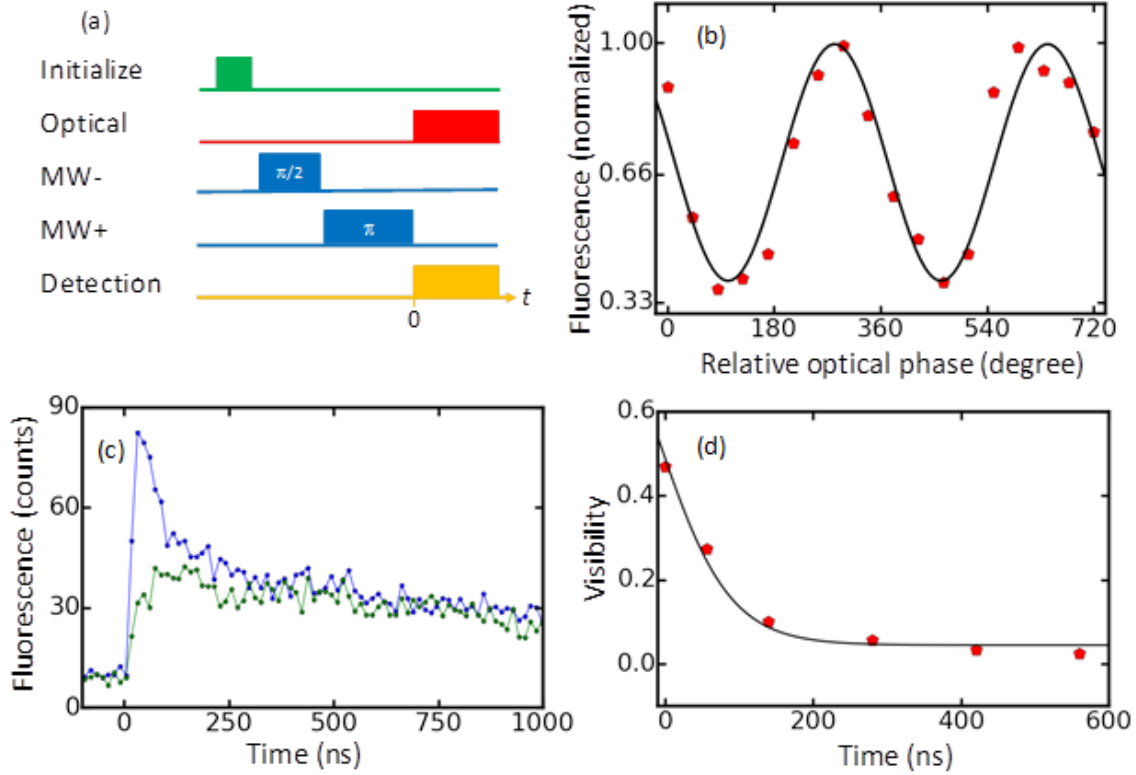
Figure 12: MW to optical phase transfer. (a) Pulse sequence for the transfer of phase information from microwave to optical fields. A NV is initialized in the m_s=0 state with an 8 ms green laser pulse. The two MW pulses prepare the NV in a superposition of m_s=± 1 states. The Raman-resonant optical pulse pair then retrieves the phase information of the superposition spin state. (b) Fluorescence from state A_2 detected during the initial 28 ns as a function of relative optical phase. The solid curve is a least-square fit to a sinusoidal oscillation with period 2p, with the peak normalized to 1. (c) Fluorescence from state A_2 as a function of time. The upper (lower) curves are obtained with ϕ_{opt} near a maximum (minimum) of the oscillations in (b). (d) Visibility of the sinusoidal oscillations as a function of fluorescence detection time, derived from experiments similar to those shown in (b). The solid line shows the results of a numerical fit using the decay time derived from the time-resolved fluorescence.

The maximum fringe visibility observed is limited by the fact that the dark state is not completely "dark" due to spin decoherence. In this regard, the maximum visibility is

40

closely related to the depth of the CPT dip in Fig. 13a. We can further improve the visibility by reducing spin dephasing, for example, using isotopically-purified diamond or dressed spin states[46].

To understand the decay of the visibility shown in Fig. 12d, we have carried out CPT experiments, for which the NV is initially prepared in $|-1>$. Figure 13a shows the fluorescence from $|A_2>$ measured as a function of the detuning between the two optical fields. The dip in the spectral response corresponds to CPT and occurs when the relative laser detuning satisfies the Raman resonant condition. The spectral width of the dip provides an independent measurement of the optical Rabi frequency[46], which agrees with that determined from the power broadening of the dipole optical transition.

The CPT shown in Fig. 12a arises from optical pumping of the NV center into the dark state. The dynamics of this pumping process is revealed in the time-resolved florescence from $|A_2>$ shown in Fig. 12b. For reference, we first set the detuning to be 20 MHz off the Raman resonance such that dark states cannot be formed. In this case, a decay time of 450 ns is observed. This decay arises from optical pumping into the $m_s=0$ state due to state mixing induced by residual strain[46]. We then set the detuning to be at the Raman resonance. The time-resolved florescence now features a much faster decay, with a decay time of 31 ns. This decay time, which is on the order of spontaneous emission lifetime of $|A_2>$, corresponds to the optical pumping of the NV center into the dark state and sets the timescale for the formation of the dark state. In this regard, Fig. 11d confirms that the decay of the visibility is determined by this optical pumping process, which is much faster than the spin decoherence time.
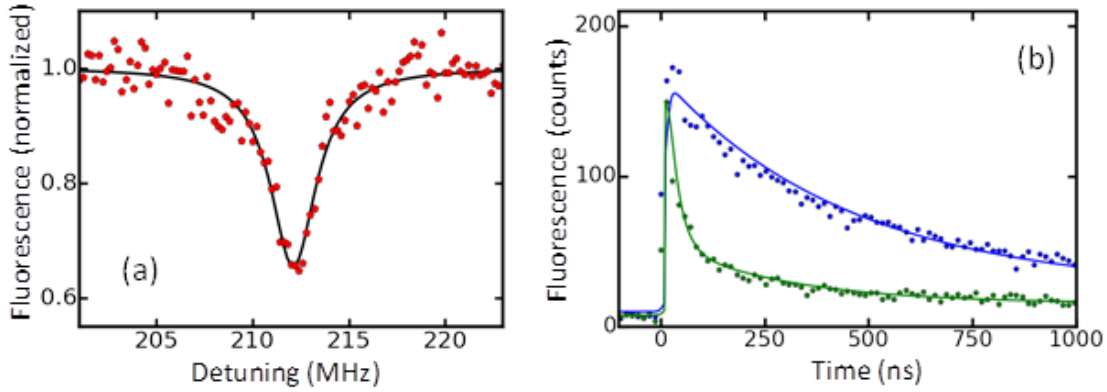
Figure 13: Dark state formation in the NV. (a) Fluorescence from state A_2 as a function of the detuning between two applied optical fields, showing the spectral response for CPT. The solid line shows a least-square fit of the dip to an inverted Lorentzian, with a linewidth of 2.8 MHz and with the baseline normalized to 1. (b) Fluorescence from A_2 as a function of time. The upper (lower) curve is obtained when the optical detuning satisfies (is 20 MHz away from) the Raman resonance. The solid lines show least-square fits to exponentials, with a decay time of 450 ns for the upper curve. Two decay times, 31 ns and 450 ns, are used for the lower curve.

4.5 Optical Phase Preparation and Readout

We now turn to the process that encodes the relative optical phase into the superposition spin state and then retrieves the phase with microwave fields. In this case, two Raman resonant optical fields with equal Rabi frequency and a well-defined relative phase prepare an optical dark state via the optical pumping process discussed above. Here, the optical pumping plays the crucial role in driving the NV center into a dark state, which has a relative phase set by φ_{opt}. As indicated in Fig. 14a, we use two microwave fields with equal Rabi frequency and a well-defined relative phase φ_{mw} to drive the electron in the optically-dark superposition spin state to the $m_s=0$ state and then detect the population in the $m_s=0$ state via the resonant E_y transition. The duration of the two microwave fields is set to $\tau = \pi / \sqrt{2}\overline{\Omega}$, where $\overline{\Omega}$ is the Rabi frequency for the individual microwave fields.

42

When φ_{mw} is in phase with φ_{opt}, the superposition spin state is not only a dark state for the optical fields, but also a dark state for the microwave fields. In this case, the electron spin is also decoupled from the microwave fields, preventing the transfer of the electron population back to the $m_s=0$ state. This leads to a minimum in the fluorescence from the E_y state. For comparison, in the limit that φ_{mw} is π out of phase with φ_{opt}, the superposition state becomes a bright state for the microwave fields. In this case, the pair of microwave fields serves as a π-pulse, driving the electron from the superposition spin state to the $m_s=0$ state and thus leading to a maximum in the measured fluorescence. Figure 14b shows the sinusoidal oscillation of the fluorescence from the E_y state as a function of φ_{mw}. The visibility derived from experiments similar to Fig. 12b are plotted in Fig. 14c as a function of the delay between the optical-encoding and microwave-readout pulses. The relatively long decay observed in Fig. 14c is primarily due to the spin dephasing induced by the fluctuating nuclear spin environment. The decay time obtained (0.6 ms) is in agreement with the expected spin dephasing time (T_2*). Note that because of the long spin lifetime, microwave fields are not effective in pumping the electron into a microwave dark state.

The visibility for the microwave readout shown in Fig. 14 is limited to a maximum of 1/5 because of the hyperfine coupling the NV electron spin to the nitrogen nuclear spin. Since the microwave fields used in our experiments were resonant to only one set of hyperfine states and no additional nuclear spin preparation was performed, on average 2/3 of the electron population remains in the $m_s=0$ state and does not participate in the transfer of phase information. Greater fringe contrast can be achieved with nuclear spin preparation[47].
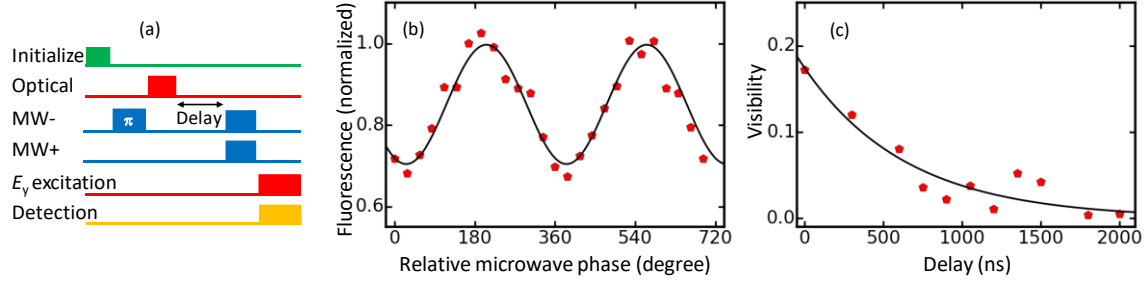
Figure 14: Optical to MW phase transfer. (a) Pulse sequence for the transfer of phase information from optical to microwave fields. Following an initialization green laser pulse, a MW π-pulse puts the NV in the m_s=-1 state. The Raman resonant optical pulse pair then prepares the NV in a dark state. A pair of MW pulses read out the phase of the dark state by driving the NV from the dark state to the m_s=0 state. Population in state m_s=0 is detected via a resonant excitation to the E_y excited state. (b) Fluorescence from state E_y as a function of relative microwave phase. The solid curve is a least-square fit to a sinusoidal oscillation with period 2π and with the peak normalized to 1. (c) Visibility of the sinusoidal oscillations as a function of the delay between optical-encoding and microwave-readout pulses. The solid line shows a least-square fit to an exponential with a decay time of 0.6 ms.

4.6 Summary

The dark-state based coherent coupling between microwave and optical fields demonstrated above can in principle enable the full quantum state transfer between optical and microwave fields, if an ensemble of NV centers, instead of a single NV center, is used. In this case, the quantum state mapping takes place via a propagating dark state or a dark-state polariton[48]. While there are still considerable technical challenges for using an ensemble of NV centers including inhomogeneous broadening of the NV centers, it is promising to develop a spin-based interface that can enable superconducting circuits to function in hybrid quantum systems.

CHAPTER V

PHONONIC COUPLING THEORY

5.1 Introduction

Vast amounts of experimental effort have been dedicated towards coupling NVs together and integrating them into larger and more complex quantum networks. Many of these implementations have used optical photons, microwave photons and collective electronic excitations within the diamond as the mediator to these couplings[25]. However, one promising method for coupling would be via the collective mechanical excitations of the diamond host containing the NV centers. Unlike photons, phonons have much slower velocities, allowing for less stringent timing requirements on chip. In addition, phonons cannot propagate in vacuum, allowing for the easier creation of highly isolated, low loss systems with mechanical oscillations as opposed to optical ones. This opens the possibility for long range coherent interactions between qubits which are mediated by phonon modes instead of optical or MW ones. As was shown in previous chapters, both the NV ground and excited state couple, via both state splitting and mixing, to strain. As such, diamond mechanical resonators carrying NV centers provide a promising physical platform for the control of both spin and mechanical degrees of freedom as well as the use of mechanical oscillations in quantum information processing using NV centers.

As will be shown, the efficiency of the NV-phonon coupling can generally be described by the cooperativity which can be given as $C = g^2/\gamma\Gamma$, where g is the single phonon coupling rate to the NV while γ and Γ are the dissipation rates of the NV two level

system and mechanical resonator respectively. It is generally stated that a system with C>1 is in the regime of "quantum coupling" as the interactions between the qubit and mechanical motion are strong enough to show quantum effects before the two systems individually decohere. Achieving this regime in a NV-phonon system will allow for a number of useful applications such as the creation of squeeze mechanical states[49], cooling of a mechanical resonator to its ground state[50] and spin-phonon entanglement[51].

5.2 Related/Previous Work

Much work has already been done on NV center phonon coupling, the majority of which has been with externally driven phonons interacting with the NV center ground state spins. Work in characterizing the ground state strain response was performed by P. Ovartchaiyapong *et al.* [19] where a cantilever with a fundamental mechanical mode of 800 kHz was actuated by a piezoelectric transducer. The effects of the strain coupling to the spin transitions were observed in a Hahn echo pulse sequence which showed the detuning of the ground state energy levels due to their strain coupling.

One main advantage of using phonons for quantum control in the ground state is that magnetic dipole forbidden transitions such as |-1> to |+1> cannot be effectively driven with the standard MW field driving in the NV ground state, but can be driven due to the strain coupling present in the ground state Hamiltonian. In an NV ensemble, MacQuarrie *et al*. [52] demonstrated Rabi oscillations between the |±1> states and an increased coherence time T_2^* in the ground state using phonon dressed states which are decoupled from first order magnetic field noise caused by the nuclear spin environment (Fig. 15a). In

this experiment, a high overtone bulk acoustic resonator (HBAR) was used with a fabricated piezoelectric and electrode to excite the modes of up to 1 GHz. Additional work in the realm of ground state quantum control used a cantilever beam fabricated in the diamond sample and driven with a piezoelectric to perform Rabi oscillations on a single hyperfine sublevel of the NV ground state and observed the strain induced Autler-Townes splitting at an anti-crossing point for a given magnetic field in the ground state (Fig. 15b)[53].
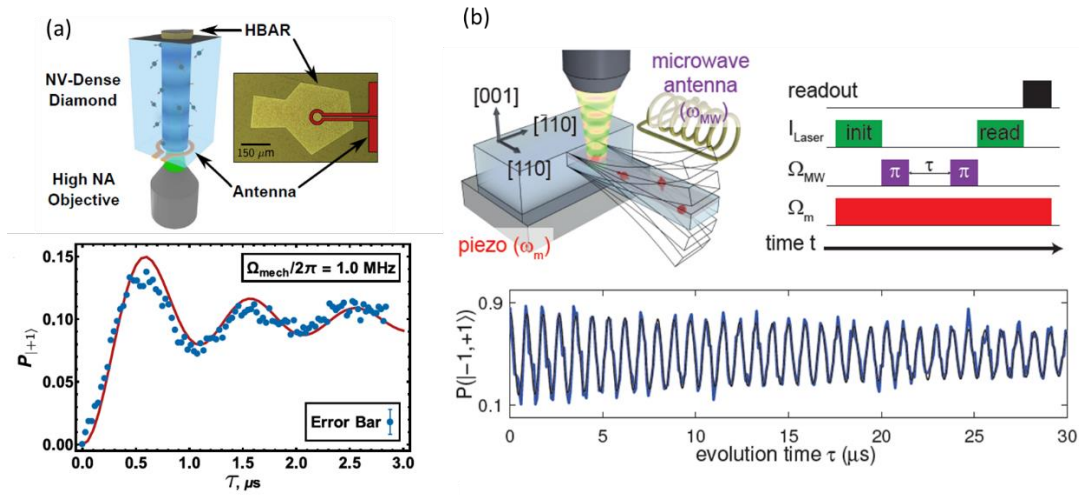
Figure 15: Driven NV-phonon experiments. (a) Upper: Schematic and picture of high-overtone bulk acoustic resonator (HBAR). Lower: Mechanically driven Rabi oscillations between the $|m_s=1>$ and $|m_s=-1>$ states. (Images from [52]). (b) Upper Left: Schematic of cantilever implementation of NV ground state driving. Upper Right: Pulse sequence for mechanically driven rabi oscillations. Lower: Strain driven Rabi oscillations (Images from [53]).

As opposed to work in the ground state, the NV excited state coupling has been less explored, due to the difficulties of creating coherent NVs in thin mechanical resonators, which will be discussed later. Previous work in [54] and [55] used interdigital transducers (IDTs) to drive surface acoustic waves (SAWs) on a diamond sample containing near

surface NV centers (Fig. 16a). The special property of the SAWs ensures that their induced displacement decays into the surface on a length scale determined by their wavelength. As such, most of the driven strain is near the surface, which results in higher orbital-phonon coupling rates. Golter *et al.* [54] fabricated an IDT on a bulk diamond sample with a resonant frequency of ~1GHz. Driving the SAW while performing PLE on a near surface NV revealed red and blue sidebands detuned by the mechanical drive frequency (Fig. 16b). The properties of this effect are comparable to the Stokes and anti-Stokes sidebands present in trapped ion/atoms, which can either absorb or emit mechanical quanta at some frequency to assist in an atomic transition. Setting the laser frequency to one of these sidebands allows for coherent, phonon assisted Rabi oscillations to be observed whose Rabi frequency depends on the strength of the mechanical driving (Fig. 16c). Further work with this system[55] preformed phonon assisted, optically driven spin transitions within a lambda system of the NV center. In this work, both the phonon-assisted coherent population trapping (Fig. 16d) and phonon assisted Raman spin transitions between the $|\pm 1\rangle$ ground states (Fig. 16e) were performed. This work was an important step in realizing spin-phonon coupling in the NV center, since the ground state spins are suitable systems for various quantum storage operations while the excited state, with its strong phonon coupling rate, mediates the phonon interaction between the spin states without introducing separate decoherence mechanisms.
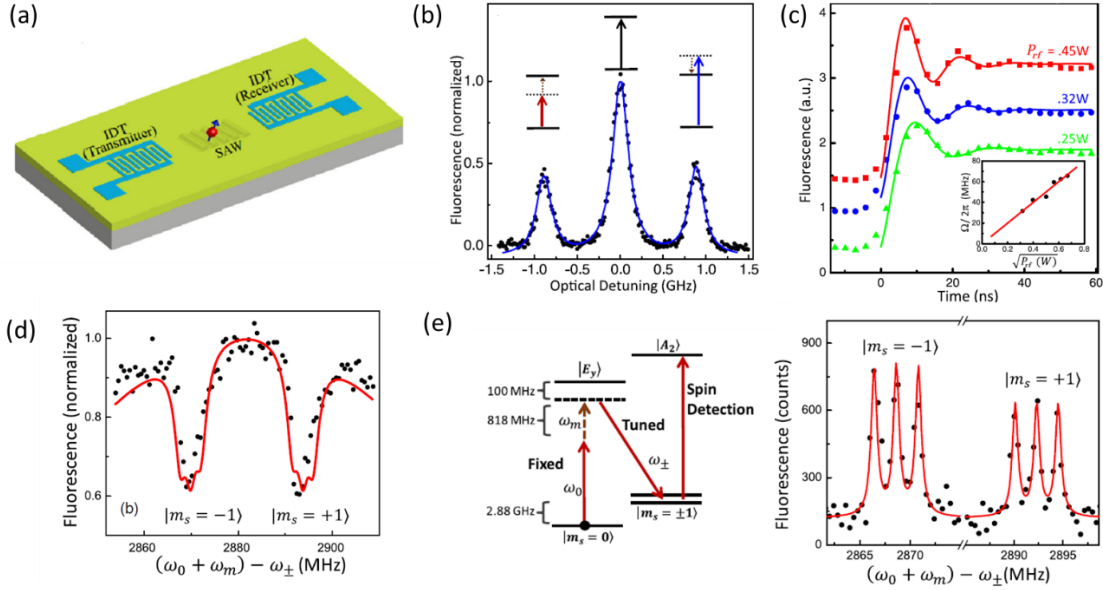
Figure 16: NV-phonon coupling in the excited state. (a) Schematic of SAW emitter and receiver on diamond surface. (b) Red and blue-detuned sideband of excited state NV transitions. The detuning of each is equal to ~900MHz, which is the drive frequency of the SAW. (c) Phonon assisted Rabi oscillations of the NV excited state. The laser frequency is detuned from the central transitions so it is on one of the sideband resonances. The RF drive power for the SAW is then varied, showing the SAW power dependence of the phonon-assisted Rabi frequency. (Images a-c from [54]). (d) Dark state formation with one of the optical drives being phonon assisted. (e) Left: Pulse sequence for optical, phonon-assisted Raman transitions between the $|m_s=0\rangle$ and $|m_s=\pm1\rangle$ spin ground states. Right: Frequency scan of the phonon-unassisted Raman drive field. Large fluorescence counts correspond to large population in the $|m_s=\pm1\rangle$ states. Because the effective Rabi frequency of the transition is lower than the hyperfine splitting, the hyperfine nuclear spin states of the $|m_s=\pm1\rangle$ are individually visible. (Images d and e from[55])

5.3 Optomechanical Theory

5.3.1 Optical Cavity

The ubiquitous system for understanding the optomechanical driving interaction is the optical cavity with one movable mirror on a spring. The radiation pressure from the light reflecting off the moveable mirror induces a force incident on the mirror, moving it which then alters the length of the optical cavity and changes the resonance condition for

49

the light inside it. The Hamiltonian for the cavity-mechanical system in the quantum

mechanical picture is given as ($\hbar$=1):

$$H = \omega_c(\hat{x})\hat{a}^\dagger\hat{a} + \omega_m\hat{b}^\dagger\hat{b} \tag{20}$$

with $\hat{a}$ and $\hat{b}$ being the annihilation operators for the optical cavity mode and mechanical

mode respectively. Assuming the frequency change due to the mirror motion is small

compared to the overall frequency, Taylor expanding the cavity resonance gives

$$\omega_c(\hat{x}) \approx \omega_c(0) + G\hat{x} \tag{21}$$

where $G = \frac{\partial\omega_c}{\partial x}\big|_{x=0}$. Plugging this expression into (20) and noting that $\hat{x} = x_{zpf}(\hat{b}^\dagger + \hat{b})$

with $x_{zpf} = \sqrt{\frac{\hbar}{2m_{eff}\omega_m}}$, we get the following:

$$H = \omega_c(0)\hat{a}^\dagger\hat{a} + \omega_m\hat{b}^\dagger\hat{b} + Gx_{zpf}(\hat{b}^\dagger + \hat{b})\hat{a}^\dagger\hat{a} \tag{22}$$

Notice the first two terms represent the Hamiltonian with a decoupled mechanical

oscillation and cavity frequency, while the third term represents the interaction between

the light and phonon mode. Oftentimes, the third term coefficient is expressed $g_0 =$

$G x_{zpf}$ where g_0 is the single-phonon coupling rate (i.e. the amount the cavity frequency

shifts due to the presence of one quanta in the mechanical mode).

5.3.2 NV-Phonon Coupling

The case where a mechanical oscillator couples to the energy levels of a two level NV system is similar to the results shown in Eqn. 20. The physical phenomena which couples the energy of the two-level system (TLS) in this case is perhaps less obvious than a moveable mirror in a cavity. The NV center is located in an ionic lattice of carbon and the positions of the carbon ions surrounding it determine the potential the unbound electrons of the NV center experience. Therefore, they also affect the transition energies of any orbital excitations the center might undergo. This phenomena is qualitatively given as the "deformation potential" *D*, where *D* is a factor describing how much the energy levels of the excited state of the NV change for a given strain (Note: strain is dimensionless and $\hbar$=1, so *D* will have dimensions of frequency in the following calculations). The interaction Hamiltonian for the NV orbital-phonon coupling is then given as:

$$H_{int} = D \, k_m x_{zpf} (\hat{b}^\dagger + \hat{b})|e\rangle\langle e| \tag{23}$$

with k_m the wavevector of the mechanical mode and the energy of the ground state set to 0. To the full two-level Hamiltonian with a driving optical field Ω_0 we apply the Schrieffer-Wolfe transformation [55]:

$$U = \exp\left[\frac{g}{\omega_m}(\hat{b}^\dagger - \hat{b})|e\rangle\langle e|\right] \tag{24}$$

and move to the interaction picture. This yields the expressions for the phonon-assisted transitions:

$$V = \frac{\Omega_0}{2}\frac{g}{\omega_m}(\hat{b}e^{i(\Delta_1 - \omega_m)t}|e\rangle\langle g| + h.c) \tag{25}$$

where Δ_1 is the detuning from resonance of the laser field. This expression is similar to the case in [55] except that there is a phonon operator present instead of a $\sqrt{n}$ present due to lack of external driving. In the following calculations, the state of the phonon mode will not be considered to be static with a mean number of phonons present (as in experiments with external phonon driving), but instead will evolve over time. Without driving, the effective rabi frequency $G = \frac{\Omega}{2}\frac{g}{\omega_m}$ is generally too small to see any dynamics such as red/blue sidebands. Because of this, it will be necessary to measure the interference of this phonon-assisted field with another driving field. The Heisenberg-Langevin equations for the interaction Hamiltonian is given by:

$$\dot{\sigma}_- = -\frac{\gamma_{TLS}}{2}\sigma_- - i\omega_0\sigma_- + iGb\sigma_z + F_\sigma + Ae^{-i\delta t}$$

$$\dot{b} = -\frac{\gamma_m}{2}b - i\omega_0 b - iG\sigma_- + F_b \tag{26}$$

where the γ's are the decoherence rates of the two level system and the mechanical resonator, A is the amplitude of the 2nd (resonant) drive field of the two level system and F_σ and F_b are the noise operators for their respective operators. Time averaging these operators ($p = <\sigma_->, \beta = <b>$), taking the weak excitation limit ($p \approx -1, <b\sigma_z> \approx$

$< b >$) and going into the frame rotating at the frequency of the drive detuning δ ($p = p'e^{-i\delta t}$, $\beta = \beta'e^{-i\delta t}$) we get the equations of motion:

$$\dot{p}' = -(i(\omega_0 - \delta) + \frac{\gamma_{TLS}}{2})p' - iG\beta + A$$

$$\dot{\beta}' = -\left(i(\omega_0 - \delta) + \frac{\gamma_m}{2}\right)\beta' - iGp \qquad (27)$$

Taking the steady state and solving for both these as a function of the laser detuning gets the following:

$$p' = \frac{2A}{\gamma_{TLS}}[1 - \frac{\frac{\gamma_m}{2}C}{i(\omega_0 - \delta) + (1+C)\frac{\gamma_m}{2}}]$$

$$\beta' = \frac{1}{iG}[A - \left(i(\omega_0 - \delta) + \frac{\gamma_{TLS}}{2}\right)(\frac{2A}{\gamma_{TLS}}\left[1 - \frac{\frac{\gamma_m}{2}C}{i(\omega_0 - \delta) + (1+C)\frac{\gamma_m}{2}}\right])] \qquad (28)$$

where the factor $C = \frac{4G^2}{\gamma_m\gamma_{TLS}}$ is the cooperativity. The steady state results of p' are plotted

in Figure 17. It should be noted that the measurement method for the NV-phonon coupling

proposed here and the results shown in Figure 17 are analogous to optomechanically-

induced transparency (OMIT) experiments performed with optomechanical resonators

such as microspheres and microtoroids[56].
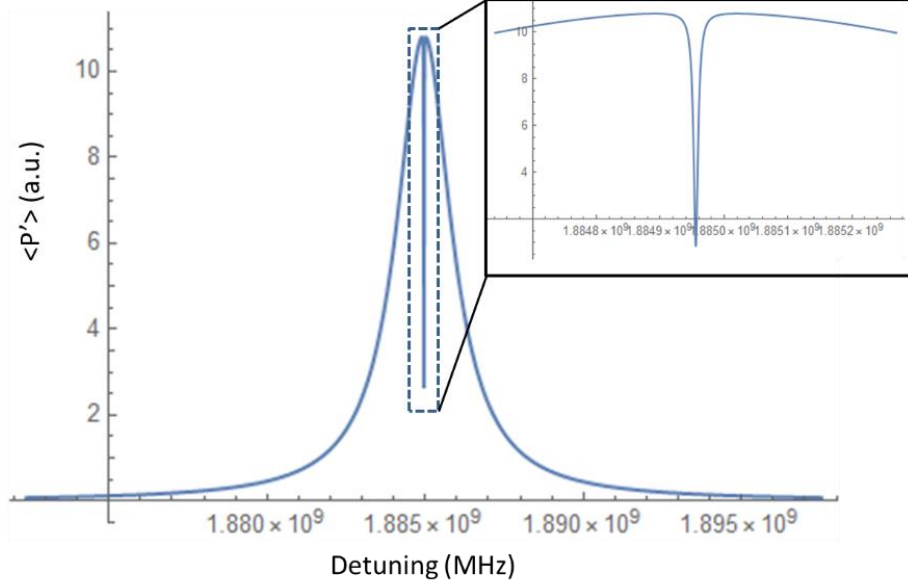
Figure 17: Graph of the expectation value of the dipole moment p' as a function of detuning δ. The dip in excited state population occurs once the detuning of the laser drive is on resonance with the detuning of the of the phonon assisted drive. Inset: Zoom in of the dip feature, the linewidth of the dip is approximately given by the linewidth of the mechanical mode, which is generally orders of magnitude smaller than most optical transition linewidths.

The cooperativity is the main factor determining the depth of the dip and as mentioned before, $C > 1$ is a critical threshold for allowing numerous quantum operations to occur with phonons as their intermediaries. Expressing the cooperativity $C = \frac{\hbar}{2m_{eff}} \frac{\Omega_0^2 D^2}{\gamma_m \gamma_{TLS}} \frac{1}{\omega_m}$, it is clear to see which factors we need to optimize for realizing $C > 1$. Small oscillator mass, small mechanical decoherence and small TLS decoherence are particularly critical, since the bare driving frequency Ω_0 and mechanical frequency ω_m are related in their limits, as a large Ω_0 broadens the transition and then requires a larger ω_m to be resolvable. Finally, as mentioned earlier, the deformation potential D of the NV center is nearly 5 orders of magnitude larger if the coupling takes place via an orbital excited state

54

rather than the spin triplet ground state[57], meaning utilization of the excited state is almost guaranteed to be a necessity for $C > 1$.

There are two implementations to this phonon assisted interference experiment with the NV center that I will discuss. The first is through the use of a pure excited state transition (to either $|E_y\rangle$ or $|E_x\rangle$) directly from the ground state (Fig. 18a). This is obviously the case calculated above where two fields in a TLS interfere to give the feature shown in Figure 17. The one restriction is that the phonon assisted transition should be resolvable, which puts a limit to how low ω_m can be based on the optical linewidth of the $|0\rangle \to |E_y\rangle$ transition. As will be explained in the following chapters, this is a significant limit for NVs in thin, <1μm mechanical resonators which are required for the mechanical mode to have a high Q. For a mechanical resonator $\omega_m/2\pi$ =1GHz, $\gamma_{TLS}/2\pi$=500MHz, $\Omega_0/2\pi$=100MHz and m_{eff}=1.2pg, a mechanical quality factor Q of $6.8*10^4$ is necessary to achieve C=1. This is a relatively high Q for such a high frequency mechanical resonator but should be achievable as discussed in the following chapters.

The alternative method, as employed in [55] is to instead use an effective two level transition between two of the spin triplet ground states (Fig. 18b). The NV is initialized into the $|-1\rangle$ state via a MW π-pulse, then pumped to the other spin state $|+1\rangle$ with two detuned optical fields with an effective Rabi frequency $\Omega_{eff} = \frac{\Omega_-\Omega_+}{4\Delta}$. As long as the overall detuning Δ is sufficiently large, the excited state $|A_2\rangle$ is never significantly populated and the fast spontaneous emission time of the excited state is not an issue in the population transfer. Figure 16e gives an example of the driven spin control experiment and shows that with sufficiently low Ω_{eff} the hyperfine ground states can be individually resolved. This

implementation of the NV phonon coupling is particularly important due to the vast amount of experiments and methods utilizing the NV electron and nuclear spins for quantum information processes. Additionally, though the transition process is facilitated by optical fields, the relevant linewidths are the spin transition linewidths and not the optical linewidths. Therefore, much lower frequency resonators will be needed to be in the resolved sideband regime. However, the additionally MW driving and the need for four overall optical fields (three for the Raman transition, one for the readout) complicates the experimental setup compared to the direct sideband transition. For a mechanical resonator $\omega_m/2\pi$ =2MHz, $\gamma_{TLS}/2\pi$=1MHz, $\Omega_0/2\pi$=1MHz and m_{eff}=2.4pg, a mechanical quality factor Q of 10^5 is necessary to achieve C=1. Quality factors this high have been achieved in thin diamond membranes at cryogenic temperatures[58].
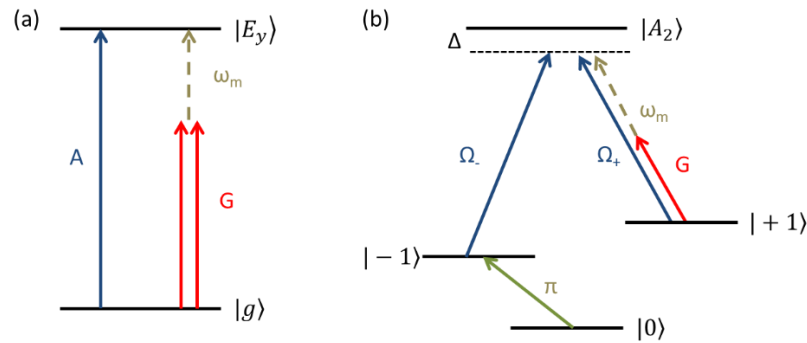
Figure 18: OMIT-like experiment to characterize single phonon coupling. (a) Case of orbital-phonon coupling: Direct sideband transition with resonant optical driving field A and off-resonant optical drive G on the red sideband of the transition. (b) Case of spin-phonon coupling: A MW π pulse initializes the state into the $|-1\rangle$ ground state. Two Raman resonant optical fields Ω_- and Ω_+ induce a transition between the $|-1\rangle$ and $|+1\rangle$ ground states with an overall detuning Δ. A third, off-resonant optical drive field G will show interference effects when it is detuned from Raman resonance by exactly the mechanical drive frequency.

5.4 Summary

The NV center in diamond can couple to the mechanical vibrations of its host crystal and modulate its energy levels to perform both orbital-phonon and spin-phonon coupling experiments. In theory, the fully quantum C=1 regime can be achieved while using the excited state of the NV center rather than the ground state spin transitions. The requirements placed on the mechanical resonators suggest that high Q and low mass are necessary for both cases. The experiment to measure this coupling is comparable to OMIT type experiments done before in optomechanical systems.

CHAPTER VI

MECHANICAL RESONATORS

6.1 Introduction

The field of high quality factor mechanical resonators greatly predates the field of quantum information science. Mechanical resonators have been used as time keeping devices for centuries, while more modern applications have ranged from precision mass sensing to gravitational wave detection[59]. In the context of NV-phonon coupling, the cooperativity C of the interaction can be improved by designing a low mass and high Q resonator. The requirement of the interaction being in the resolved sideband regime of the two-level transition gives a lower bound for the frequency of the mechanical resonator to be used. Since the optical and spin transition linewidths are orders of magnitude different to one another in the schemes shown in Figure 18, this suggests that vastly different resonator designs will be required for the two experiments.

6.2 Diamond Cantilevers

Diamond, due to its extremely high Young's Modulus and low intrinsic loss, makes an excellent material for mechanical resonators, though its chemical inertness presents a challenge for fabrication. Recently, thin cantilever resonators from single crystal diamond have been fabricated using inductively coupled plasma (ICP) etching techniques[58], [60]. The devices are long and thin (Figure 19a), meaning they have relatively low frequencies on the order of 10s of kHz. For our purposes, shorter and thicker cantilever with mechanical

frequencies of a minimal 1-2MHz would be necessary for the spin-phonon coupling experiment. In addition, Figure 19b shows that cooling a cantilever made of electronic grade single-crystal diamond leads to an order of magnitude increase of the quality factor due to the main dissipation mechanism (in this case surface friction) being suppressed at cryogenic temperatures. These results suggest that the mechanical resonator design in the case of the phonon-assisted spin transition is relatively straightforward, as cantilevers are one of the most ubiquitous nanomechanical resonator systems.
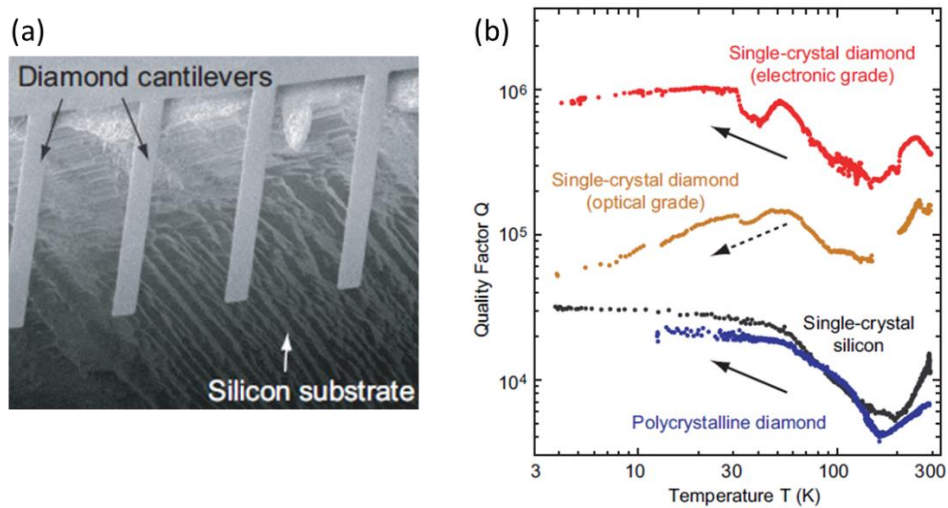
Figure 19: Diamond cantilevers. (a) SEM image of 100nm thick diamond resonators. (b) Quality factors vs. temperature comparisons between various types of diamond and Si. (Images from [58])

6.3 Lamb Wave Modes

6.3.1 Overview

Designing and fabricating a thin diamond cantilever with NVs seems like the easiest way to realize the requirements for the phonon assisted Raman process. However,

the direct sideband method (i.e. orbital-phonon) is complicated by the need for a very high frequency mechanical resonator. Here, we turn to the surface acoustic wave modes used in the experiments done in [54] and [55]. SAW modes are a special type of Rayleigh wave which exists in a semi-infinite medium and which have most of their mode volume within one acoustic wavelength of the surface of the semi-infinite plane. As shown in Figure 16b, the frequency of SAWs must be sufficiently high for the direct sideband transition to be resolved from the >100MHz linewidth of the NV's optical transition. However, the requirements needed to achieve high cooperativity in the orbital-phonon experiment necessitate a small effective mass of the oscillator. Thankfully, similar Rayleigh waves exist in a medium which is not semi-infinite but has a thickness comparable to the wavelength of the mode, which are known as Lamb waves[61].

6.3.2 Theory

Lamb waves are guided acoustic waves propagating in a thin plate of elastic material. To understand their properties first we derive the theory for Rayleigh waves, a type of acoustic wave which propagates along the surface of an elastic solid and whose displacements decay exponentially as a function of depth from the surface[62].

First we assume our medium is linear and elastic, meaning that the force on a single particle in the medium is proportional to its displacement from its equilibrium position and the equilibrium position does not change/distort over time:

$$T_{ij} = \sum_{k,l} c_{ijkl} S_{kl} \tag{29}$$

60

Here, T is the stress tensor (units of force/area), c is the "stiffness" tensor and $S_{ij}(x_1, x_2, x_3) = \frac{1}{2}(\frac{\partial u_i}{\partial x_j} + \frac{\partial u_j}{\partial x_i})$ is the strain tensor, where u_i is a particle's displacement from equilibrium in the ith direction. This is essentially a fully generalized version of Hooke's law. Additionally, though c appears to have 81 components, symmetries greatly reduce its complexity (ex. a cubic crystal has only 3 independent components). Now consider a cube of side length δ. The forces on one of the x_1 facing sides equal $\delta^2 T_{i1}(x'_1 + \frac{\delta}{2}, x'_2, x'_3)$ which, taking δ small and summing the forces, gives $\delta^3 \sum_j (\frac{\partial T_{ij}}{\partial x_j})$. This force must be caused by accelerations of the internal displacement vectors, $\rho\delta^3(\frac{\partial^2 u_i}{\partial t^2})$ therefore our equation of motion is:

$$\sum_j \left(\frac{\partial T_{ij}}{\partial x_j}\right) = \rho\left(\frac{\partial^2 u_i}{\partial t^2}\right) \tag{30}$$

For simplicity we assume our medium is isotropic, in which case the stiffness tensor only has 2 independent components λ and μ (called Lamé constants): $c_{ijkl} = \lambda\delta_{ij}\delta_{kl} + \mu(\delta_{ik}\delta_{jl} + \delta_{il}\delta_{jk})$. Plugging c into our expression for T leads to

$$\rho\left(\frac{\partial^2 u_i}{\partial t^2}\right) = (\lambda + \mu)\frac{\partial}{\partial x_i}(\nabla \cdot u) + \mu\nabla^2 u_i \tag{31}$$

and assuming a plane wave solution for u gives:

$$\omega^2\rho\,\vec{u_0} = (\lambda + \mu)(\vec{k}\cdot\vec{u_0})\vec{k} + \mu|\vec{k}|^2\vec{u_0} \tag{32}$$

Two cases of interest are for waves with purely longitudinal displacements ($(\vec{k} \cdot \vec{u}_0) =$ $|\vec{k}||\vec{u}_0|$) and purely transverse displacements ($(\vec{k} \cdot \vec{u}_0) = 0$) which will have $V_l = \sqrt{\frac{\lambda+2\mu}{\rho}}$

and $V_t = \sqrt{\frac{\mu}{\rho}}$ phase velocities respectively.

For the scenario of waves propagating at the surface of a medium, consider a "half-space" which consists of a linear elastic medium for z<0 , vacuum in z>0, the wave propagating in the x direction and the wavefront parallel to the y direction. Assuming the SAW is composed of a longitudinal and transverse wave with wavevectors $\vec{k}_l = (\beta, 0, L)$ and $\vec{k}_t = (\beta, 0, T)$, the displacements are therefore

$$\vec{u_l} = A \left(1, 0, \frac{L}{\beta}\right) e^{-i(\beta x + Lz)} \tag{33}$$

$$\vec{u_t} = B \left(1, 0, -\frac{\beta}{T}\right) e^{-i(\beta x + Lz)} \tag{34}$$

Here, β is the wavevector of the SAW propagating in the x direction, $T^2 = \frac{\omega^2}{v_t^2} - \beta^2$ and $L^2 = \frac{\omega^2}{v_l^2} - \beta^2$. Plugging the sum of these displacements into our expression for T_{ij} and requiring that the stresses are zero at the surface ($T_{13} = T_{33} = 0$) gives two homogeneous equations which, requiring the determinant of A and B to be zero, gives:

$$\left(2 - \frac{v^2}{v_t^2}\right)^2 = 4\sqrt{1 - \frac{v^2}{v_t^2}}\sqrt{1 - \frac{v^2}{v_l^2}} \tag{35}$$

where v is the SAW velocity. These boundary conditions also solve the x and z components of the displacements (up to an arbitrary factor):

$$u_x = \left(\gamma e^{a\beta z} - e^{b\beta z}\right)e^{i(\omega t - \beta x)} \tag{36}$$

$$u_z = i\left(\gamma a e^{a\beta z} - \frac{1}{b}e^{b\beta z}\right)e^{i(\omega t - \beta x)} \tag{37}$$

where $a = -i\frac{L}{\beta}$, $b = -i\frac{T}{\beta}$ and $\gamma = (2 - \frac{v_R^2}{v_t^2})/(2ab)$. Note that L and T are positive imaginary while β is positive real, therefore a, b and γ are real positive, so the displacement amplitudes decay in the –z direction as desired. Additionally, the two displacement amplitudes are in quadrature with one another, therefore the overall displacement will be elliptical.

For Lamb waves, a similar analysis follows. Instead of a half space, take our medium to span the entire x and y axes but only –d to +d in the z axis. We can no longer claim the displacement amplitudes decay quickly in the z direction therefore our new transverse and longitudinal displacements will be $\vec{u}_l = C(1,0,L/\beta)e^{(-i(\beta x + Lz))} + D(1,0,-L/\beta)e^{(-i(\beta x - Lz))}$ and $\vec{u}_t = A(1,0,-\beta/T)e^{(-i(\beta x + Tz))} + B(1,0,\beta/T)e^{(-i(\beta x - Tz))}$. The boundary conditions of $T_{13} = T_{33} = 0$ at z=±d lead to 2 sets of 2 linear, homogeneous equations which have non-trivial solutions when their determinants are zero, giving two characteristic equations:

$$(k^2 + T^2)\cosh(Ld)\sinh(Td) - (4k^2 TL)\sinh(Ld)\cosh(Td) = 0 \tag{38}$$

$$(k^2 + T^2)\sinh(Ld)\cosh(Td) - (4k^2 TL)\cosh(Ld)\sinh(Td) = 0 \tag{39}$$

The solutions to each of these gives wavevectors symmetric and anti-symmetric wavevectors k_s and k_a respectively. Solving for the displacements in both cases (up to an arbitrary constant) gives:

$$u_{x,s} = -ik_s \left(\frac{\cosh(L_s z)}{\sinh(L_s d)} - \frac{2L_s T_s}{k_s^2 + T_s^2} \frac{\cosh(t_s z)}{\sinh(T_s d)} \right) e^{i(k_s x - \omega t)} \tag{40}$$

$$u_{z,s} = -L_s \left(\frac{\sinh(L_s z)}{\sinh(L_s d)} - \frac{2k_s^2}{k_s^2 + T_s^2} \frac{\sinh(t_s z)}{\sinh(T_s d)} \right) e^{i(k_s x - \omega t)} \tag{41}$$

$$u_{x,a} = -ik_a \left(\frac{\sinh(L_a z)}{\cosh(L_a d)} - \frac{2L_a T_a}{k_a^2 + T_a^2} \frac{\sinh(T_a z)}{\sinh(T_a d)} \right) e^{i(k_a x - \omega t)} \tag{42}$$

$$u_{z,a} = -L_s \left(\frac{\cosh(L_a z)}{\cosh(L_a d)} - \frac{2k_a^2}{k_a^2 + T_a^2} \frac{\cosh(T_a z)}{\cosh(T_a d)} \right) e^{i(k_a x - \omega t)} \tag{43}$$

Here $T_s^2 = \frac{\omega^2}{v_t^2} - k_s^2$ and $L_s^2 = \frac{\omega^2}{v_l^2} - k_s^2$ with analogous expressions for T_a and L_a. The first solution has z displacements which are symmetric with respect to z=0 while the second is anti-symmetric. The number of symmetric or anti-symmetric modes allowed in a plate of thickness 2d is given by the number of real roots of their respective characteristic equations which are given by $N_s = 1 + [2\frac{d}{\lambda_t}] + [2\frac{d}{\lambda_l} + \frac{1}{2}]$ and $N_a = 1 + [2\frac{d}{\lambda_l}] + [2\frac{d}{\lambda_t} + \frac{1}{2}]$ where λ_l and λ_t are wavelengths for longitudinal and transverse waves at a given frequency and the brackets take the nearest integer value of their arguments. The phase velocities for the 0th order symmetric and anti-symmetric modes, which are calculated through their respective characteristic equations, are shown for an Aluminum Nitride plate (Fig. 20). Key features to note are that the Lamb modes asymptotically converge to SAWs

in the limit of plate thickness >> wavelength and the 0th symmetric mode has very low dispersion for a thin plate.
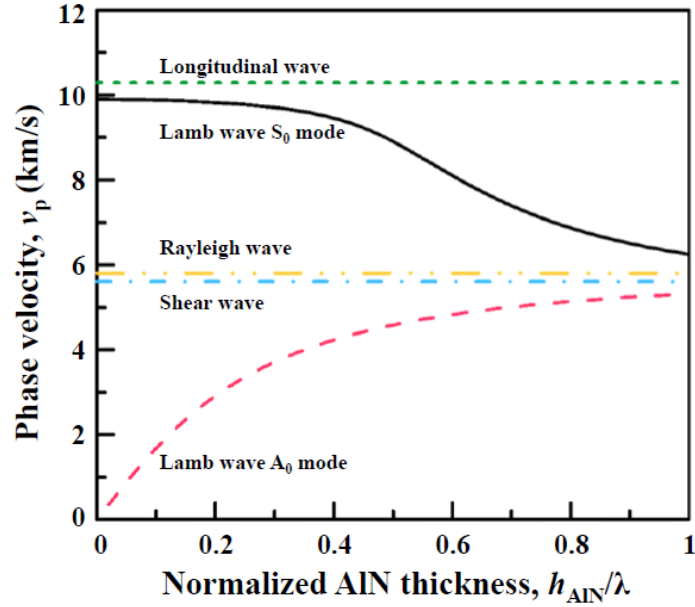
Figure 20: Phase velocities of the 0th order Lamb modes vs. normalized wavenumber. Shear, longitudinal and Rayleigh/SAW cases are shown for comparison (image from [61]).

6.4 Finite Element Analysis

Although analytic solutions for an isotropic medium give insight into general properties of Lamb waves, the increased complexity of a finite and anisotropic crystal medium will be evaluated numerically with COMSOL finite element analysis (FEA). The goal in this analysis will be to calculate at what frequency certain mechanical modes appear, which modes are preferred and how the system geometry changes the quality factors of each mode. The calculation for the Lamb wave resonator is particularly crucial since the symmetric wave Lamb mode has primarily in plane vibrations, meaning that it

cannot be measured with a standard laser interferometry setup like the fundamental cantilever mode. The main way to confirm the quality factor and frequency of the Lamb mode will be via its coupling to the energy levels of a solid state defect. Since the dip shown in Figure 17 has a width primarily determined by the linewidth of the mechanical mode, this means that the detuning frequency of the phonon assisted field will need to be scanned with a resolution lower than that of the mechanical linewidth. Therefore, the accuracy of the simulation calculating the frequency of the Lamb wave mode is of significant importance.

Firstly, the mechanical mode of interest will have its resonance frequency simulated for a given geometry. In the case of Lamb wave modes, assuming the wave propagates in the <100> direction of the diamond, an eigenfrequency analysis is performed to find the frequencies at which the Lamb modes appear. Pictured in Figure 21 are the 0th order antisymmetric and symmetric modes for a 30um x 15.6um x .9um geometry, which appear at 54MHz and 286MHz respectively.
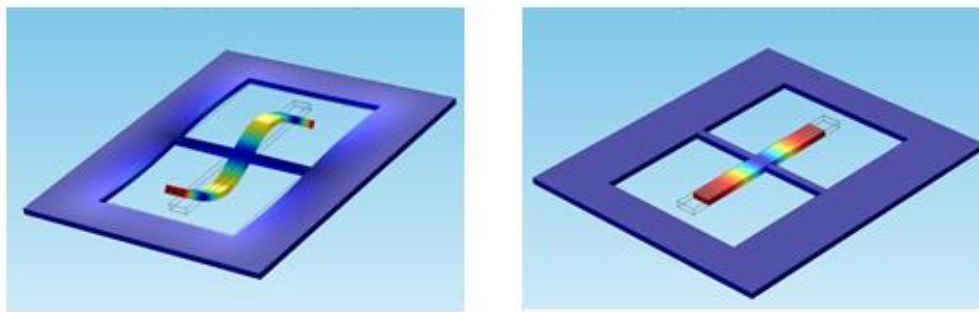
Figure 21: Displacements for 0th anti-symmetric (left) and symmetric (right) modes. The plate thickness is much smaller than its length.

Secondly, COMSOL is capable of simulating the clamping loss of a mechanical resonator geometry using a perfectly matched layer (PML). A PML is a layer of the geometry that has exact impedance matching (sound velocity in this case) with its bordering region while having a very high internal loss. This allows mechanical vibrations to enter the PML without reflection and, if the PML is of sufficient length, the vibrations will damp out before reflecting off the boundary of the finite surface. This essentially simulates the resonator's coupling to an infinite support structure while only needing to simulate a relatively small overall geometry (Fig. 22).
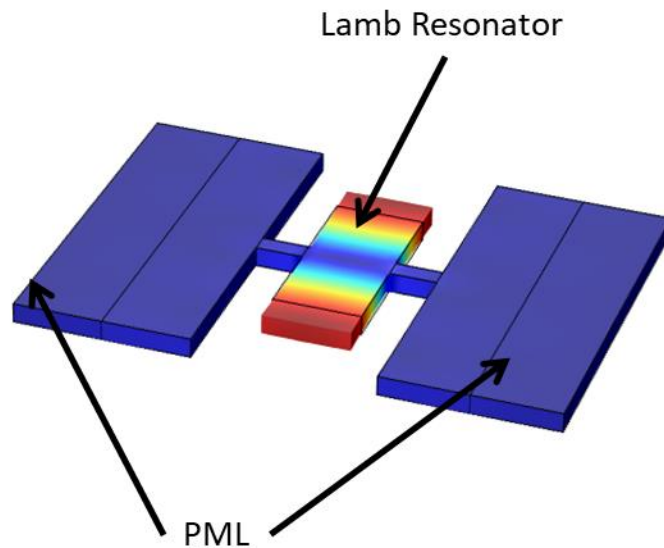
Figure 22: COMSOL simulation of Lamb wave resonator tethered to a finite support structure. The outer rectangular patterns are PMLs in which mechanical excitations decay quickly. The mode shown is the 0th order symmetric Lamb mode.

The tether dimensions are the most crucial parameters for optimizing the Q factors for the Lamb wave modes. Decreasing the tether cross-section increases the Qs monotonically since there is less coupling to the bulk diamond but also decrease the structural stability of the plate. Varying tether lengths also changes the Q factor for the symmetric modes sinusoidally (Fig. 23). This is understood by noting that the tethers themselves have flexural modes which have low displacements if the edges of the tether correspond to nodes of the mode (i.e. $\ell = n\frac{\lambda}{2}$) and will therefore increase the quality factors greatly. It can be seen that for thin tethers with optimized lengths, Q factors for the symmetric Lamb wave modes approach 10^6.
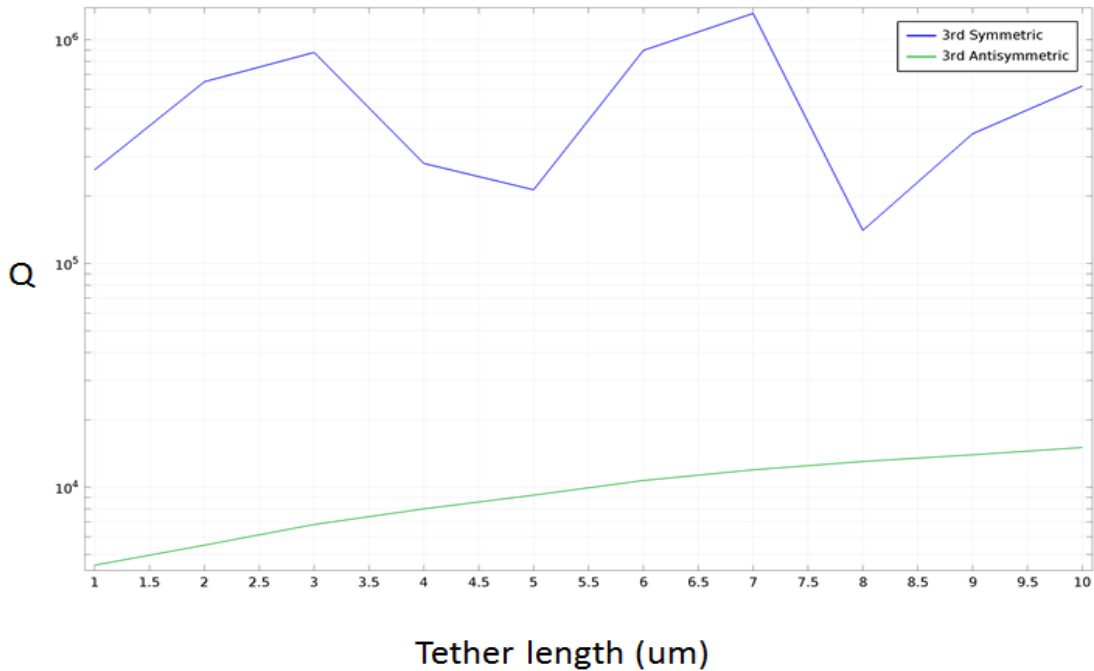
Figure 23: Quality factors as a function of tether length for higher order symmetric and anti-symmetric Lamb modes.

6.5 Phononic Crystals

Though clamping loss can be greatly reduced by using tethers/support structures of smaller dimensions, this will inevitably make the structures fragile and prone to breaking, especially in the cases of sub-micron thickness resonators. A common way of reducing clamping loss is in using a highly strained material, which has been observed to both increase the frequency and quality factor of comparable mechanical modes. This Q factor increase is generally attributed towards "dissipation dilution," where the elastic energy of the vibration is diluted by a lossless potential[63]. Though this method is viable for materials such as thin SiN membranes grown on oxide substrates, the fabrication of highly strained single crystal diamond is not at the same level of sophistication as SiN. In addition, high static strain can negatively affect the orbital selection rules of the NV center, potentially complicating experiments involving the excited state (as shown in Chapter III).

A recent and novel method for reducing clamping loss in nanomechanical resonators has been through the use of "phononic crystal shields." The general idea behind this method is to engineer the mechanical dispersion relation of the support structure such that the resonator mode of interest cannot couple to the support structure (i.e. its environment) due to no modes of that frequency existing. The general way of accomplishing this dispersion relation engineering is by creating periodically changing structures of differing acoustic velocity. In practice, this is done by etching periodic holes of certain dimensions in the support structure. An example of this is given in Figure 24 below, where both a phononic and photonic cavity are created in the same region for a 5GHz acoustic mode and 1550nm optical mode[64]. The optical mode is primarily used to

measure the in-plane compression mode of the resonator. The structure is made on a Silicon on insulator (SOI) substrate and patterned with the holes shown in Fig. 24b, which serve to create the dispersion relation shown in Fig. 24c. Multiple structures are created with varying amounts of periodic shielding and it is shown that the quality factor increase exponentially with increasing acoustic shield periods, before saturating to $Q=4.9*10^{10}$ ($N_{period}=10$) at milliKelvin temperatures.
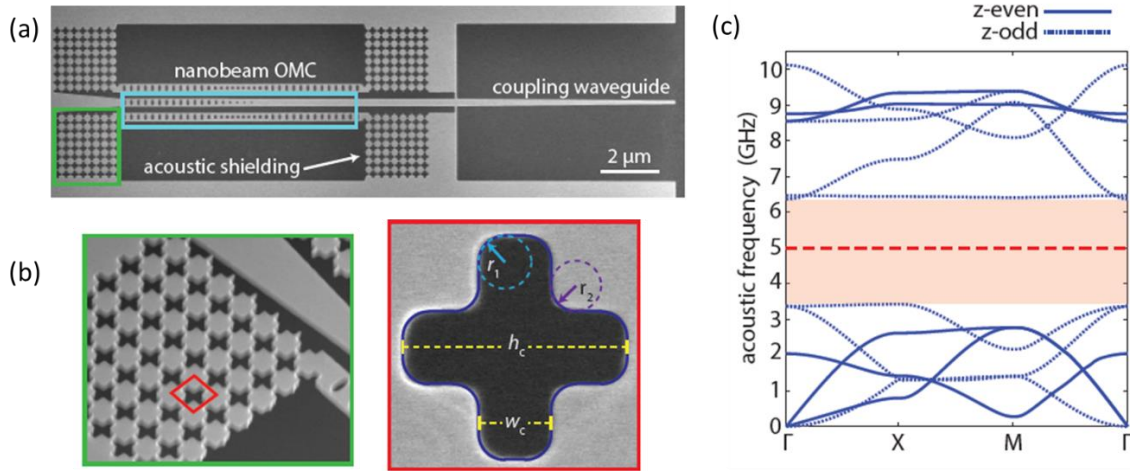
Figure 24: Phononic shield in Si resonators. (a) SEM image of SOI optomechanical resonator. (b) Left: Zoom in of acoustic shielding. Right: Zoom in of acoustic shielding pattern and relevant dimensions. (c) Phononic dispersion relation calulcation for the pattern given in (b). (Images from [64])

6.6 Summary

The two differing NV-phonon coupling schemes shown in Figure 18 impart differing requirements for the mechanical resonators to be used, though high Q is necessary for both. The phonon-assisted spin transition has sub-MHz linewidths when properly detuned, thus only requiring cantilever modes of a few MHz frequency to be sideband-

resolved. The sideband optical transition requires higher mechanical frequencies due to the high optical linewidths. As such, the Lamb wave modes in a tethered plate have been investigated as a candidate for the mechanical mode necessary. In particular, the Q factors of both the symmetric and anti-symmetric modes have been investigated, suggesting that the symmetric mode of 0th order is a suitably high Q mode. Though the Q factor of the symmetric mode can be made arbitrarily high by decreasing the dimensions of the support tether, this will make the structure vulnerable to breakage during the fabrication process. As such, phononic crystal crystals can be used to decrease the clamping loss by creating a support structure with a phonon bandgap at the frequency of the Lamb wave resonator.

CHAPTER VII

FABRICATION OF LAMB WAVE RESONATORS

This chapter is based on work co-authored by Thein Oo and Hailin Wang [27].

7.1 Introduction

In this chapter, I report the design and fabrication of diamond Lamb wave spin-mechanical resonators embedded in a two-dimensional (2D) phononic crystal lattice. The resonator features GHz in-plane mechanical compression modes, which are protected by the band gap of the phononic crystal. We have developed a membrane-in-bulk approach, fabricating the suspended 2D phononic structure directly in bulk diamond. This approach overcomes the complexities and difficulties of a number of earlier fabrication approaches[65], [66], which are either incompatible with the necessary high-temperature thermal annealing for post-release surface treatment or unsuitable for fabricating 2D structures with the required feature size. To overcome excessive spectral diffusion induced by charge fluctuations near the surface, we have used a graded soft oxygen etching process that gradually reduces the etching rate to significantly below 1 nm/minute. The graded and extremely slow etching process effectively removes defective surface layers damaged by reactive ion etching, without causing significant new damages. We show that diamond surface treatment incorporating graded soft oxygen etching can suppress spectral diffusion of NV optical transitions and reduce the optical linewidth of NV centers in resonators with a thickness below 1 mm to as narrow as 330 MHz. These resonators should enable the achievement of the resolved sideband regime for the excited-state strain coupling.

7.2 The Resonator

Figure 25a shows a schematic of the overall design of a thin rectangular diamond plate embedded in a phononic crystal square lattice with a period of 8 mm, along with the displacement pattern of the fundamental compression mode. The frequency of this mode depends primarily on the length and is essentially independent of the thickness of the plate. For the length (9.5 mm) of the diamond resonator used in Fig. 25a, the fundamental mode features a frequency of 0.95 GHz. Figure 25b plots the phononic dispersion relationship of the symmetric modes for the square lattice. The large band gap protects and isolates the relevant mechanical modes from the surrounding environment. The numerical calculations for the displacement pattern and the phononic band structure in Fig. 25 were carried out with the use of COMSOL Multiphysics software package. The diamond material parameters used in the calculations include Young's modulus $E = 1050$ GPa, Poisson ratio n=0.2, and material density $r = 3539$ kg/m^3.

7.3 Fabrication and Characterization

As illustrated in Fig. 25a, the fabrication of the 2D diamond phononic structure discussed in Section 7.2 starts with surface preparation and ion implantation of a bulk diamond film about 30 μm in thickness for the creation of NV centers near the diamond surface[67]. This is followed by electron-beam lithography (EBL), mask transfer, and reactive ion etching (RIE) of the phononic structure. The diamond film is then thinned down to below 1 μm in thickness with a shadow mask technique (see Fig. 26b), until the phononic structure is completely released. Surface layers that are damaged by the thinning process are then removed through special surface treatment processes. PLE measurements

at low temperature are carried out at various stages of the fabrication process for the characterization of the optical coherence or optical linewidth of the NV centers.
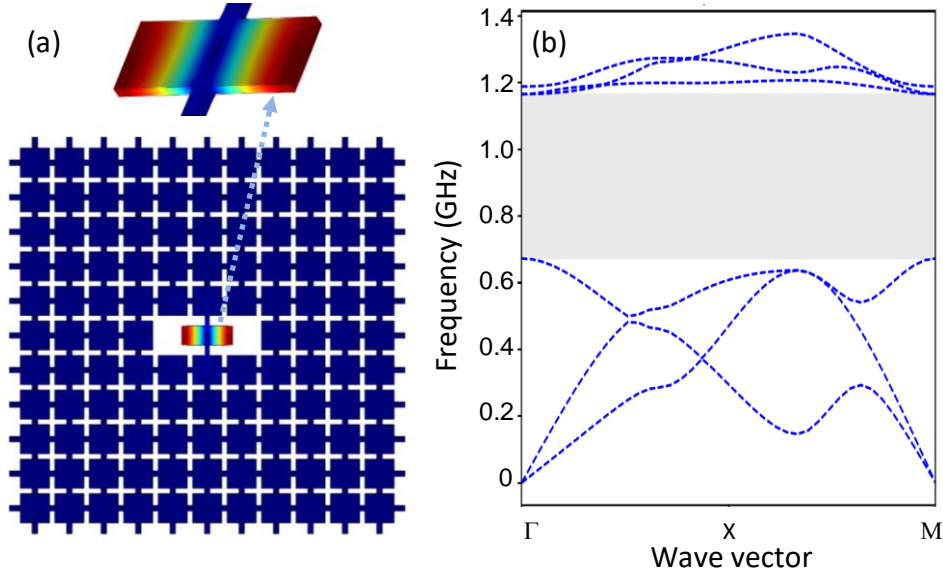
Figure 25: Design of Lamb wave resonator. (a) The design of a diamond Lamb wave resonator (4.5 μm x 9.5 μm) embedded in a square phononic crystal lattice with a spatial period of 8 μm, along with the calculated mechanical displacement pattern for the fundamental compression mode with a frequency of 0.95 GHz. The dimensions of the bridges in the square lattice are 1.25 μm x 1.25 μm. (b) Phononic band structure of the symmetric modes in the square lattice. The shaded area highlights the phononic band gap.

7.3.1 Creation of NV Centers

Electronic grade chemical-vapor-deposition (CVD) grown single-crystal diamond from Element Six, Inc. was used for the fabrication. The bulk diamond samples were sliced and polished to thin films with dimension (2, 4, 0.03) mm by Applied Diamond, Inc. Inductively-coupled-plasma (ICP) RIE was used for the removal of surface layers damaged by mechanical polishing. A 30 min Ar/Cl_2 etch was carried out in a PlasmaPro NGP80 ICP65 etcher from Oxford Instrument, Inc., with an etching rate of 80 nm/minute. This is followed by a 5 min O_2 etch in the same etcher and with an etching rate of 100 nm/minute to remove the residual chlorine in the sample. The sample was then cleaned in a triacid

74

solution with a 1:1:1 mixture of sulfuric, nitric, and perchloric acids at 380 °C for about two hours for the removal of surface contaminants. Implantation of $^{15}N^+$ ions at an energy of 85 keV and with a dosage of $3\times10^{10}/cm^2$ was carried out by Innovion, Inc. The kinetic energy used for the implantation leads to a mean nitrogen stopping depth about 100 nm with a straggle about 20 nm[68].
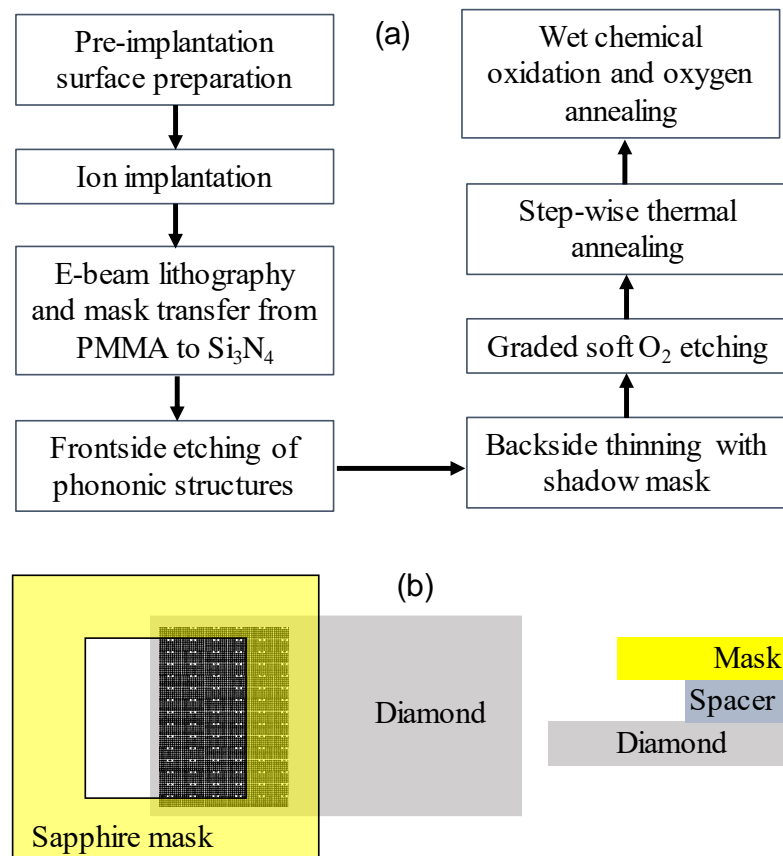
Figure 26: Fabrication steps. (a) A flowchart for the fabrication of phononic crystal mechanical resonators. (b) A sapphire slide with a square hole serves as a shadow mask for backside thinning. A spacer with a thickness of 150 mm between the diamond and the mask is used to avoid trenching.

After the implantation, we carried out step-wise thermal annealing and additional surface treatments using the procedures developed in an earlier study[68], [69]. The step-wise thermal annealing consists of a 2 hour step at 400 °C, an 8 hour step at 800 °C, and a 2 hour step at 1200 °C, with a temperature ramping rate about 3 °C per minute and with a chamber pressure below or near 10^{-6} torr. The thermal annealing was followed by wet chemical oxidation in the triacid solution for 3 hours and annealing in an O_2 atmosphere at 465 °C for 2.5 hours. The high temperature thermal annealing leads to the formation of NV centers and repairs, to a certain extent, damage in the diamond lattice induced by the implantation. The additional surface treatments aim to remove surface layers graphitized by thermal annealing and terminate the surface with O_2.

Negatively charged NV centers have a permanent electric dipole and are highly sensitive to charge fluctuations in their surrounding environment, which can lead to excessive spectral diffusion of NV optical transition frequencies and can broaden the NV zero-phonon optical linewidth to significantly greater than 1 GHz at low temperature. The zero-phonon optical linewidth or optical coherence of the NV centers can be determined with PLE spectroscopy. For the PLE measurement, we used a tunable diode laser to resonantly excite the NV center through the E_x or E_y transition and a green laser at 532 nm to initialize the NV center to the $m_s=0$ ground spin state and to reverse possible photoionization due to the resonant optical excitation.

Figure 27a shows a single PLE scan of a single NV center obtained at 8 K, after the ion implantation and the extensive surface treatment. For the single scan, the NV is initialized before the start of the scan and no green repumping is used during the scan. The total scan takes about 2 seconds and each data point takes about 40 ms. Figure 27b shows

PLE scans obtained under the same condition, but with repeated scans. The single scan features an optical linewidth near 35 MHz. The additional spectral fluctuations of the NV transition frequency shown in Fig. 27b are in part due to the repumping by the green laser beam. These results are in general agreement with the earlier experimental study[68]. With the surface preparation, ion implantation, and surface treatment procedures discussed above, the NV centers observed consistently feature an optical linewidth near 100 MHz for PLE measurements with repeated scans and with green-laser repumping. However, the experimental results become inconsistent if O_2 plasma etch significantly longer than 5 minutes is used for surface preparation before the ion implantation or if triacid cleaning is not used before the ion implantation. For example, the use of O_2 plasma etch for 30 minutes resulted in a NV PLE linewidth greater than 500 MHz. These results indicate that in order to minimize NV spectral diffusion, proper surface preparation before the implantation is as essential as the surface treatment after the implantation.
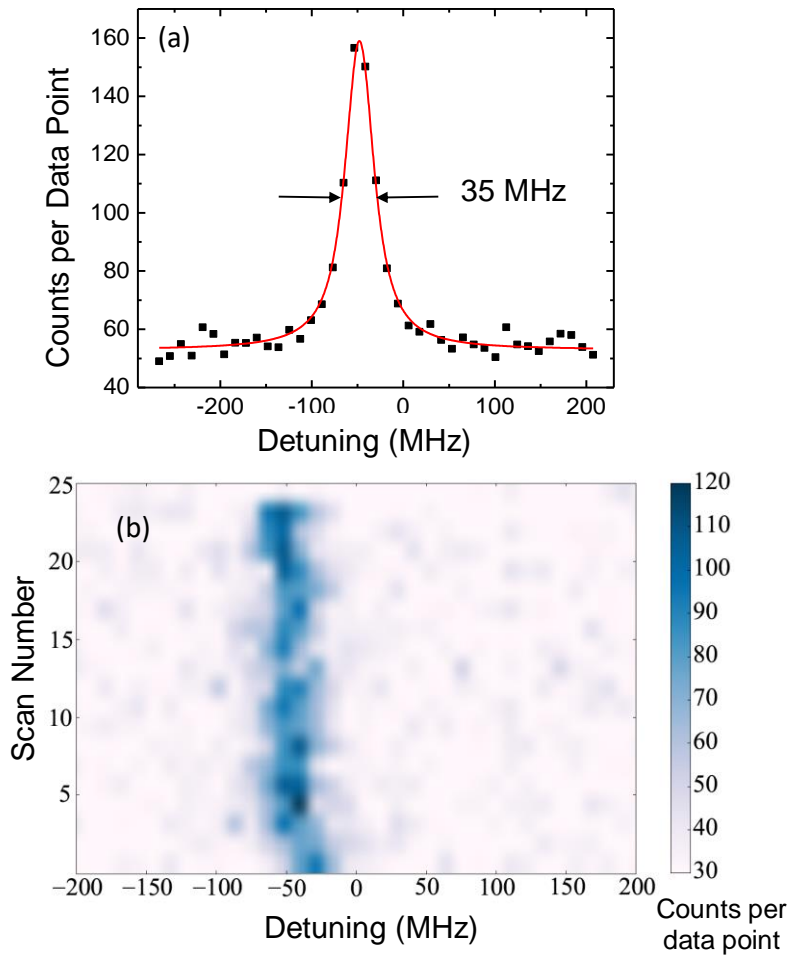
Figure 27: Spectral diffusion of the NV excited state. (a) A single PLE scan of a single NV center created by ion implantation in a bulk diamond film, followed by surface treatments. The red line is a least square fit to a Lorentzian. (b) Repeated PLE scans of the NV center. The data were obtained at 8 K. The NV center is initialized by a green laser before the start of the scan. No green repumping is used during the scan.

7.3.2 Fabrication of Suspended 2D Phononic Shield

Various approaches have been developed for the fabrication of suspended diamond 2D nano-optical and nano-mechanical structures. The diamond-on-insulator approach bonds a diamond film to a silicon wafer[70]. 2D diamond structures are released with the wet chemical etching of the SiO_2 bonding layer between the diamond and silicon. The membrane-in-frame approach mounts a bulk diamond film in a frame made of materials

such as quartz. The membrane can then be etched from the backside (the implanted side is the frontside) until the 2D structure is completely released. Another approach uses angled plasma etching or quasi-isotropic plasma etching to undercut the lithographically defined structures in bulk diamond[60], [71]. The undercutting process, however, makes it difficult to fabricate 2D structures with a relatively large feature size (e.g. > 3 µm). A membrane-in-bulk approach using an etch mask has also been used for the fabrication of membranes with a thickness of few µm[72], though trenching becomes a serious problem for membranes with a thickness less than 1 µm.

For the fabrication of suspended diamond 2D phononic structures, we have developed an approach that uses a shadow mask during the backside thinning of the bulk diamond film. In this case, a suspended diamond membrane with lithographically defined structures can be fabricated directly in a bulk diamond film, without resorting to undercutting. The membrane is attached directly to the bulk diamond, instead of being supported by a frame made of another material. For this membrane-in-bulk approach, the reuse of unsuccessful samples also becomes possible, which is highly desirable given the relatively poor fabrication yield and the high cost of electronic grade diamond samples.

2D phononic structures were fabricated in a (2, 4, 0.03) mm bulk diamond film. After the cleaning of the diamond film in boiling piranha, plasma-enhanced chemical vapor deposition (PECVD) was used for the deposition of a 280 nm layer of Si_3N_4 on the implanted (i.e. the front) side of the diamond film, on which NV centers have been created about 100 nm beneath the surface. A 10 nm layer of titanium was deposited on the Si_3N_4 layer to avoid charging during EBL. A 500 nm layer of Polymethyl methacrylate (PMMA) was then spun onto the sample, followed by EBL that defines the pattern for the 2D

79

phononic structure. Following the photoresist development, CHF$_3$ plasma RIE was used to transfer the pattern to the Si$_3$N$_4$ layer. The 2D phononic structure pattern was then fabricated onto the diamond film with the O$_2$ ICP-RIE and with the Si$_3$N$_4$ layer as a hard mask. The etching depth is 1.2 μm, with an estimated etching rate of 100 nm/minute. The etching parameters used include a RF power of 60 W, an ICP power of 420 W, a DC bias of 108 V, a chamber pressure of 10 mTorr, and an O$_2$ flow of 30 sccm. Figure 28a shows an optical image of the 2D phononic structure (the design is shown in Fig. 25a) etched in a bulk diamond film.

The key step in our membrane-in-bulk approach is the use of a U-shaped shadow mask, which is laser-cut from a sapphire slide with a thickness of 150 mm (see Fig. 26b), during the backside thinning of the diamond film. The shadow mask defines the area of the diamond film that will be thinned down and avoids trenching that occurs when the mask is in direct contact with the sample. Note that an etch mask with an angled sidewall has also been used in an earlier work to avoid trenching[73]. We positioned the U-shaped sapphire mask with a 150 μm thick spacer at one edge of the diamond film, with an etching area approximately 1.5 mm by 0.75 mm. In this way, the suspended phononic structure is attached or anchored to the bulk diamond film in three sides. If any step of the thinning or post-release surface treatment did not go as expected, the remaining bulk diamond film can still be reused.
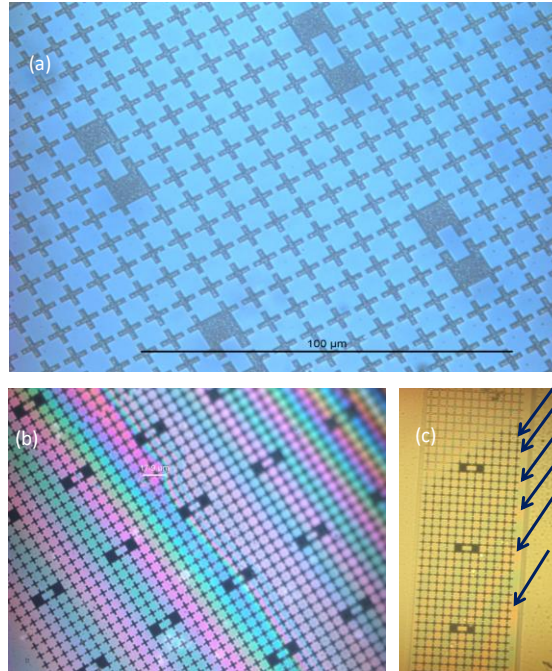
Figure 28: Optical images of fabricated structures. (a) Optical image of a 2D phononic structure fabricated in a diamond film with a thickness about 30 μm, for which the structure is not yet released. (b) Optical image of a 2D phononic structure, for which the structure is completely released. (c) Optical image of a 2D phononic structure that contains both released and unreleased regions. The arrows mark the positions of the color fringes. The three images were taken with three different samples. The period of the phononic crystals in all three images is 8 μm.

The diamond film was thinned from the backside with an alternating etch process that consists of 30 minutes of Ar/Cl$_2$ plasma etching, with an etching rate 80 nm/minute, and 2 minutes of O$_2$ plasma etching, with an etching rate 100 nm/minute, followed by 10 minutes of soft O$_2$ plasma etching, with an etching rate 6 nm/minute. The parameters for the Ar/Cl$_2$ plasma etching include a RF power of 210 W, an ICP power of 280 W, a DC bias of 310 V, a chamber pressure of 5 mTorr, 16 sccm Cl$_2$, and 10 sccm Ar. The parameters for the O$_2$ plasma etching are identical to those used for the front side. For the soft O$_2$ plasma etching, the DC bias is set to zero and the RF power is turned off. Other parameters include an ICP power of 500 W, a chamber pressure of 10 mTorr, and an O$_2$

flow of 30 sccm. We ran the thinning process continuously until the phononic structure is released or suspended. This is followed by a long period of soft O_2 plasma etching with a gradually decreasing etching rate, as will be discussed in more detail later. We used this graded soft O_2 etch to remove the surface layers damaged by the Ar/Cl_2 plasma and the hard O_2 plasma etching.

Figure 28b shows an optical image of a suspended 2D phononic structure. The bright color fringes are due to slight variations in the thickness of the suspended structure. These variations, which occurred during the slicing and polishing of the bulk diamond film, can be minimized or corrected[70]. The optical interference fringes can be used for the measurement of the membrane thickness. For the 2D phononic structure shown in Fig. 28c, a dividing line between the released and unreleased regions can be clearly identified. This line corresponds to a membrane thickness of 1.2 μm. Nearly parallel color fringes, marked by the arrows in Fig. 28c, can also be discerned. As expected, the fringe visibility increases with decreasing membrane thickness. Each interference fringe or period corresponds to a thickness change of approximately 110 nm. We can thus determine the thickness of a given nanomechanical resonator by counting the number of interference fringes.
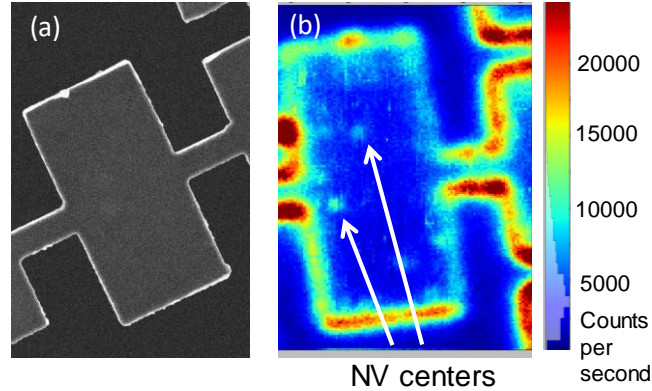
Figure 29: SEM and confocal images of Lamb resonator. (a) A SEM image of a released nanomechanical resonator. The dimension of the resonator is 9.5 μm by 4.5 μm. (b) Confocal optical image showing NV centers in a released nanomechanical resonator.

Figure 29a shows a scanning electron microscope (SEM) image of a released nanomechanical resonator. A confocal optical image of a released nanomechanical resonator showing NV centers in the resonator is also displayed in Fig. 29b. Note that the relatively large-scale edge roughness shown in Fig. 29a is due to an intentional under-etching for the mask transfer from PMMA to Si_3N_4, which ensures a relatively thick Si_3N_4 layer to protect the NVs from the O_2 plasma during the frontside etching. This roughness can be avoided with a more precise mask transfer.

7.3.3 Post Release Surface Treatment

A major technical hurdle that has thus far hindered the use of NV centers in spin-mechanical resonators as well as optical microcavities is the severe degradation of optical properties of NV centers in a thin diamond membrane. While an optical linewidth near 100 MHz has been observed for NV centers in diamond membranes as thin as 3 μm[40], previous studies have shown an optical linewidth of 1 GHz or greater for NV centers in

membranes with a thickness ranging from 1 μm to 100 nm[74], [75]. Similar results have also been observed in our samples, which were fabricated with the procedures discussed above, but without the graded soft O_2 etching step. The samples then underwent the same surface treatments as those used after the ion implantation. For these experiments, fluorescence from individual NV centers in a nanomechanical resonator is detected in a confocal optical setup. These NV centers, which feature permanent electric dipoles, are highly sensitive to charge fluctuations on the back surface of the membrane, even when the back surface is far (e.g., 1 μm) away from the NV centers. For the two samples we have investigated, for which the graded soft O_2 etch is not used, we have found no NV centers with a PLE linewidth smaller than 1 GHz when the resonator thickness is less than 1 μm, in agreement with the extensive earlier studies. In this case, excessive charge fluctuations in the surface layers damaged by the long etching process lead to strong NV spectral diffusions and thus large optical linewidths. These damages cannot be repaired completely with surface treatment processes such as those used after the ion implantation. Figure 30a shows an example of the PLE spectrum of a NV center obtained in a released nanomechanical resonator with a thickness near 1 μm.

In comparison, for the etching of the 2D phononic structure on the frontside, the Si_3N_4 hard mask protects the front surface from damages induced by the O_2 plasma. Figure 30b shows a PLE spectrum of a typical NV center in a nanomechanical resonator obtained before the backside etching process. For the average of repeated scans, an optical linewidth of 115 MHz is obtained, which indicates that because of the hard mask, the frontside etching process induces minimal damages on the diamond surface. Note that surface

treatments including wet chemical oxidation and oxygen annealing were carried out before the optical characterization.
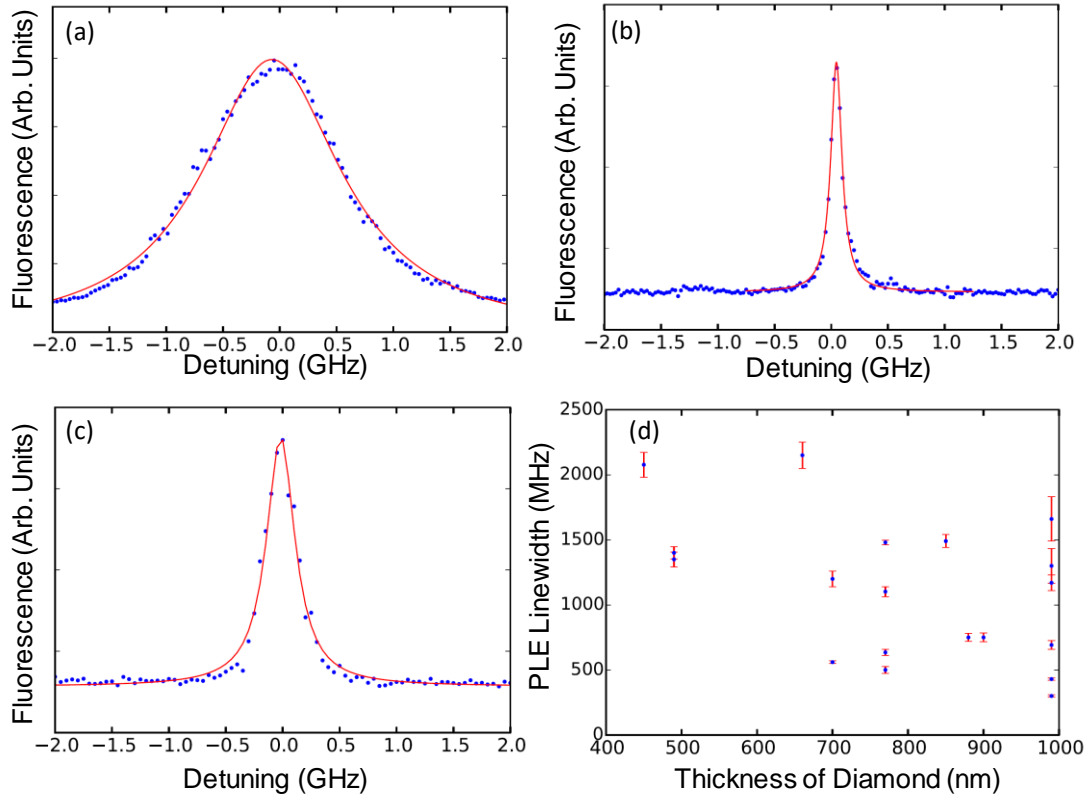
Figure 30: Optical characterization of NV centers. (a) PLE spectrum of a NV center in a released nanomechanical resonator with a thickness near 1 μm and without soft O_2 etch. (b) PLE spectrum of a NV center in a nanomechanical resonator before the backside etching process. (c) PLE spectrum of a NV center in a released nanomechanical resonator with a thickness slightly below 1 mm and with soft O_2 etch. Red lines are least square fits to a Lorentzian, showing a linewidth of 1.5 GHz for (a), 115 MHz for (b), and 330 MHz for (c). All PLE spectra are averages of repeated scans, for which green repumping is used at each data point during the scan. (d) A scatter plot of the PLE linewidth for NV centers in the released phononic structures with varying thicknesses, obtained under conditions similar to those in (c). All data were obtained at 10 K.

The technical challenge for the surface treatment after the long reactive ion etching process is to remove the damaged surface layers without causing additional damages. Since

85

wet chemical oxidation is not effective in removing the defective surface layers, we have developed a graded soft O_2 etching process, which decreases the etching rate gradually from 6 nm/minute to significantly below 1 nm/minute as the etching progresses. The graded soft O_2 etch consists of four steps, a 1 hour etch with an ICP power of 500 W and an etching rate of 6 nm/minute, a 2 hour etch with an ICP power of 200 W and an etching rate of 1 nm/minute, a 10 minute etch with an ICP power of 150 W, and a 10 minute etch with an ICP power of 100 W. This long and graded soft O_2 etching process aims to remove the damaged surface layers, while avoiding additional damages through the gradual decrease in the etching rate[76]. The soft O_2 etch is followed by the step-wise thermal annealing, triacid wet chemical oxidation, and oxygen annealing, which are essentially the same as those used after the ion implantation discussed above[68]. After these extensive surface treatments, we have been able to obtain NV linewidth as small as 330 MHz in a diamond nanomechanical resonator with a thickness below 1 μm, as shown in Fig. 30c. Figure 30d shows a scatter plot of the PLE linewidths (obtained from averages of repeated scans) vs diamond thickness for NV centers measured in released phononic structures. Although a large fraction of the NV centers (>50%) in the released structures still exhibit an optical linewidth near or exceeding 1 GHz, these experiments demonstrate that suitable surface treatments can effectively repair the surface damages induced by the reactive etching process. In principle, the duration and gradual step down of the etching rate for the soft O_2 etch can be adjusted and optimized to achieve consistent narrow optical linewidth for NV centers in diamond membranes with a thickness less than 1 μm.

7.3.4 Additional Discussion

We have discussed the optical characterization of NV centers at four different stages of the fabrication process: i) after the implantation, ii) after the frontside etching of the phononic structure, iii) after the backside thinning but before the soft O_2 etch, iv) after the soft O_2 etch. Surface treatments, including step-wise thermal annealing up to 1200 °C, wet chemical oxidation, and oxygen annealing, have to be carried out before the optical characterization at each of these stages, except that the step-wise thermal annealing is not needed for the optical characterization after the frontside etching of the phononic nanostructures. To increase the yield of and to speed up the fabrication process, we only carry out the surface treatments and thus optical characterization in the last step of a typical fabrication run.

Compared with the various fabrication approaches developed in earlier studies, the membrane-in-bulk approach is straightforward to implement. There are no additional steps of mounting a diamond film to a frame or bonding a diamond film to a silicon wafer. The membrane-in-bulk approach also allows convenient and direct accesses to both surfaces of the membrane. Furthermore, the SiO_2 bonding used in the diamond-on-insulator and the membrane-in-frame approach is not compatible with high-temperature (~ 1200 °C) thermal annealing, which we found is essential for the post-release surface treatment even with the graded soft O_2 etch.

A recent experimental study has shown that NV centers formed from implanted nitrogen exhibit poor optical coherence, with optical linewidth exceeding 1 GHz[77]. Most of the implanted NV centers in the bulk diamond sample we have studied feature a narrow optical linewidth (100 to 200 MHz with green repumping at each data point). Additional

87

studies indicate that these NV centers with narrow optical linewidth are formed with native ^{14}N, instead of the implanted ^{15}N, in agreement with the earlier study[77].

It should be noted that out-of-plane mechanical vibrations in commonly used nanomechanical resonators can be conveniently probed with optical interferometric techniques. The interferometric techniques, however, are not sensitive enough for high-frequency in-plane mechanical vibrations, such as the compressional modes in a Lamb wave resonator, because the in-plane mechanical motion induces primarily amplitude, instead of phase, changes in these measurements. The in-plane mechanical vibrations can be probed directly through the spin-mechanical coupling, or through near-field optomechanical coupling with whispering gallery mode (WGM) optical resonators. The near-field optomechanical coupling has been used extensively in cavity optomechanics and can be applied to both out-of-plane and in-plane mechanical vibrations[78], [79].

A special feature of the phononic crystal mechanical resonator developed in this work is that the resonator can be largely immune to considerable imperfections of the fabricated process as long as the mechanical resonance is in the band gap of the surrounding phononic crystal lattice, because mechanical waves cannot be scattered into vacuum. For the 2D square lattice shown in Fig. 25a, the band gap shown in Fig. 25b is insensitive to relatively small thickness variations. Furthermore, the frequency of the fundamental compression mode in our mechanical resonator is determined by the length of the thin plate and is independent of the thickness of the plate, as confirmed by numerical calculations. In comparison, for optomechanical crystals, the fabrication imperfections including the variation in the thickness strongly affects both the frequency and damping rate of the optical cavity modes.

7.4 Summary

In conclusion, we have successfully developed and fabricated Lamb wave spin-mechanical resonators that feature a GHz fundamental compression mode and NV centers with optical linewidths as narrow as 330 MHz. The mechanical resonators are embedded in a phononic crystal square lattice with a phononic band gap that protects the relevant compression modes. This type of diamond spin-mechanical resonators has been used in an earlier theoretical study on mechanically mediated spin entanglement and state transfer, which has discussed in detail spin-mechanical coupling via orbital degrees of freedom of the NV excited states through an optical Raman transition[80] . The membrane-in-bulk approach developed for the fabrication of the suspended 2D phononic structures, which is relatively easy to implement and allows high-temperature thermal annealing required for post-release surface treatment, can also be extended to the fabrication of diamond 2D photonic structures. A graded soft O_2 etching process with the etching rate reduced gradually to significantly below 1 nm/minute has been employed for the removal of surface layers damaged by reactive ion etching without causing significant new damages. Combining the graded soft O_2 etch with other established surface treatment techniques can lead to much improved spectral stability of NV optical emissions in diamond membranes with a thickness less than 1 mm. Overall, these advances should enable a new experimental platform for exploiting both spin and mechanical degrees of freedom for quantum information processing, including the use of GHz mechanical compression modes in phononic networks of solid state spins[80].

CHAPTER VIII

SUMMARY

8.1 Transduction with Solid State Defects

Hybrid quantum systems are systems which can exploit the advantageous properties of separate physical systems, such as the fast gate time of SC qubits or the long storage time of solid state spins. The importance of hybrid quantum systems is twofold. Firstly, they may solve certain scaling issues which would otherwise limit the creation of large scale quantum computer via the quantum node/quantum channel architecture shown in Figure 1c. Secondly, they may be critical for interfacing quantum systems which are very far apart and do not operate using fields which can be transmitted far without high loss (ex. MW fields for SC qubits).

In order to realize a hybrid quantum system, coherent transduction between the control fields/mechanisms for the two disparate systems is needed. For this transduction the NV center is particularly well suited. The NV is a thoroughly researched solid state defect which can couple to a variety of phenomena including optical, MW, magnetic and strain fields.

8.2 Phase Transfer Between MW and Optical Fields

The NV center energy level structure allows for the coupling of a spin superposition using both MW and optical fields. The dark state, a special superposition state of a three level system being pumped by two fields, is decoupled from excitations to the common excited state. MW fields were used to prepare this superposition, whose phase was

determined by the relative phase difference between the two MW fields. Two optical fields then resonantly pumped each spin state in the superposition to a common excited state. The phase difference of the optical fields and MW fields determined if the superposition state was in the dark state or bright state, resulting in a phase dependent intensity for the fluorescence. An analogous preparation and readout sequence is done for the case of optical preparation and MW readout. These experiments demonstrate a coherent coupling between EM fields of disparate energy levels and are the first step towards coherent state transfer (not just phase readout) between MW and optical fields.

8.3 Phonon Coupling to NV Centers

Phonons have certain advantages over photons, such as their slower speed and easier confinement, which has motivated research towards integrating them into hybrid quantum systems. In particular, the wide variety of physical systems that intrinsically couple to them has led to interest in phonons as both a control mechanism for qubits and a channel which coherently transmits quantum information. The NV center being a solid state defect couples to strain in the crystal lattice and numerous experiment have shown phonon-assisted control of the states of the NV center.

Most work done up to this point with the NV center has focused on strongly driving mechanical vibrations into the diamond externally. However, the regime of single-phonon coupling will be critical since the number of phonons involved in most quantum related applications will likely be small. This means that high quality factor resonators will be critical for enhancing the single-phonon interaction strength with the NV center. An OMIT-like interference experiment, with one of the exciting fields being phonon-assisted, was

suggested as a way to measure the strength of the phonon coupling. Two different phonon assisted "two-level" schemes were presented which utilize different energy levels in the NV center and place different requirements for the mechanical resonator.

8.4 Fabrication of Mechanical Resonators with Optically Coherent NVs

The design and fabrication of high quality factor mechanical resonators in diamond posed a number of challenges. Firstly, the requirements for a resonator with mechanical frequency near 1GHz prevented the use of more traditional cantilever designs. Lamb waves were investigated as promising modes which possessed reasonably high Q factors for appropriately chosen geometries. Resonator geometries containing these modes were simulated in finite element analysis software (COMSOL). To ensure clamping loss was minimal, a phononic crystal shield was designed in the support structure of these resonators possessing a phononic bandgap at the frequency of the mode of interest.

Regarding fabrication, the chemical inertness and lack of thin film single crystal diamond means that the main way of creating sub-micron diamond membranes is via plasma etching of a thicker starting structure. This method creates damaged diamond layers which host paramagnetic and charge defects, which severely degrade the optical and spin coherence of NVs near these sources of noise. The methods used in fabricated our structures mitigated this damage. A Lamb wave resonator imbedded in a phononic crystal shield was created using electron beam lithography processes. The process which thinned down the structure to sub-micron thicknesses utilized a soft O_2 plasma etch with a gradually decreasing ICP power. Using this process, NV linewidths narrower than 1GHz were observed in diamond membranes as thin as 600nm.

8.5 Future Work

Progress has been made towards integrating NV centers in high quality factor mechanical resonators without a significant loss in optical coherence. However, due to the nature of the mechanical modes chosen, interferometric measurements of the modes are difficult, since most of the displacement is in the plane of the diamond (as opposed to out-off-plane for the fundamental cantilever mode). As such, the mechanical properties of the fabricated structures are still unknown.

In addition, the NV linewidths in thin diamond are still inconsistent. There are two ways of proceeding with the Lamb wave experiment. The first way is to improve the graded soft O_2 etch used in removing the plasma damage in the lattice. Though there are limits in how close one can bring the NV center to the diamond surface before its coherence properties degrade [81]–[83], the current implantation depth of the NVs (~100nm) is nowhere near that. Therefore, it is reasonable to conclude that the bulk-like optical linewidths of NV centers implanted 100nm below the surface should be physically realizable in diamond membranes as thin as 200nm (if not thinner).

A more promising way forward in the case of the Lamb wave resonator is to use a defect center with optical properties which are more robust to charge noise. In particular, the silicon vacancy (SiV) center in diamond is a defect center with no permanent dipole moment due to its symmetric configuration in the diamond lattice. This property allows the SiV center to maintain its original linewidths in diamond membranes as thin as 200nm with the equivalent plasma etching steps done on the NV center. The properties of this defect center in thin diamond membranes have been investigated in the Appendix.

93

APPENDIX

THE SILICON VACANCY CENTER IN DIAMOND

This chapter contains material from [28] which was co-authored with Hailin Wang.

A.1 Introduction

We report the fabrication and optical characterization of thin diamond membranes implanted with negatively charged silicon vacancy (SiV^-) centers. The variations in the membrane thickness enable the experimental study of optical coherence of SiV^- centers as the membrane thickness is varied from 100 nm to 1100 nm. Photoluminescence excitation spectroscopy at low temperature shows that most of the SiV^- centers in these membranes feature an optical linewidth ranging between 200 and 300 MHz. Furthermore, there is no discernable dependence of the optical linewidth on the membrane thickness for membranes as thin as 100 nm, indicating the feasibility of incorporating SiV^- centers in a varity of diamond nanostructures and still maintaining the excellent optical coherence of these color centers.

In comparison with NV centers, negatively charged silicon vacancy (SiV^-) centers in diamond exhibit superior optical properties[84], [85]. The zero-phonon line of SiV^- centers contains more than 70% of the total fluorescence. Because of their inversion symmetry, SiV^- centers are robust against charge fluctuations in their surrounding environment. Two-photon quantum interference from separated SiV^- centers have been demonstrated[86]. SiV^- centers created with ion implantation and annealing can exhibit nearly lifetime-limited optical linewidth[87]. SiV^- centers have been incorporated in

94

diamond one-dimensional (1D) photonic crystal structures as well as whispering gallery mode (WGM) optical resonators for cavity QED studies[88]. Although spin decoherence time of SiV⁻ centers is relatively short at elevated temperatures, spin decoherence time as long as 13 ms has been observed at temperatures near 100 mK[89]. In addition, recent development of neutral SiV centers indicates that the neutral SiV centers can exhibit robust spin coherence even at room temperature[90]. SiV-based systems can thus provide a highly promising platform for developing optical quantum networks.

An important issue that has not been adequately addressed is to what extent optical coherence of SiV⁻ centers is degraded by the etching process, which is necessary for the fabrication of diamond nanophotonic structures. Optical linewidths near 300 MHz have been reported for SiV⁻ centers in 1D photonic crystal structures that feature a lattice constant of 260 nm and a triangular cross section with a side dimension of order 500 nm[88]. Similar linewidths have also been observed in diamond nanocrystals and nanopillars with a dimension of order 200 nm[91]. For the incorporation of SiV⁻ centers in diamond nanostructures including both photonic and phononic nanostructures, it is important to know whether excellent optical coherence can be maintained in nanostructures with even smaller feature sizes.

In this appendix, we report studies of the optical coherence of implanted SiV⁻ centers in diamond membranes as thin as 100 nm. Variations in the thickness of the membranes fabricated from a 30 μm thick diamond film have enabled us to measure the optical linewidth of SiV⁻ centers as the membrane thickness is decreased from 1100 nm to 100 nm. We show that most of the SiV⁻ centers in these membranes feature optical

linewidths ranging between 200 and 300 MHz. Remarkably, there is no discernable dependence of the optical linewidth on the membrane thickness. These results indicate the feasibility of incorporating SiV⁻ centers in a wide variety of diamond nanostructures and still maintaining the excellent optical coherence of the SiV⁻ centers.

A.2 Membrane Fabrication

We have fabricated diamond membranes that were designed for use in our cavity QED systems. In these systems, color centers in a thin diamond membrane couple evanescently to optical WGMs of a silica resonator[92]. The fabrication started with electronic grade single-crystal diamond films, with the slicing and polishing of a chemical-vapor-deposition grown bulk diamond sample (Element Six, Inc.) into the thin films (with a dimension of (2, 4, 0.03) mm) carried out by Applied Diamond, Inc. Figure 31(a) shows schematically the steps of the membrane fabrication. The ion implantation and high temperature thermal annealing used in the fabrication follows essentially those developed in an earlier study[87].
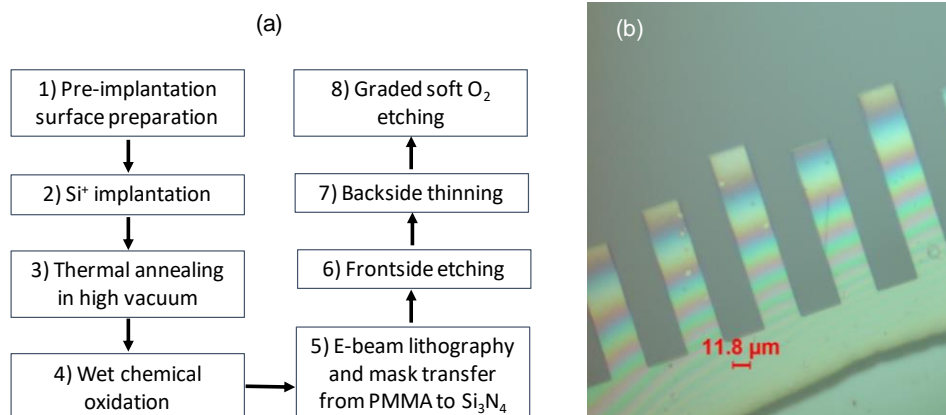

Figure 31: Design of diamond membranes with SiV centers. (a) A flowchart of the steps used for the fabrication of diamond membrane stripes. (b) An optical image of a diamond sample showing completely released membrane stripes. The color fringes reflect the thickness variation of the membranes.

The first step is to remove mechanical-polishing induced surface damages and prepare the diamond film for ion implantation. For this step, we used Ar/Cl_2 plasma etching to remove about 2 to 3 μm diamond surface layers. The inductively-coupled-plasma (ICP) reactive ion etching (RIE) was carried out in a PlasmaPro NGP80 ICP65 etcher from Oxford Instrument, Inc., with an etching rate of 80 nm/minute. For the removal of the residual chlorine ions in the diamond film, the Ar/Cl_2 plasma etching was followed by a 5 minute O_2 plasma etching, with an etching rate of 100 nm/minute. The diamond film was then placed in a triacid solution with a 1:1:1 mixture of sulfuric, nitric, and perchloric acids at 380 °C for about two hours for the removal of surface contaminants.

For the second step, $^{29}Si^+$ ions with a kinetic energy of 150 keV and with a dosage of $1x10^{10}/cm^2$ were implanted near the surface of the diamond thin film. The implantation was carried out by Innovion, Inc. The kinetic energy used for the implantation leads to a mean silicon stopping depth about 100 nm with a straggle about 20 nm[87].

The third step is high-temperature thermal annealing in high vacuum ($< 10^{-6}$ Torr). The thermal annealing process consists of 2 hours at 400 °C, 8 hours at 800 °C, and 2 hours at 1200 °C. The temperature ramping rate is approximately 3 °C per minute. The fourth step is the wet chemical oxidation in the triacid solution discussed above for 3 hours. The thermal annealing assists the formation of SiV^- centers and repairs implantation-induced damages in the crystal lattice, as shown in the earlier study[87]. The wet chemical oxidation removes surface layers graphitized by the thermal annealing.

97

The fifth step patterned a Si_3N_4 mask on the front (i.e. the implanted) side of the diamond film. Though simple stripes of diamond membranes are used in our cavity QED systems, the same process can also be used for the fabrication of two dimensional (2D) photonic or phononic nanostructures. In this step, a 280 nm layer of Si_3N_4 was deposited on the front side of the diamond film with plasma-enhanced chemical vapor deposition (PECVD). This is followed by the deposition of a 10 nm layer of titanium to avoid charging during electron beam lithography (EBL). We then spun a 500 nm layer of Polymethyl methacrylate (PMMA) on the front side of the diamond film and carried out EBL and photoresist development to define a simple stripe pattern. This pattern was transferred from the PMMA layer to the Si_3N_4 layer with CHF_3 plasma etching.

The sixth step etched the stripe pattern onto the front side of the diamond film. O_2 plasma etching was used, with an estimated etching rate of 100 nm/minute and with the Si_3N_4 layer as a hard mask. The etching parameters include a RF power of 60 W, an ICP power of 420 W, a DC bias of 108 V, a chamber pressure of 10 mTorr, and an O_2 flow of 30 sccm. The etching depth is slightly over 1 mm.

The seventh step thinned the backside of the diamond film until the stripe pattern is completely released. For this step, we used an alternating process that consists of 30 minutes of Ar/Cl_2 plasma etching, with an etching rate about 80 nm/minute, and 2 minutes of O_2 plasma etching, with an etching rate about 100 nm/minute, followed by 10 minutes of soft O_2 plasma etching, for which the DC bias is set to zero and the RF power is turned off. The Ar/Cl_2 plasma etching used a RF power of 210 W, an ICP power of 280 W, a DC bias of 310 V, a chamber pressure of 5 mTorr, 16 sccm Cl_2, and 10 sccm Ar. The O_2

plasma etching used the same parameters as those for the front side etching. The soft O_2 plasma etching used an ICP power of 500 W, a chamber pressure of 10 mTorr, and an O_2 flow of 30 sccm, with an estimated etching rate of 6 nm/minute. A sapphire shadow mask was also used for the backside thinning such that only a small portion (< 10 %) of the diamond film was etched. In this case, the membrane stripes are attached to and supported by the much thicker film. In addition, the remaining film can also be reused.

The eighth step in our fabrication process is the use of graded soft O_2 plasma etching to remove surface layers damaged by the harsh ICP-RIE process. For the graded soft etching process, the etching rate decreases gradually from 6 nm/minute to below 1 nm/minute, with the aim of removing the damaged surface layers without causing significant new damages[76]. The graded soft O_2 etching process consists of 1 hour with an ICP power of 500 W and an etching rate of 6 nm/minute, 2 hours with an ICP power of 200 W and an etching rate of 1 nm/minute, 10 minutes with an ICP power of 150 W, and 10 minutes with an ICP power of 100 W.

The patterning and etching of the membrane stripes (i.e. steps 5 to 8 discussed above) are essentially the same as those used for diamond nanostructures that are intended for studies of NV centers in Chapter VII. The main difference in the fabrication process is the surface treatment used after graded soft etching. While high temperature thermal annealing and wet chemical oxidation following the graded soft etching are used in both cases, oxygen annealing was not used as the surface termination step for SiV⁻-based diamond membrane stripes.

Figure 31(b) shows an optical image of membrane stripes in a fabricated diamond sample. The membrane width is 20 μm and the length varies from 80 to over 100 μm. The variations in the thickness of the original diamond film lead to corresponding variations in the membrane thickness. The pronounced color fringes exhibited by the membrane stripes shown in Fig. 31b arise from optical interference. Each set of fringes corresponds to a thickness variation of approximately 110 nm[70]. The first fringe measured from the tip corresponds to a membrane thickness approximately 110 nm, as verified by additional measurements using an optical profilometer (Zygo NewView 7300). Note that the thickness variation of the 30 μm film, which originates from dicing and polishing, can be minimized via an additional carefully-designed polishing process, as shown in an earlier experimental study[70]. The variations in the membrane thickness, however, make it convenient to investigate the dependence of the optical coherence of SiV⁻ centers on the membrane thickness.

A.3 Optical Coherence and Discussions

Negatively-charged SiV⁻ centers feature optical transitions with wavelengths near 737 nm. In the absence of an external magnetic field, both the ground and excited states are doublets due to spin-orbit interactions, as shown schematically in Fig. 32(a). The spin-orbit splittings for the ground and excited states are λ_{so}^g=47 GHz and λ_{so}^u =260 GHz, respectively. All transitions between the ground and excited states are dipole-allowed. The excited-state lifetime is 1.7 ns, corresponding to a lifetime limited optical linewidth of 94 MHz (full width at half maximum). An earlier experimental study on SiV⁻ centers implanted in bulk diamond samples has shown that most of the SiV⁻ centers feature an

optical linewidth ranging from 200 MHz to 400 MHz[70]. A relatively small inhomogeneous linewidth (a few GHz) for SiV⁻ centers has also been observed[84].
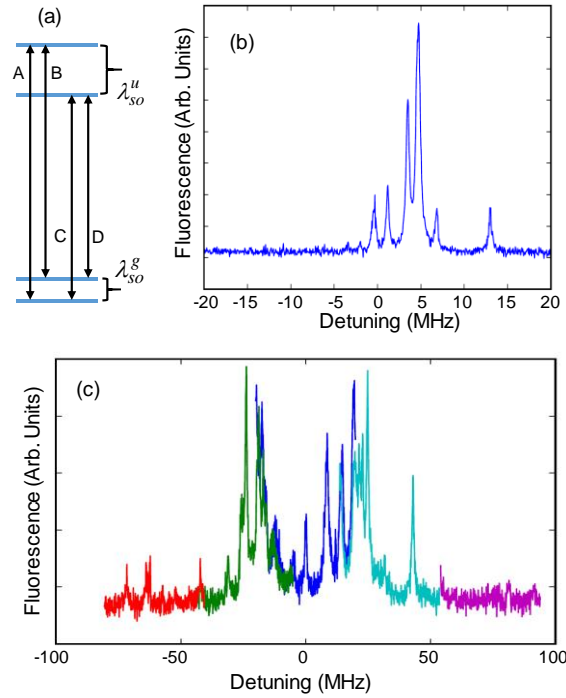
Figure 32: Energy levels of the SiV center. (a) Schematic of the optical transitions in a SiV⁻ center (with no strain). (b) A PLE spectrum obtained near the SiV⁻ optical transition wavelengths. (c) An extended scan of a PLE spectrum, combining together five individual scans. All data were obtained at a temperature of 12K.

To characterize the optical coherence of SiV⁻ centers in the diamond membranes, we have carried out photoluminescence excitation (PLE) measurements using membranes with a thickness ranging from 100 nm to over 1000 nm. The diamond sample was mounted on the cold finger of a close-cycled helium cryostat (CR-111 Cryostation from Montana Instruments). The PLE experiments were carried out with a home-built confocal optical microscope setup, which uses a 100x objective with a numerical aperture, NA=0.85 outside the cryostat. For the PLE experiments, the SiV⁻ centers were resonantly excited with a

tunable diode laser (New Focus Velocity TLB-6712). A relatively low laser power (< 1 mW) was used to avoid power broadening of the optical transitions. A dichroic beam splitter at 760 nm was used in the collection/excitation path of the fluorescence to reject the reflected and scattered laser light. A tunable long-pass optical filter with a cut-off near the laser wavelength was also used for additional rejection. The fluorescence from the SiV⁻ centers was detected with an avalanche single-photon counting module (Excelitas SPCM-AQRH-16-FC). PLE spectra shown in Fig. 32 are single scans with data averaging at each spectral position. A 532 nm laser irradiation was used at each data acquisition to initialize and stabilize the SiV⁻ centers in the negative charge state, with the detector gated off during the green laser pulse.

Figure 32(b) shows as an example a PLE spectrum obtained in a bulk single crystal diamond and at a temperature of 12 K. Multiple SiV⁻ centers are observed within the effective detection area of our confocal setup, indicating the relatively high density of SiV⁻ centers created in the sample. Figure 32(c) shows a PLE spectrum in the bulk crystal with a spectral range about 175 GHz. For this spectrum, we stitched or combined together five PLE spectra of individual scans with a scan range of 40 GHz. From the extended PLE spectrum, we can obtain a ground-state splitting of approximately 48 GHz, in general agreement with the theoretical expectation. Note that the PLE resonances shown in Fig. 32(b) correspond to the C-transition in Fig. 32(a).
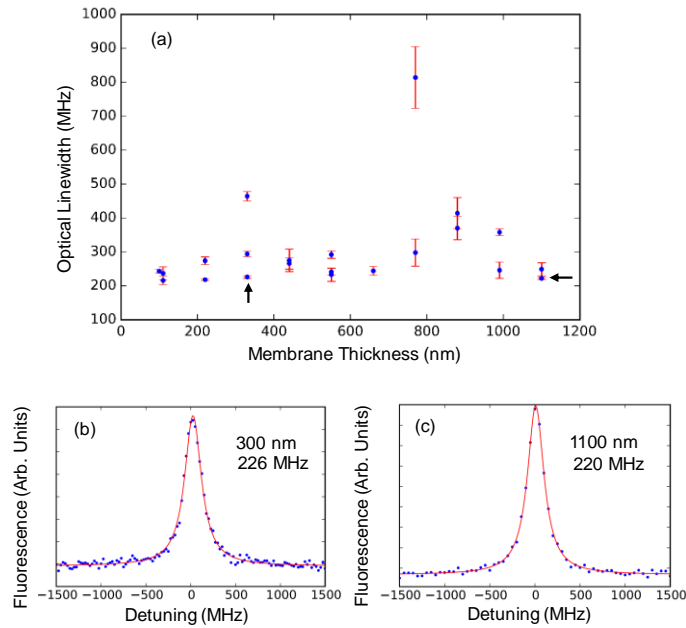
Figure 33: Optical characterization of SiV centers in thin diamond. (a) A scatter plot of the optical linewidths for SiV⁻ centers in diamond membranes with varying thicknesses. PLE spectrum of a SiV⁻ center in a membrane with a thickness of 330 nm. (c) PLE spectrum of a SiV⁻ center in a membrane with a thickness of 1100 nm. Red lines in (b) and (c) are least square fits to a Lorentzian, showing a linewidth of 226 MHz for (b) and 222 MHz for (c), as also indicated by the arrows in (a). The error bars in (a) correspond to the uncertainties in the numerical fits to single Lorentzian. All data were obtained at 12K.

Figure 33(a) plots the optical linewidths obtained for SiV⁻ centers in membranes with a thickness ranging from 100 nm to 1100 nm. A total of 22 SiV⁻ centers were examined in this set of experiments. For these data, we measured the thinnest part of the sample with an optical profilometer and determined the membrane thickness through the number of fringes counted from the thinnest edge. The errors for the estimated thickness are less than 1/4 of the interference fringe, i.e., < 25 nm. As shown in Fig. 33(a), 20 SiV⁻ centers exhibit optical linewidths between 200 to 400 MHz, while 17 SiV⁻ centers have linewidths between 200 and 300 MHz. Furthermore, there is no discernable dependence

of the SiV$^-$ optical linewidth on the membrane thickness. Figures 33(b) and 33(c) show, as an example, SiV$^-$ optical resonances obtained in membranes with estimated thickness of 330 nm and 1100 nm, respectively. The solid lines in Figs. 33(b) and 33(c) are the least square fit to a Lorentzian. The numerical fit gives an optical linewidth of 226 MHz and 222 MHz for SiV$^-$ centers in 330 and 1100 nm thick membranes, respectively.

For the experimental data shown in Fig. 33, the optical resonances correspond to the transitions from the ground states to the lower-energy excited state, though we have not attempted to determine the specific transition. This is in part due to the relatively high density of SiV$^-$ centers implanted in our sample. As discussed earlier, multiple SiV$^-$ centers (typically >5) are observed within the effective detection area. This, along with the strain induced energy level shifts, makes it difficult to identify the specific transition. In addition, for the transitions to the lower-energy excited state, there has been no evidence that the optical linewidth depends on the specific transitions.

We note that while the average implantation depth used is 100 nm, the strangle is about 20 nm. For PLE measurements in the thinnest part of the sample, we have by default used relatively bright SiV$^-$ centers, which are likely to be situated away from the surface, i.e., these centers were formed within 80 nm of the front surface. An average implantation depth of 100 nm was chosen because this was the depth used in our earlier work on NV centers and because we had expected SiV$^-$ centers to retain good optical coherence in membranes as thin as 200 nm. It is remarkable that excellent optical coherence of SiV$^-$ centers can still be seen in membranes as thin as 100 nm. For these thin membranes, an average implantation depth less than 100 nm should be a more optimal choice.

The experimental results shown in Fig. 33 are in sharp contrast to the results shown in Chapter VII. The NV optical linewidth starts to broaden when the membrane thickness is decreased to a few μm. Without graded soft etching, the NV optical linewidth exceeds 1 GHz at a membrane thickness of 1 μm. With graded soft etching, the NV optical linewidth can remain close to 300 MHz at a thickness of 1 μm, but broadens to beyond 1 GHz when the membrane thickness is decreased to below 500 nm. NV centers are extremely sensitive to charge fluctuations and thus to etching-induced damages. In comparison, because of the inversion symmetry of SiV$^-$ centers, the optical coherence of the SiV$^-$ centers is robust against charge fluctuations, which is further confirmed by the independence of the SiV$^-$ optical linewidth on the membrane thickness for membranes as thin as 100 nm. Based on these findings, we expect that optical coherence of SiV$^-$ centers can be retained in diamond nanostructures with similar feature sizes.

Optical coherence of SiV$^-$ centers can be affected by strong strain in the diamond sample. As shown in an earlier study[93], a relatively large strain can lead to a ground state splitting far exceeding the intrinsic spin-orbit splitting, thereby strongly modifying the thermalization process. At a ground-state splitting of about 400 GHz and at 4 K, the spin linewidth can be reduced from about 3.5 MHz to 1 MHz[93]. For the membranes studied in our work, the observed ground state splitting ranges from 48 GHz at a thickness of 100 nm to 60 GHz at a thickness near 1 μm (near the clamping area). The ground-state splitting in the membranes is thus close to the intrinsic spin-orbit splitting. As such, we do

105

not expect the strain in our sample to appreciably affect the optical linewidth of SiV⁻ centers.

Diamond membrane stripes as thin as 100 nm as shown in Fig. 31(b) can be incorporated into a cavity QED system that exploits the evanescent coupling between optical WGMs and color centers in the membrane, without spoiling the quality factor of the WMGs[30]. This type of cavity QED systems can reach the good cavity limit, in which the cavity linewidth is small compared with the linewidth of the SiV optical transitions as well as the relevant single-photon coupling rate, enabling a promising platform for optical quantum networks. It should be noted that the implantation parameters we have used led to a relatively high density of SiV centers. Multiple, but still spectrally resolvable, SiV⁻ centers can be a good choice for initial cavity QED efforts. In addition, it is relatively straight forward to reduce the SiV⁻ center density by adjusting the implantation parameters.

A.4 Summary

In summary, we have characterized the optical coherence of SiV⁻ centers implanted in diamond membranes. Using membranes with variable thicknesses, we show that excellent optical coherence of SiV⁻ centers can be maintained in membranes as thin as 100 nm. Diamond photonic nanostructures with SiV⁻ center can provide a promising and robust experimental platform for optical quantum networks. SiV⁻ center can also be used in the recently developed phononic networks of spins with closed mechanical subsystems, which can potentially enable new experimental platforms for phonon-based quantum information processing[94].

REFERENCES CITED

[1] G. E. Moore, "Cramming More Components Onto Integrated Circuits," *Proc. IEEE*, vol. 86, no. 1, pp. 82–85, Jan. 1998, doi: 10.1109/JPROC.1998.658762.

[2] M. Ekerå and J. Håstad, "Quantum Algorithms for Computing Short Discrete Logarithms and Factoring RSA Integers," in *Post-Quantum Cryptography*, vol. 10346, T. Lange and T. Takagi, Eds. Cham: Springer International Publishing, 2017, pp. 347–363.

[3] P. W. Shor, "Polynomial-Time Algorithms for Prime Factorization and Discrete Logarithms on a Quantum Computer," *SIAM J. Comput.*, vol. 26, no. 5, pp. 1484–1509, Oct. 1997, doi: 10.1137/S0097539795293172.

[4] D. Kielpinski, C. Monroe, and D. J. Wineland, "Architecture for a large-scale ion-trap quantum computer," *Nature*, vol. 417, no. 6890, pp. 709–711, Jun. 2002, doi: 10.1038/nature00784.

[5] K. Wright *et al.*, "Benchmarking an 11-qubit quantum computer," *Nature Communications*, vol. 10, no. 1, Art. no. 1, Nov. 2019, doi: 10.1038/s41467-019-13534-2.

[6] F. Arute *et al.*, "Quantum supremacy using a programmable superconducting processor," *Nature*, vol. 574, no. 7779, Art. no. 7779, Oct. 2019, doi: 10.1038/s41586-019-1666-5.

[7] J. Preskill, "Quantum Computing in the NISQ era and beyond," *Quantum*, vol. 2, p. 79, Aug. 2018, doi: 10.22331/q-2018-08-06-79.

[8] Z.-L. Xiang, S. Ashhab, J. Q. You, and F. Nori, "Hybrid quantum circuits: Superconducting circuits interacting with other quantum systems," *Rev. Mod. Phys.*, vol. 85, no. 2, pp. 623–653, Apr. 2013, doi: 10.1103/RevModPhys.85.623.

[9] "Ion-based commercial quantum computer is a first," *Physics World*, Dec. 17, 2018. https://physicsworld.com/a/ion-based-commercial-quantum-computer-is-a-first/ (accessed Aug. 10, 2020).

[10] J. Palmer, "Quantum computing takes big leap," *BBC News*, Mar. 22, 2011.

[11] H. J. Kimble, "The quantum internet," *Nature*, vol. 453, no. 7198, Art. no. 7198, Jun. 2008, doi: 10.1038/nature07127.

[12] M. W. Doherty, N. B. Manson, P. Delaney, F. Jelezko, J. Wrachtrup, and L. C. L. Hollenberg, "The nitrogen-vacancy colour centre in diamond," *Physics Reports*, vol. 528, no. 1, pp. 1–45, Jul. 2013, doi: 10.1016/j.physrep.2013.02.001.

[13] G. D. Fuchs, G. Burkard, P. V. Klimov, and D. D. Awschalom, "A quantum memory intrinsic to single nitrogen–vacancy centres in diamond," *Nature Physics*, vol. 7, no. 10, Art. no. 10, Oct. 2011, doi: 10.1038/nphys2026.

[14] D. A. Golter, K. N. Dinyari, and H. Wang, "Nuclear-spin-dependent coherent population trapping of single nitrogen-vacancy centers in diamond," *Phys. Rev. A*, vol. 87, no. 3, p. 035801, Mar. 2013, doi: 10.1103/PhysRevA.87.035801.

[15] S. Dhomkar, J. Henshaw, H. Jayakumar, and C. A. Meriles, "Long-term data storage in diamond," *Science Advances*, vol. 2, no. 10, p. e1600911, Oct. 2016, doi: 10.1126/sciadv.1600911.

[16] L. Rondin, J.-P. Tetienne, T. Hingant, J.-F. Roch, P. Maletinsky, and V. Jacques, "Magnetometry with nitrogen-vacancy defects in diamond," *Rep. Prog. Phys.*, vol. 77, no. 5, p. 056503, May 2014, doi: 10.1088/0034-4885/77/5/056503.

[17] V. M. Acosta, E. Bauch, A. Jarmola, L. J. Zipp, M. P. Ledbetter, and D. Budker, "Broadband magnetometry by infrared-absorption detection of nitrogen-vacancy ensembles in diamond," *Appl. Phys. Lett.*, vol. 97, no. 17, p. 174104, Oct. 2010, doi: 10.1063/1.3507884.

[18] P. Neumann *et al.*, "High-Precision Nanoscale Temperature Sensing Using Single Defects in Diamond," *Nano Lett.*, vol. 13, no. 6, pp. 2738–2742, Jun. 2013, doi: 10.1021/nl401216y.

[19] P. Ovartchaiyapong, K. W. Lee, B. A. Myers, and A. C. B. Jayich, "Dynamic strain-mediated coupling of a single diamond spin to a mechanical resonator," *Nature Communications*, vol. 5, no. 1, Art. no. 1, Jul. 2014, doi: 10.1038/ncomms5429.

[20] X. Zhu *et al.*, "Coherent coupling of a superconducting flux-qubit to an electron spin ensemble in diamond," *Nature*, vol. 478, no. 7368, pp. 221–224, Oct. 2011, doi: 10.1038/nature10462.

[21] Y. Kubo *et al.*, "Hybrid Quantum Circuit with a Superconducting Qubit Coupled to a Spin Ensemble," *Phys. Rev. Lett.*, vol. 107, no. 22, p. 220501, Nov. 2011, doi: 10.1103/PhysRevLett.107.220501.

[22] R. W. Andrews *et al.*, "Bidirectional and efficient conversion between microwave and optical light," *Nat Phys*, vol. 10, no. 4, pp. 321–326, Apr. 2014, doi: 10.1038/nphys2911.

[23] M. Hafezi, Z. Kim, S. L. Rolston, L. A. Orozco, B. L. Lev, and J. M. Taylor, "Atomic interface between microwave and optical photons," *Phys. Rev. A*, vol. 85, no. 2, p. 020302, Feb. 2012, doi: 10.1103/PhysRevA.85.020302.

[24] A. Rueda *et al.*, "Efficient single sideband microwave to optical conversion using an electro-optical whispering gallery mode resonator," *Optica*, vol. 3, no. 6, p. 597, Jun. 2016, doi: 10.1364/OPTICA.3.000597.

[25] D. Lee, K. W. Lee, J. V. Cady, P. Ovartchaiyapong, and A. C. B. Jayich, "Topical review: spins and mechanics in diamond," *J. Opt.*, vol. 19, no. 3, p. 033001, 2017, doi: 10.1088/2040-8986/aa52cd.

[26] I. Lekavicius, D. A. Golter, T. Oo, and H. Wang, "Transfer of Phase Information between Microwave and Optical Fields via an Electron Spin," *Phys. Rev. Lett.*, vol. 119, no. 6, p. 063601, Aug. 2017, doi: 10.1103/PhysRevLett.119.063601.

[27] I. Lekavicius, T. Oo, and H. Wang, "Diamond Lamb wave spin-mechanical resonators with optically coherent nitrogen vacancy centers," *Journal of Applied Physics*, vol. 126, no. 21, p. 214301, Dec. 2019, doi: 10.1063/1.5124307.

[28] I. Lekavicius and H. Wang, "Optical coherence of implanted silicon vacancy centers in thin diamond membranes," *Opt. Express, OE*, vol. 27, no. 22, pp. 31299–31306, Oct. 2019, doi: 10.1364/OE.27.031299.

[29] M. W. Doherty, N. B. Manson, P. Delaney, and L. C. L. Hollenberg, "The negatively charged nitrogen-vacancy centre in diamond: the electronic solution," *New J. Phys.*, vol. 13, no. 2, p. 025019, Feb. 2011, doi: 10.1088/1367-2630/13/2/025019.

[30] A. Gali, "Theory of the neutral nitrogen-vacancy center in diamond and its application to the realization of a qubit," *Phys. Rev. B*, vol. 79, no. 23, p. 235210, Jun. 2009, doi: 10.1103/PhysRevB.79.235210.

[31] H. Kaupp *et al.*, "Purcell-Enhanced Single-Photon Emission from Nitrogen-Vacancy Centers Coupled to a Tunable Microcavity," *Phys. Rev. Applied*, vol. 6, no. 5, p. 054010, Nov. 2016, doi: 10.1103/PhysRevApplied.6.054010.

[32] N. B. Manson and J. P. Harrison, "Photo-ionization of the nitrogen-vacancy center in diamond," *Diamond and Related Materials*, vol. 14, no. 10, pp. 1705–1710, Oct. 2005, doi: 10.1016/j.diamond.2005.06.027.

[33] A. Batalov *et al.*, "Low Temperature Studies of the Excited-State Structure of Negatively Charged Nitrogen-Vacancy Color Centers in Diamond," *Phys. Rev. Lett.*, vol. 102, no. 19, p. 195506, May 2009, doi: 10.1103/PhysRevLett.102.195506.

[34] J. R. Maze *et al.*, "Properties of nitrogen-vacancy centers in diamond: the group theoretic approach," *New J. Phys.*, vol. 13, no. 2, p. 025025, Feb. 2011, doi: 10.1088/1367-2630/13/2/025025.

[35] B. Hensen *et al.*, "Loophole-free Bell inequality violation using electron spins separated by 1.3 kilometres," *Nature*, vol. 526, no. 7575, Art. no. 7575, Oct. 2015, doi: 10.1038/nature15759.

[36] M. Jamali, I. Gerhardt, M. Rezai, K. Frenner, H. Fedder, and J. Wrachtrup, "Microscopic diamond solid-immersion-lenses fabricated around single defect centers by focused ion beam milling," *Review of Scientific Instruments*, vol. 85, no. 12, p. 123703, Dec. 2014, doi: 10.1063/1.4902818.

[37] R. J. Epstein, F. M. Mendoza, Y. K. Kato, and D. D. Awschalom, "Anisotropic interactions of a single spin and dark-spin spectroscopy in diamond," *Nature Physics*, vol. 1, no. 2, Art. no. 2, Nov. 2005, doi: 10.1038/nphys141.

[38] G. Balasubramanian *et al.*, "Ultralong spin coherence time in isotopically engineered diamond," *Nat Mater*, vol. 8, no. 5, pp. 383–387, May 2009, doi: 10.1038/nmat2420.

[39] K.-M. C. Fu, C. Santori, P. E. Barclay, L. J. Rogers, N. B. Manson, and R. G. Beausoleil, "Observation of the Dynamic Jahn-Teller Effect in the Excited States of Nitrogen-Vacancy Centers in Diamond," *Phys. Rev. Lett.*, vol. 103, no. 25, p. 256404, Dec. 2009, doi: 10.1103/PhysRevLett.103.256404.

[40] D. A. Golter and H. Wang, "Optically Driven Rabi Oscillations and Adiabatic Passage of Single Electron Spins in Diamond," *Phys. Rev. Lett.*, vol. 112, no. 11, p. 116403, Mar. 2014, doi: 10.1103/PhysRevLett.112.116403.

[41] P. R. Hemmer, A. V. Turukhin, M. S. Shahriar, and J. A. Musser, "Raman-excited spin coherences in nitrogen-vacancy color centers in diamond," *Opt. Lett., OL*, vol. 26, no. 6, pp. 361–363, Mar. 2001, doi: 10.1364/OL.26.000361.

[42] C. G. Yale *et al.*, "All-optical control of a solid-state spin using coherent dark states," *PNAS*, vol. 110, no. 19, pp. 7595–7600, May 2013, doi: 10.1073/pnas.1305920110.

[43] C. Santori *et al.*, "Coherent Population Trapping of Single Spins in Diamond under Optical Excitation," *Phys. Rev. Lett.*, vol. 97, no. 24, p. 247401, Dec. 2006, doi: 10.1103/PhysRevLett.97.247401.

[44] P. Bushev *et al.*, "Ultralow-power spectroscopy of a rare-earth spin ensemble using a superconducting resonator," *Phys. Rev. B*, vol. 84, no. 6, p. 060501, Aug. 2011, doi: 10.1103/PhysRevB.84.060501.

[45] D. I. Schuster *et al.*, "High-Cooperativity Coupling of Electron-Spin Ensembles to Superconducting Cavities," *Phys. Rev. Lett.*, vol. 105, no. 14, p. 140501, Sep. 2010, doi: 10.1103/PhysRevLett.105.140501.

[46] D. A. Golter, T. K. Baldwin, and H. Wang, "Protecting a Solid-State Spin from Decoherence Using Dressed Spin States," *Phys. Rev. Lett.*, vol. 113, no. 23, p. 237601, Dec. 2014, doi: 10.1103/PhysRevLett.113.237601.

[47] L. Childress *et al.*, "Coherent Dynamics of Coupled Electron and Nuclear Spin Qubits in Diamond," *Science*, vol. 314, no. 5797, pp. 281–285, Oct. 2006, doi: 10.1126/science.1131871.

[48] M. Fleischhauer and M. D. Lukin, "Dark-State Polaritons in Electromagnetically Induced Transparency," *Phys. Rev. Lett.*, vol. 84, no. 22, pp. 5094–5097, May 2000, doi: 10.1103/PhysRevLett.84.5094.

[49] E. E. Wollman *et al.*, "Quantum squeezing of motion in a mechanical resonator," *Science*, vol. 349, no. 6251, pp. 952–955, Aug. 2015, doi: 10.1126/science.aac5138.

[50] P. Rabl, "Cooling of mechanical motion with a two-level system: The high-temperature regime," *Phys. Rev. B*, vol. 82, no. 16, p. 165320, Oct. 2010, doi: 10.1103/PhysRevB.82.165320.

[51] P. Rabl, S. J. Kolkowitz, F. H. L. Koppens, J. G. E. Harris, P. Zoller, and M. D. Lukin, "A quantum spin transducer based on nanoelectromechanical resonator arrays," *Nature Physics*, vol. 6, no. 8, Art. no. 8, Aug. 2010, doi: 10.1038/nphys1679.

[52] E. R. MacQuarrie, T. A. Gosavi, A. M. Moehle, N. R. Jungwirth, S. A. Bhave, and G. D. Fuchs, "Coherent Control of a Nitrogen-Vacancy Center Spin Ensemble with a Diamond Mechanical Resonator," *arXiv:1411.5325 [cond-mat, physics:quant-ph]*, Nov. 2014, Accessed: May 12, 2016. [Online]. Available: http://arxiv.org/abs/1411.5325.

[53] A. Barfuss, J. Teissier, E. Neu, A. Nunnenkamp, and P. Maletinsky, "Strong mechanical driving of a single electron spin," *Nature Physics*, vol. 11, no. 10, pp. 820–824, Aug. 2015, doi: 10.1038/nphys3411.

[54] D. A. Golter, T. Oo, M. Amezcua, K. A. Stewart, and H. Wang, "Optomechanical Quantum Control of a Nitrogen-Vacancy Center in Diamond," *Phys. Rev. Lett.*, vol. 116, no. 14, p. 143602, Apr. 2016, doi: 10.1103/PhysRevLett.116.143602.

[55] D. A. Golter, T. Oo, M. Amezcua, I. Lekavicius, K. A. Stewart, and H. Wang, "Coupling a Surface Acoustic Wave to an Electron Spin in Diamond via a Dark State," *Phys. Rev. X*, vol. 6, no. 4, p. 041060, Dec. 2016, doi: 10.1103/PhysRevX.6.041060.

[56] S. Weis *et al.*, "Optomechanically induced transparency," *Science*, vol. 330, no. 6010, pp. 1520–1523, Dec. 2010, doi: 10.1126/science.1195596.

[57] K. W. Lee, D. Lee, P. Ovartchaiyapong, J. Minguzzi, J. R. Maze, and A. C. Bleszynski Jayich, "Strain Coupling of a Mechanical Resonator to a Single Quantum Emitter in Diamond," *Phys. Rev. Applied*, vol. 6, no. 3, p. 034005, Sep. 2016, doi: 10.1103/PhysRevApplied.6.034005.

[58] Y. Tao, J. M. Boss, B. A. Moores, and C. L. Degen, "Single-Crystal Diamond Nanomechanical Resonators with Quality Factors exceeding one Million," *Nature Communications*, vol. 5, Apr. 2014, doi: 10.1038/ncomms4638.

[59] B. P. Abbott *et al.*, "LIGO: the Laser Interferometer Gravitational-Wave Observatory," *Rep. Prog. Phys.*, vol. 72, no. 7, p. 076901, Jun. 2009, doi: 10.1088/0034-4885/72/7/076901.

[60] B. Khanaliloo, H. Jayakumar, A. C. Hryciw, D. P. Lake, H. Kaviani, and P. E. Barclay, "Single crystal diamond nanobeam waveguide optomechanics," *Physical Review X*, vol. 5, no. 4, Dec. 2015, doi: 10.1103/PhysRevX.5.041051.

[61] J. Zou, "High Quality Factor Lamb Wave Resonators," p. 62.

[62] D. Morgan, *Surface Acoustic Wave Filters: With Applications to Electronic Communications and Signal Processing*. Academic Press, 2010.

[63] S. A. Fedorov *et al.*, "Generalized dissipation dilution in strained mechanical resonators," *Phys. Rev. B*, vol. 99, no. 5, p. 054107, Feb. 2019, doi: 10.1103/PhysRevB.99.054107.

[64] G. S. MacCabe *et al.*, "Phononic bandgap nano-acoustic cavity with ultralong phonon lifetime," *arXiv:1901.04129 [cond-mat, physics:quant-ph]*, Jan. 2019, Accessed: May 26, 2020. [Online]. Available: http://arxiv.org/abs/1901.04129.

[65] P. Ovartchaiyapong, L. M. A. Pascal, B. A. Myers, P. Lauria, and A. C. B. Jayich, "High quality factor single-crystal diamond mechanical resonators," *Applied Physics Letters*, vol. 101, no. 16, p. 163505, Oct. 2012, doi: 10.1063/1.4760274.

[66] P. Maletinsky *et al.*, "A robust scanning diamond sensor for nanoscale imaging with single nitrogen-vacancy centres," *Nat Nano*, vol. 7, no. 5, pp. 320–324, May 2012, doi: 10.1038/nnano.2012.50.

[67] C. Santori, P. E. Barclay, K.-M. C. Fu, and R. G. Beausoleil, "Vertical distribution of nitrogen-vacancy centers in diamond formed by ion implantation and annealing," *Phys. Rev. B*, vol. 79, no. 12, p. 125313, Mar. 2009, doi: 10.1103/PhysRevB.79.125313.

[68] Y. Chu *et al.*, "Coherent Optical Transitions in Implanted Nitrogen Vacancy Centers," *Nano Lett.*, vol. 14, no. 4, pp. 1982–1986, Apr. 2014, doi: 10.1021/nl404836p.

[69] B. Naydenov *et al.*, "Increasing the coherence time of single electron spins in diamond by high temperature annealing," *Appl. Phys. Lett.*, vol. 97, no. 24, p. 242511, Dec. 2010, doi: 10.1063/1.3527975.

[70] Y. Tao and C. Degen, "Facile Fabrication of Single-Crystal-Diamond Nanostructures with Ultrahigh Aspect Ratio," *Adv. Mater.*, vol. 25, no. 29, pp. 3962–3967, Aug. 2013, doi: 10.1002/adma.201301343.

[71] S. Mouradian, N. H. Wan, T. Schröder, and D. Englund, "Rectangular photonic crystal nanobeam cavities in bulk diamond," *Appl. Phys. Lett.*, vol. 111, no. 2, p. 021103, Jul. 2017, doi: 10.1063/1.4992118.

[72] P. Appel *et al.*, "Fabrication of all diamond scanning probes for nanoscale magnetometry," *Review of Scientific Instruments*, vol. 87, no. 6, p. 063703, Jun. 2016, doi: 10.1063/1.4952953.

[73] M. Challier *et al.*, "Advanced Fabrication of Single-crystal Diamond Membranes for Quantum Technologies," *arXiv:1802.08971 [cond-mat, physics:physics, physics:quant-ph]*, Feb. 2018, [Online]. Available: http://arxiv.org/abs/1802.08971.

[74] D. Riedel *et al.*, "Deterministic Enhancement of Coherent Photon Generation from a Nitrogen-Vacancy Center in Ultrapure Diamond," *Phys. Rev. X*, vol. 7, no. 3, p. 031040, Sep. 2017, doi: 10.1103/PhysRevX.7.031040.

[75] T. Ishikawa *et al.*, "Optical and Spin Coherence Properties of Nitrogen-Vacancy Centers Placed in a 100 nm Thick Isotopically Purified Diamond Layer," *Nano Lett.*, vol. 12, no. 4, pp. 2083–2087, Apr. 2012, doi: 10.1021/nl300350r.

[76] F. F. de Oliveira *et al.*, "Effect of Low-Damage Inductively Coupled Plasma on Shallow NV Centers in Diamond," *Applied Physics Letters*, vol. 107, no. 7, p. 073107, Aug. 2015, doi: 10.1063/1.4929356.

[77] S. B. van Dam *et al.*, "Optical coherence of diamond nitrogen-vacancy centers formed by ion implantation and annealing," *arXiv:1812.11523 [cond-mat, physics:physics, physics:quant-ph]*, Dec. 2018, [Online]. Available: http://arxiv.org/abs/1812.11523.

[78] G. Anetsberger *et al.*, "Near-field cavity optomechanics with nanomechanical oscillators," *Nature Physics*, vol. 5, no. 12, Art. no. 12, Dec. 2009, doi: 10.1038/nphys1425.

[79] T. Oo, C. Dong, V. Fiore, and H. Wang, "Evanescently coupled optomechanical system with SiN nanomechanical oscillator and deformed silica microsphere," *Appl. Phys. Lett.*, vol. 103, no. 3, p. 031116, Jul. 2013, doi: 10.1063/1.4816292.

[80] M. C. Kuzyk and H. Wang, "Scaling Phononic Quantum Networks of Solid-State Spins with Closed Mechanical Subsystems," *Phys. Rev. X*, vol. 8, no. 4, p. 041027, Nov. 2018, doi: 10.1103/PhysRevX.8.041027.

[81] A. Stacey *et al.*, "Evidence for Primal sp2 Defects at the Diamond Surface: Candidates for Electron Trapping and Noise Sources," *arXiv:1807.02946 [cond-mat, physics:quant-ph]*, Jul. 2018, Accessed: Jul. 19, 2018. [Online]. Available: http://arxiv.org/abs/1807.02946.

[82] D. Bluvstein, Z. Zhang, and A. C. B. Jayich, "Identifying and mitigating charge instabilities in shallow diamond nitrogen-vacancy centers," Oct. 2018, Accessed: Oct. 23, 2018. [Online]. Available: https://arxiv.org/abs/1810.02058.

[83] S. Sangtawesin *et al.*, "Origins of Diamond Surface Noise Probed by Correlating Single-Spin Measurements with Surface Spectroscopy," *Phys. Rev. X*, vol. 9, no. 3, p. 031052, Sep. 2019, doi: 10.1103/PhysRevX.9.031052.

[84] E. Neu *et al.*, "Low-temperature investigations of single silicon vacancy colour centres in diamond," *New J. Phys.*, vol. 15, no. 4, p. 043005, Apr. 2013, doi: 10.1088/1367-2630/15/4/043005.

[85] C. Hepp *et al.*, "Electronic Structure of the Silicon Vacancy Color Center in Diamond," *Phys. Rev. Lett.*, vol. 112, no. 3, p. 036405, Jan. 2014, doi: 10.1103/PhysRevLett.112.036405.

[86] A. Sipahigil *et al.*, "Indistinguishable Photons from Separated Silicon-Vacancy Centers in Diamond," *Phys. Rev. Lett.*, vol. 113, no. 11, p. 113602, Sep. 2014, doi: 10.1103/PhysRevLett.113.113602.

[87] R. E. Evans, A. Sipahigil, D. D. Sukachev, A. S. Zibrov, and M. D. Lukin, "Narrow-Linewidth Homogeneous Optical Emitters in Diamond Nanostructures via Silicon Ion Implantation," *Phys. Rev. Applied*, vol. 5, no. 4, p. 044010, Apr. 2016, doi: 10.1103/PhysRevApplied.5.044010.

[88] A. Sipahigil *et al.*, "An integrated diamond nanophotonics platform for quantum-optical networks," *Science*, vol. 354, no. 6314, pp. 847–850, Nov. 2016, doi: 10.1126/science.aah6875.

[89] D. D. Sukachev *et al.*, "Silicon-Vacancy Spin Qubit in Diamond: A Quantum Memory Exceeding 10 ms with Single-Shot State Readout," *Phys. Rev. Lett.*, vol. 119, no. 22, p. 223602, Nov. 2017, doi: 10.1103/PhysRevLett.119.223602.

[90] B. C. Rose *et al.*, "Observation of an environmentally insensitive solid-state spin defect in diamond," *Science*, vol. 361, no. 6397, pp. 60–63, Jul. 2018, doi: 10.1126/science.aao0290.

[91] "OSA | Complete coherent control of silicon vacancies in diamond nanopillars containing single defect centers." https://www.osapublishing.org/optica/abstract.cfm?uri=optica-4-11-1317 (accessed Aug. 11, 2020).

[92] M. Larsson, K. N. Dinyari, and H. Wang, "Composite Optical Microcavity of Diamond Nanopillar and Silica Microsphere," *Nano Lett.*, vol. 9, no. 4, pp. 1447–1450, Apr. 2009, doi: 10.1021/nl8032944.

[93] Y.-I. Sohn *et al.*, "Controlling the coherence of a diamond spin qubit through strain engineering," *arXiv:1706.03881 [cond-mat, physics:quant-ph]*, Jun. 2017, [Online]. Available: http://arxiv.org/abs/1706.03881.

[94] M.-A. Lemonde *et al.*, "Phonon Networks with Silicon-Vacancy Centers in Diamond Waveguides," *Phys. Rev. Lett.*, vol. 120, no. 21, p. 213603, May 2018, doi: 10.1103/PhysRevLett.120.213603.